Lean Premixed Hydrogen Flames: Turbulence, Chemistry, and Modelling

Thesis by
Matthew X. Yao

In Partial Fulfillment of the Requirements for the
Degree of
Doctor of Philosophy

Caltech

CALIFORNIA INSTITUTE OF TECHNOLOGY
Pasadena, California

2024
Defended May 17, 2024

© 2024

Matthew X. Yao
ORCID: 0000-0001-6141-1477

ACKNOWLEDGEMENTS

No man is an island, and my PhD would not have been possible without the support of the many important people in my life throughout the past five years.

First and foremost, I would like to thank my advisor, Professor Guillaume Blanquart. Although your brain is one thousand times the size of mine, you were always patient in our meetings and scientific discussions (arguments). You provided encouragement when it was not deserved, and even though your jokes were the worst, you were a great cheerleader. Your guidance and support were instrumental in my success and my development as a scientist. I could not have asked for a better advisor. I would also like to thank the members of my thesis committee, Professors Tim Colonius, Jane Bae, and Melany Hunt, for their constructive feedback on the improvement of my research and scientific communication.

I would like to thank the friends I made during my time here, including Team DFA and members of TheFORCE. You were an endless source of entertainment, and provided much needed stress relief throughout my degree. In particular, I would like to thank my officemates, Alex Carroll, Alexandra Baumgart, Liam Heidt, and Aaron Nelson, without whom this work would have been completed much sooner. Our many discussions, both scientific and not, will always be remembered fondly. We must all imagine Sisyphus happy. I would also like to thank my friends from before my time at Caltech, including Dionne Pasion, Karl Vantomme, Brian Wong, Bill Li, Ned Zhou, and Omar Kamal. Although we were scattered across the continent, your presence online was especially appreciated during the pandemic isolation.

My journey begins with my parents, who have believed in me and provided me with everything I needed to succeed since the day I was born. My success is yours, and I cannot thank you enough. Thank you to my siblings, Kathleen and David, for always believing in me. Thank you to my grandma for providing me with a lifetime of delicious food, and to my aunt and uncle, Diana and Joe, and my cousins, Audrey and Emily, for always providing me with entertainment when I visit home.

Most importantly, I would like to express my gratitude to my fiancée, Jessica Lyda. You are my rock, and I am only who I am thanks to you. You make me better every day, and your unconditional love and support have made this all possible. I cannot wait to spend the rest of my life with you.

ABSTRACT

Lean turbulent premixed hydrogen/air flames have substantially increased flame speeds, a behaviour which is attributed to differential diffusion effects. In this thesis, the relationships between turbulence, chemistry, and modelling are studied through direct numerical simulation (DNS) and large eddy simulation (LES).

The effect of turbulence on lean hydrogen combustion is studied through DNS using detailed chemistry and detailed transport. Simulations are conducted at six Karlovitz numbers and four integral length scales. A general expression for the burning efficiency is proposed which depends on the conditional mean chemical source term and gradient of a progress variable. At a fixed Karlovitz number, the normalized turbulent flame speed and area both increase almost linearly with the integral length scale ratio. The effect on the mean source term profile is minimal, indicating that the increase in flame speed can solely be attributed to the increase in flame area. At a fixed integral length scale, both the flame speed and area first increase with Karlovitz number before decreasing. Neglecting Soret diffusion is shown to reduce the flame speed, area, and burning efficiency. At higher Karlovitz numbers, the diffusivity is enhanced due to penetration of turbulence into the reaction zone, significantly dampening differential diffusion effects.

The structure of lean hydrogen flames, namely the species mass fraction dependence on the local temperature, differs significantly from that of unity Lewis number fuels due to thermodiffusive instabilities. When subjected to turbulence, the conditional mean species mass fraction profiles are observed to transition from the laminar mixture-averaged flamelet solution to the unity Lewis number flamelet solution. We assess the impact of Soret diffusion and integral length scales on an effective Lewis number model. The results show that the turbulent flame structure can be mapped onto laminar flamelets via the use of effective Lewis numbers, which are expressed by an a priori Karlovitz number model. Although the flame structure is altered by Soret diffusion, there is still strong agreement with previously derived Karlovitz number models for effective Lewis numbers. To map the turbulent flames onto laminar flames with effective Lewis numbers, the relative impact of Soret diffusion needs to be proportionally reduced.

To assess the LES modelling of lean hydrogen flames, we simulate a low-swirl burner, an alternative means of clean energy generation. The LES modelling of

these flows remains challenging because the transition of small-scale instabilities into large-scale turbulent structures cannot be modelled by conventional strategies. Traditional one-equation tabulated chemistry formulations require only a progress variable, and cannot capture differential diffusion and curvature effects. In this work, we study the effects of tabulating different conditional mean source terms. It is shown that tabulating the appropriate conditional mean source term leads to improvements in the flow field prediction, however, key features such as the main recirculation region are not reproduced. Then, a two-equation tabulated chemistry model which accounts for differential diffusion and curvature effects is tested. This model provides the best agreement with experimental results. The work is a first effort in evaluating the performance of the two-equation model in the LES framework.

PUBLISHED CONTENT AND CONTRIBUTIONS

[1] M. X. Yao and G. Blanquart. "Capturing differential diffusion effects in large eddy simulation of turbulent premixed flames". In: *Proceedings of the Combustion Institute* (2024). (Under Review)
     The manuscript has been accepted for presentation and is under review for publication. The author of this thesis performed all simulations, analyzed the data, made the figures, and wrote the manuscript.

[2] M. X. Yao and G. Blanquart. "Isolating effects of large and small scale turbulence on thermodiffusively unstable premixed hydrogen flames". In: *Combustion and Flame* (2024). (Under Review)
     The author of this thesis performed all simulations, analyzed the data, made the figures, and wrote the manuscript.

TABLE OF CONTENTS

LIST OF ILLUSTRATIONS

LIST OF TABLES

Chapter 1

INTRODUCTION

1.1   Background and motivation

Despite the rapid adoption of renewable energy sources and higher efficiency equipment, combustion is expected to retain a significant role in U.S. energy sources through 2050 [1]. Current projections estimate that coal use will decrease drastically while natural gas use remains steady, driven primarily by needs in the industrial and electric power sectors. By 2030, carbon dioxide emissions in the U.S. are expected to fall to 25%-38% below 2005 levels [1], which does not meet the Paris Agreement target of 50%-52% below 2005 levels [2]. Furthermore, the global energy mix in 2050 is projected to consist of 70% fossil fuels with a continual increase of carbon dioxide emissions [3]. Besides carbon dioxide emissions, fossil fuel combustion produces pollutants such as sulfur dioxide, nitrogen oxides (NO_x), soot, unburnt fuels, fine particulate matter, and ozone, which have serious detrimental effects on human health [4, 5]. To minimize climate change and public health hazards, it is necessary to develop combustion devices which minimize these negative effects.

Hydrogen combustion has emerged as a promising technology with the potential to address the above challenges since it does not produce carbon emissions or soot. Another benefit is that, in principle, hydrogen can also be produced sustainably through renewable energy powered electrolysis. Hydrogen is also promising for its high specific energy density. For use in combustion devices, hydrogen can either be added to existing systems such as internal combustion engines, premixed combustors, and existing natural gas networks [6, 7, 8, 9, 10], or used as a standalone fuel [11, 12]. When hydrogen is added to fuel blends in limited quantities, the overall combustion dynamics are unchanged while hydrocarbon pollutant emissions are significantly reduced. However, care must be taken as the fraction of hydrogen is increased, as the combustion can become unstable. For example, Liu et al. [13] have shown that hydrogen addition up to 50% by volume is acceptable for MILD combustion.

Although hydrogen has benefits in reducing carbon and soot emissions, its high flame temperature leads to NO_x emissions which pose severe public health risks [14]. To minimize NO_x emissions, hydrogen is typically burnt lean (less fuel than oxidizer),

thus reducing the flame temperature. However, lean hydrogen combustion presents unique engineering and modelling challenges due to its propensity to develop combustion instabilities. In the presence of turbulence, these instabilities result in highly enhanced flame speeds, which can lead to safety concerns such as flame blowoff and flashback [9]. Blowoff refers to the situation where the flame cannot be stabilized due to a flow speed which is too high. In these cases, the flame propagates downstream and eventually extinguishes. Flashback refers to the situation where the flame cannot be stabilized due to a flow speed which is too low. In these cases, the flame propagates upstream into the inlet pipes, which can cause mechanical failure.

This thesis is focused on lean turbulent premixed hydrogen flames with applications in power generation. Accurate modelling of the unique burning properties of lean hydrogen combustion requires a comprehensive understanding of the fundamental combustion dynamics.

1.2 Premixed hydrogen flames

Premixed flames represent an asymptotic limit in which the fuel and oxidizer are considered to be fully mixed before combusting. The one-step irreversible chemical process is described by the conversion of fuel, F, and oxidizer, O, into products, P:

$$\nu_F F + \nu_o O \rightarrow P \tag{1.1}$$

For hydrogen flames, we have:

$$2H_2 + O_2 \rightarrow 2H_2O \tag{1.2}$$

In the presence of pure oxidizer, the only combustion product is water. The equivalence ratio, ϕ, is typically used to characterize premixed flames:

$$\phi = \frac{X_F/X_O}{(X_F/X_O)_{st}} = \frac{Y_F/Y_O}{(Y_F/Y_O)_{st}} \tag{1.3}$$

where X is the mole fraction, Y is the mass fraction, and the subscript st represents stoichiometric condition. In cases where $\phi < 1$, the mixture is lean, and there is less fuel than oxidizer compared to stoichiometric conditions. The opposite is true for rich mixtures where $\phi > 1$.

The dependence of the adiabatic flame temperature, T_{ad}, on ϕ is shown in Fig. 1.1 for an unburnt temperature $T_u = 298$ K and thermodynamic pressure of $P_0 = 1$ atm. The adiabatic flame temperatures at $\phi = 1$ and $\phi = 0.4$ are $T_{ad} = 2360$ K and 1400 K, respectively. The formation of NO_x emissions are dependent on

the temperature [15], due to the thermal or Zeldovich mechanism. In general, the thermal mechanism is suppressed for $T < 1800$ K [16, 13]. As such, burning lean hydrogen mixtures is preferred for reducing emissions.
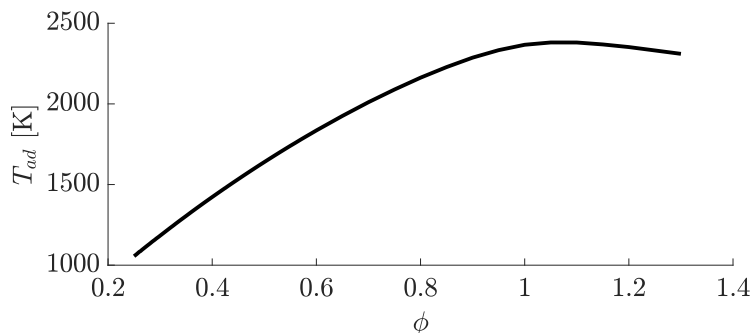
Figure 1.1: Adiabatic flame temperature versus equivalence ratio for hydrogen-air flames.

The temperatures in Fig. 1.1 are obtained from the simplest premixed flame configuration, the laminar, unstretched, freely propagating one-dimensional flame. These one-dimensional flames were calculated at varying equivalence ratios using FlameMaster [17], and the maximum flame temperature for each flame was extracted. Values obtained from these one-dimensional flames are often used as reference values when characterizing higher dimensional flames. Common examples include the laminar flame thickness, l_F, and the laminar flame speed, S_L, which is shown in Fig. 1.2. The laminar flame speed increases with the equivalence ratio.
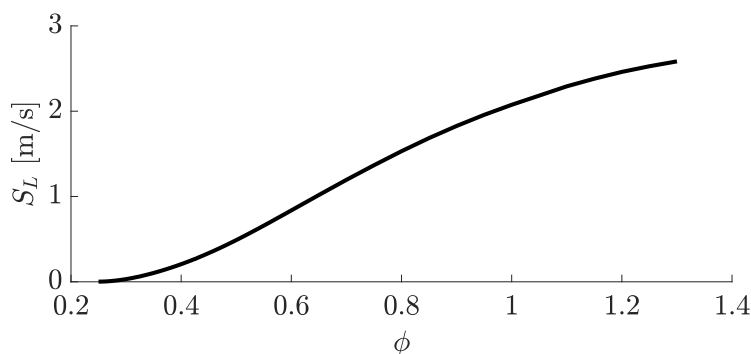
Figure 1.2: Laminar flame speed versus equivalence ratio for hydrogen-air flames.

1.3 Thermodiffusive instabilities

When extended to two- and three-dimensional configurations, lean hydrogen mixtures have a propensity to develop thermodiffusive instabilities (which will be described in the following section). In the presence of turbulence, the instabilities can cause the flame speed to increase significantly compared to S_L. Thermodiffusive

instabilities occur because of the relatively low Lewis number of hydrogen. The Lewis number of species i is defined as the ratio of mixture thermal diffusivity to species mass diffusivity:

$$\text{Le}_i = \frac{\alpha}{D_i} \tag{1.4}$$

For reference, the Lewis number of methane is close to unity, whereas the Lewis number of hydrogen is approximately 0.3.

The special burning properties of lean hydrogen combustion are attributed to differential diffusion effects [18]. It has been shown that an increase of turbulence decreases differential diffusion effects in terms of flame structure [19, 20]. However, differential diffusion is a term that may be used to refer to different physical phenomena. Thus, it is important here to clarify some definitions used in this thesis.

- *Preferential diffusion* refers to the notion that light species (e.g., H and H_2) have higher molecular diffusivities relative to other species in the mixture, and thus exhibit larger diffusive fluxes.

- *Non-unity Lewis number* refers to a mismatch of thermal to mass diffusivity. However, this does not require a difference in the relative magnitude of each species diffusivity.

- *Differential diffusion* refers to a combination of the previous two points, namely some species diffuse faster (or slower) than others and faster (or slower) than heat.

In premixed hydrogen flames, the Lewis numbers of H_2 and H are substantially lower than other species in the mixture. The mismatch of heat and mass diffusive fluxes give rise to the thermodiffusive instability. This is outlined in the schematic diagram in Fig. 1.3. At the flame front, the diffusion of species is principally in the normal direction. In regions of positive curvature, $\kappa > 0$, there is a focusing effect of the diffusion. In the case where all species Lewis numbers are equal, the species and heat are balanced and equally focused. This is not true for cases with non-unity Lewis numbers. In practice, the strongly diffusing fuel, H_2, arrives before the other species and heat. As such, there is a buildup of excess fuel in these regions. The opposite is true for regions of negative curvature, $\kappa < 0$. In these regions, the fuel experiences the defocusing effect first, and as such, produces regions which are fuel deficient. These effects result in fluctuations of the local equivalent ratio along

the flame front. Locally richer regions burn faster, and locally leaner regions burn slower (see Fig. 1.2), causing the growth of instability structures.
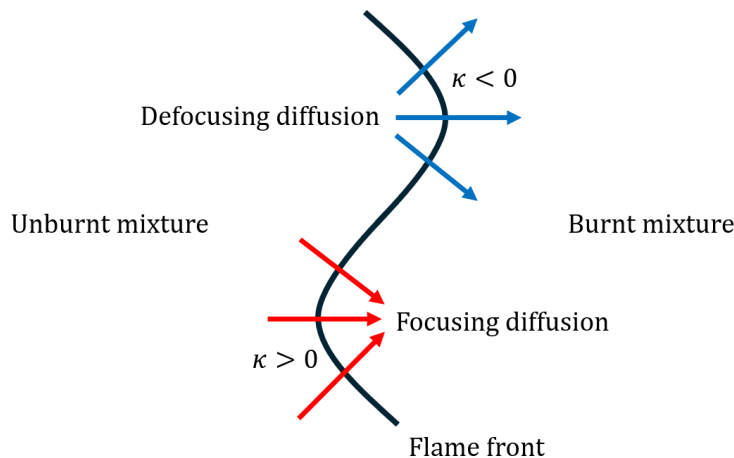
Figure 1.3: Schematic diagram of the cause of thermodiffusive instabilities.

In laminar flames, the instabilities manifest as characteristic cellular structures [21, 22], the onset of which are traditionally studied through linear stability analysis [23, 24, 25]. These cellular structures can be seen in Fig. 1.4, which shows the temperature field for a two-dimensional laminar flame at an equivalence ratio of $\phi = 0.4$ and nominal adiabatic flame temperature of $T_{ad} = 1400K$. The dynamics described earlier are reflected in this figure. In regions of positive curvature, there is superadiabatic burning due to the locally rich mixtures, which results in $T > T_{ad}$. In regions of negative curvature, $T < T_{ad}$. Overall, the thermodiffusive instabilities result in a highly corrugated flame front and nonhomogeneous burnt mixture.
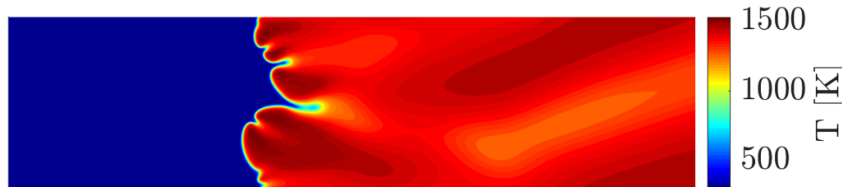
Figure 1.4: Temperature field of a two-dimensional laminar flame at $\phi = 0.4$.

Species with small molecular weight are also subject to Soret diffusion (mass diffusion driven by thermal gradients), which is known to enhance the instabilities for laminar flames [26].

1.4 Turbulent lean hydrogen premixed flames

When subject to turbulence, lean hydrogen flames exhibit highly enhanced flame speeds [27] which introduce safety concerns such as flashback and blowoff [9].

The special burning properties of turbulent lean hydrogen combustion have been investigated in a variety of direct numerical simulation (DNS) studies using detailed chemistry. Ideally, simulations would be conducted in practical combustor configurations, for example, the slot burner simulated by Berger et al. [28]. In these configurations, the flame is exposed to turbulence generated in the shear layer at the burner exit. Although physically realistic, these simulations are computationally expensive. As such, Berger et al. have only simulated a single relatively low Karlovitz number, defined as the ratio of flame to turbulence timescales. Pushing to higher Karlovitz numbers is prohibitive.

To make the problem computationally tractable, the domain can be reduced to a doubly periodic inflow-outflow configuration to focus specifically on flame-turbulence interactions. In these simulations, a forcing term is added to mimic the production of turbulence due to the missing large-scale mean shear [29]. Blanquart and coworkers [30, 31, 32] used this configuration extensively to investigate the two-way coupling between turbulence and combustion in neutrally stable hydrocarbon flames with detailed chemistry and transport. Building on this work, Schlup and Blanquart [33] performed one of the earliest DNS of turbulent unstable hydrogen flames which incorporated detailed transport with Soret effects. However, they studied only a single Karlovitz number.

The inflow-outflow configuration is a popular setup which has been used in a number of studies of lean turbulent hydrogen flames. Lee and coworkers [34, 35] employed forcing through the whole domain to study the impact of leading points on flame speed enhancement in thermodiffusively unstable flames. However, they did not account for Soret effects. Song et al. [36] and Yuvraj et al. [37] conducted DNS and studied the statistics of global and local flame speeds. In particular, they showed a strong relationship between the turbulent flame speed and the integral length scale. Although their work included Soret diffusion, the simulations were conducted at an equivalence ratio of $\phi = 0.7$, rendering the flames neutrally stable. Thus, they were not able to capture the effects of thermodiffusive instabilities.

All of the listed studies thus far were conducted at low to moderate Karlovitz numbers. Aspden et al. [38, 20] conducted simulations at extreme Karlovitz numbers to study the transition to the distributed burning regime. Once again, their configuration consisted of a flame which propagated in a doubly-periodic box with isotropic turbulence maintained through long wavelength forcing. This work was furthered by Howarth et al. [39], who conducted a detailed study on flame curvature and

provided further support for leading point theory. These studies did not include Soret diffusion.

The scaling of turbulent to laminar flame speed was first described by the phenomenological or conceptual model of Damköhler [40], who posited that locally, the flame front moves at the laminar flame speed. Thus, the following scaling was obtained:

$$\frac{S_T}{S_L} = \frac{A_T}{A} \tag{1.5}$$

where S_T is the turbulent flame speed, S_L is the laminar flame speed, A_T is the turbulent flame area, and A is the domain cross-sectional area. As the turbulence wrinkles the flame, it necessarily increases the flame area, which can be considered a global quantity. Notably, this model is not able to account for the local effects of turbulence, such as curvature or strain on the chemistry. The model was thus extended with the burning efficiency, I_0, to account for these effects [41, 42]:

$$\frac{S_T}{S_L} = I_0 \frac{A_T}{A} \tag{1.6}$$

There is no consensus on a general expression for I_0. Based on scaling arguments from Savard and Blanquart [30], Lapointe and Blanquart [43] proposed the following scaling for the ratio of turbulent to laminar flame speed for hydrocarbon flames:

$$\frac{S_T}{S_L} \approx \frac{\langle \dot{\omega}_C / |\nabla C| |C_{peak} \rangle}{\dot{\omega}_{C,lam} / |\nabla C_{lam}|} \frac{A_T}{A} \tag{1.7}$$

where C is a progress variable, and $\dot{\omega}_C$ is the corresponding source term. This model proposes a method of calculating the burning efficiency but relies on the assumption that the source term profiles locally scale as they do at C_{peak}. The applicability of this model has not yet been validated for hydrogen flames and is the subject of the present study.

1.5 Effective Lewis number model

To aid in the predictive design of practical engineering devices, there is a need for accurate and reliable large eddy simulation (LES) models which can accurately capture the combustion dynamics of these highly non-unity Lewis number fuels. One method that has been proposed in the past is the effective Lewis number model [19].

Aspden et al. [38] performed DNS on turbulent lean hydrogen/air flames at four Karlovitz numbers. They observed that the species mass fraction profiles as a

function of temperature did not match those of the corresponding one-dimensional laminar flame. Using their data, Savard and Blanquart [19] showed that the flame structure could be mapped onto one-dimensional flamelet solutions obtained using effective Lewis numbers instead of the nominal Lewis numbers. Their results showed that increased levels of turbulence led to the suppression of differential diffusion effects and pushed the effective Lewis numbers closer to unity. To aid in the development of reduced order chemistry models, they proposed a model which related the effective Lewis numbers to the Karlovitz numbers. However, their work did not consider the effects of Soret diffusion, which is known to change the flame structure [44] and enhance turbulent flame speeds [45] and thermodiffusive instabilities [26]. The impact of varying integral length scales was also not considered.

1.6 Tabulated chemistry

In order to reduce the cost of the numerical simulations and the modelling of the detailed chemical processes, other strategies rely on the use of only a few scalar equations. For instance, methods such as FPI (flame prolongation of ILDM) [46] and FGM (flamelet generated manifolds) [47] tabulate the chemical response of laminar flames with respect to a progress variable. For premixed flames, the simplest method is to create a lookup table based on a single one-dimensional flat unstretched flame [48]. The flame is parameterized by a progress variable, C, which defines uniquely the thermochemical state along the combustion trajectory. It is typically a linear combination of the mass fractions of intermediate species and products [49]. Its transport equation takes the form:

$$\partial_t (\rho C) + \nabla \cdot (\rho \mathbf{u} C) = \nabla \cdot (\rho D_C \nabla C) + \dot{\omega}_C \qquad (1.8)$$

Here, ρ is the density, $\mathbf{u}$ is the velocity vector, D_C is a diffusion coefficient, and $\dot{\omega}_C$ is the source term for C. At each timestep, important thermophysical properties are obtained via the lookup table.

Unfortunately, hydrogen exhibits strong differential diffusion effects due to its low Lewis number. This differential diffusion creates pockets of lean or rich mixtures, resulting in local fluctuations of the equivalence ratio and burning velocity. As such, the flame burns unevenly, and curvature effects become important, especially in the presence of turbulence. In these cases, the tabulation based on just C is insufficient to describe the physics [50, 48].

To account for differential diffusion, several strategies have been proposed. De Swart et al. [51] first derived a generic form of the transport equation for any control

variable (e.g., progress variable) which incorporates differential diffusion. The model was used by Donini et al. [52] with the controlling variables selected as a progress variable, enthalpy, and Bilger mixture fraction [53]. A source term which is dependent on the gradient of the progress variable is added to the transport equations of each of the control variables. However, this method is unable to reproduce flames dominated by differential diffusion due to the neglect of certain cross-diffusion terms. The model was updated by Mukundakumar et al. [54] to account for these missing terms, and showed improvement over the old model.

Other proposed methods include effects of curvature directly [55, 56] through tabulating flamelets generated using the compositional space method [57]. In these works, three major species are transported, which are then transformed into composition space for table lookup.

These proposed methods offer ways to incorporate differential diffusion effects but introduce additional complexities in the table generation and usage. A very simple model for non-unity Lewis number fuels was proposed by Regele et al. [58], who introduced a model which adds no additional source terms to the transport equation for the progress variable, and only one additional source term to the transport equation for the mixture fraction. However, the model relied on a single non-unity Lewis number and did not account for Soret diffusion. Schlup and Blanquart [33] recently generalized the model to accommodate non-constant Lewis numbers and Soret diffusion. In this model, the evaluation of the diffusion coefficients in the preprocessing step is minimal, since it depends only on diffusion coefficients which are already calculated in the flamelet generation. The reduced set of equations and lack of additional source terms in the progress variable equation also reduce the complexity of LES modelling. The model of Schlup and Blanquart [33] will be used for the calculations in this thesis.

1.7 Large eddy simulation

Several useful strategies for modelling turbulent premixed flames have been developed. For example, in the thickened flame model [59, 60], the flame front is artificially thickened by enhancing the molecular diffusion. However, the enhanced molecular diffusion can damp out critical small-scale flame instabilities that might be important in hydrogen combustion. Transported PDF methods are another modelling strategy [61, 62]. These methods may be used in conjunction with detailed chemistry, but they remain sensitive to the micro-mixing model used. As a result, it

is unclear whether these models can capture hydrogen instabilities properly.

The tabulated chemistry technique lends itself nicely to LES modelling due to the minimal amount of subfilter scale closure required. Berger et al. [63] recently conducted an a priori study to evaluate the validity of common subfilter scale models in the context of two-equation tabulated chemistry models. The results suggest that these strategies are valid for the two-equation models. However, their analysis has not yet been validated a posteriori.

1.8   Outline and objectives

This thesis investigates the relationship between large- and small-scale turbulence on the propagation and structure of turbulent lean hydrogen flames. The results are then used to inform the modelling of these flames. The specific objectives are outlined as:

1. Identify local (e.g., flame structure) and global (e.g., turbulent flame area) effects and quantify their individual contributions to the turbulent flame speed enhancement.

2. Quantify the effects of large- (integral length scale) and small- (dissipation) scale turbulence effects on the flame structure and propagation.

3. Evaluate the validity of burning efficiency expressions for thermodiffusively unstable flames.

4. Quantify the effect of Soret diffusion on turbulent lean premixed hydrogen flames.

5. Assess the validity of the two-equation tabulated chemistry model proposed by Schlup and Blanquart [33] across a wide range of Karlovitz numbers.

6. Quantify the effect of Soret diffusion and integral length scale on the effective species Lewis number model proposed by Savard and Blanquart [19].

7. Perform an a posteriori evaluation of LES modelling using the two-equation tabulated chemistry model in a complex geometry.

To support these goals, DNS are carried out using detailed chemistry and transport across a range of turbulence intensities and integral length scales. This dataset is central to this thesis, and is used extensively to fulfill the stated objectives. Then,

LES are carried out for a low-swirl burner [11] to test the validity of standard LES modelling.

The thesis is organized as follows. Chapter 2 presents the governing equations and details for both DNS and LES. Information regarding the numerical solver and implementation are also presented. A detailed analysis of the DNS results targeting Objectives 2–6 is presented in Chapter 3, and an evaluation of the effective species Lewis number model is presented in Chapter 4. Chapter 5 contains the LES of a low-swirl combustion chamber using the two-equation tabulated chemistry model. Finally, the major findings and future work are summarized in Chapter 6.

Chapter 2

GOVERNING EQUATIONS AND NUMERICAL METHOD

The simulations of turbulent premixed flames presented in this thesis are conducted within both the DNS and LES frameworks. This chapter provides an overview of the governing equations, namely, conservation of mass, momentum, species, and energy. The extension to the LES framework is also discussed, in particular with regards to the chemistry modelling. The equations are solved using the finite difference code NGA [64].

2.1 Governing equations

In the present study, the variable density, low Mach, reacting flow equations are solved. The low Mach formulation allows for the decoupling of the momentum and energy equations by eliminating the need to solve for the acoustic pressure field. A detailed derivation was conducted by Majda and Sethian [65]. After performing an asymptotic expansion of the variables in terms of the Mach number, the pressure field is decoupled into two components. The first, P_0, is the background thermodynamic pressure, which has no spatial variations and hence does not manifest in the momentum equation. The second, p, is the hydrodynamic pressure and does have spatial variations. However, the magnitude is small compared to the thermodynamic pressure and is thus neglected in the equation of state. The conservation equations for mass, momentum, temperature, and species are written:

$$\frac{\partial \rho}{\partial t} + \nabla \cdot (\rho \mathbf{u}) = 0 \tag{2.1}$$

$$\frac{\partial \rho \mathbf{u}}{\partial t} + \nabla \cdot (\rho \mathbf{u} \otimes \mathbf{u}) = -\nabla p + \nabla \cdot \boldsymbol{\tau} + \mathbf{f} \tag{2.2}$$

$$\frac{\partial \rho T}{\partial t} + \nabla \cdot (\rho \mathbf{u} T) = \nabla \cdot (\rho \alpha \nabla T) + \dot{\omega}_T - \frac{1}{c_p} \sum_i^{n_s} c_{p,i} \mathbf{j}_i \cdot \nabla T + \frac{\rho \alpha}{c_p} \nabla c_p \cdot \nabla T \tag{2.3}$$

$$\frac{\partial \rho Y_i}{\partial t} + \nabla \cdot (\rho \mathbf{u} Y_i) = -\nabla \cdot \mathbf{j}_i + \dot{\omega}_i \qquad i = 1 \dots n_s \tag{2.4}$$

The equations are closed with the ideal gas equation of state:

$$\rho = \frac{P_0 W}{RT} \tag{2.5}$$

where R is the universal gas constant, and W is the mixture molecular weight.

In these equations, t is the time, ρ is the density, $\mathbf{u} = \{u, v, w\}$ is the velocity vector, T is the temperature, c_p is the mixture heat capacity, and $\alpha = \lambda/(\rho c_p)$ is the mixture thermal diffusivity. The mixture-averaged thermal conductivity, λ, is calculated following Mathur et al. [66] using species thermal conductivities obtained via Eucken's formula [67]:

$$\lambda = \frac{1}{2} \left(\sum_i^{n_s} X_i \lambda_i + \left[\sum_i^{n_s} \frac{X_i}{\lambda_i} \right]^{-1} \right) \tag{2.6}$$

where X_i and λ_i are the mole fraction and thermal conductivity for species i. The viscous stress tensor is given as:

$$\boldsymbol{\tau} = \mu \left(\nabla \mathbf{u} + \nabla \mathbf{u}^T \right) - \frac{2}{3} \mu \left(\nabla \cdot \mathbf{u} \right) \mathbf{I} \tag{2.7}$$

where μ is the mixture dynamic viscosity and $\mathbf{I}$ is the identity tensor. The species viscosities are calculated following the standard gas kinetic relations [68], and the corresponding mixture-averaged viscosity follows a modified form of Wilke's formula [31, 69]:

$$\mu = \frac{1}{2} \left(\sum_i^{n_s} X_i \mu_i + \left[\sum_i^{n_s} \frac{X_i}{\mu_i} \right]^{-1} \right) \tag{2.8}$$

where μ_i is the species viscosity.

The momentum equation contains a forcing term $\mathbf{f}$, which is necessary to maintain the desired level of turbulence in the DNS results of this thesis due to the physical configuration of the problem. The forcing is discussed in detail in Chapter 3.

In the case of detailed chemistry, for each species i, we have the mass fraction Y_i, the species heat capacity $c_{p,i}$, the net species production rate $\dot{\omega}_i$ (units of $[\text{kg/m}^3\text{s}]$), and the species mass diffusion flux $\mathbf{j}_i$. The net species production rate is expressed as:

$$\dot{\omega}_i = W_i \sum_j^{n_R} v_{j,i} \dot{R}_j \tag{2.9}$$

where n_R is the total number of reactions, $v_{j,i}$ is the stoichiometric coefficient of species i in reaction j, and W_i is the species molecular weight. The coefficient is positive for products and negative for reactants. The reaction rate, $\dot{R}_i$, is in modified Arrhenius form:

$$\dot{R}_j = A_j T^{n_j} \exp\left(-\frac{E_{a,j}}{RT} \right) \prod_i^{n_s} \left(\frac{\rho Y_i}{W_i} \right)^{v_{j,i}^r} \tag{2.10}$$

where the pre-exponential term consists of the Arrhenius rate constant, A_j, and T^{n_j}, where n_j is a fitting constant. $E_{a,j}$ is the activation energy and $v_{j,i}^r = -\min(v_{j,i}, 0)$. The source term for the temperature equation is expressed as:

$$\dot{\omega}_T = -\frac{1}{c_p} \sum_i^{n_s} h_i(T)\, \dot{\omega}_i \tag{2.11}$$

where h_i is the enthalpy of species i at a given temperature.

In this work, the mixture-averaged diffusion model is employed. The species diffusion flux is then written:

$$\mathbf{j}_i = -\rho \frac{Y_i}{X_i} D_{i,m} \nabla X_i - \frac{1}{T} D_i^T \nabla T + \rho Y_i \mathbf{u}_c \tag{2.12}$$

where for each species i, $D_{i,m}$ is the mixture-averaged diffusion coefficient and D_i^T is the thermal diffusion coefficient. To ensure mass conservation and zero net diffusion flux, a correction velocity is introduced [70, 71]:

$$\mathbf{u}_c = \mathbf{u}_c^D + \mathbf{u}_c^T \tag{2.13}$$

which has contributions from the Fickian diffusion:

$$\mathbf{u}_c^D = \frac{\nabla W}{W} \sum_i^{n_s} D_{i,m} Y_i + \sum_i^{n_s} D_{i,m} \nabla Y_i \tag{2.14}$$

and the thermal diffusion:

$$\mathbf{u}_c^T = \frac{1}{\rho} \frac{\nabla T}{T} \sum_i^{n_s} D_i^T \tag{2.15}$$

where W is the mixture molecular weight. The present simulations use the reduced model recently proposed by Schlup and Blanquart for the calculation of the thermal diffusion coefficients [72, 73]. Typically, the calculation of thermal diffusion coefficients requires information from all other species. However, the species which are most sensitive to Soret diffusion are the light species, in this case, H_2 and H. By employing a number of simplifying assumptions regarding the relationships between transport properties and molecular weights, in particular, that the molecular weights of H_2 and H are significantly lower than that of the mixture, a simplified model for the thermal diffusion coefficients is obtained:

$$D_i^T \equiv -\alpha_i \frac{15}{4} \frac{X_i \mu_i}{\Phi_{i,m}} \left(1.2 C_{i,m}^* - 1\right)(1 - Y_i) - Y_i S \tag{2.16}$$

This model does not require information regarding other species, hence greatly reducing the computational cost. Here, α_i is an empirical scaling factor to correct for

systematic errors introduced through modelling assumptions. The values reported by Schlup and Blanquart [72] are $\alpha_{H_2} = 0.91$ and $\alpha_H = 0.895$. The term S is a correction factor which is applied to ensure mass conservation. The parameters $\Phi_{i,m}$ and $C_{i,m}$ depend only on the properties of H_2 and H and empirical fits of collision integrals.

2.2 Tabulated chemistry

In combustion simulations, a large part of the computational cost is attributed to the additional governing equations for each species, along with the evaluation of transport and thermodynamic properties. To reduce the computational cost, a popular strategy is the use of tabulated chemistry. In the tabulated chemistry framework, the thermochemical trajectory is calculated using a simplified representative model of the combustion process, and tabulated with respect to a reduced set of control variables. Instead of transporting all species, only the control variables are transported, which are used to look up necessary values in the precomputed table.

For fully premixed flames, the simplest method is to create a lookup table based on a single one-dimensional flat unstretched flame [48]. The flame is parameterized by a progress variable, C, which defines uniquely the thermochemical state along the combustion trajectory. It is typically a linear combination of the mass fractions of intermediate species and products [49]. Its transport equation is written:

$$\frac{\partial \rho C}{\partial t} + \nabla \cdot (\rho \mathbf{u} C) = \nabla \cdot (\rho D_C \nabla C) + \dot{\omega}_C \qquad (2.17)$$

and takes the same form as a species transport equation. Eq. (2.17) is solved in place of Eqs (2.3) and (2.4). Here, D_C and $\dot{\omega}_C$ are the molecular diffusivity and source term for C. At each timestep, important thermophysical properties such as ρ, μ, D_C, and $\dot{\omega}_C$ are obtained via the lookup table.

One-dimensional flat flames serve as an appropriate proxy for higher dimensional flames in which the Lewis number for all species are approximately unity. This is a reasonable assumption for many fuels, for example, methane. However, hydrogen experiences differential diffusion due to its low Lewis number. In these cases, the tabulation based on just C is insufficient to describe the physical process [50, 48].

In this work, we employ the model of Schlup and Blanquart [33], which introduces an additional control variable, Z, a mixture fraction-like variable which represents fluctuations in the local equivalence ratio due to differential diffusion effects. The

equation for Z reads:

$$\frac{\partial \rho Z}{\partial t} + \nabla \cdot (\rho \mathbf{u} Z) = \nabla \cdot (\rho D_Z \nabla Z) - \underbrace{\nabla \cdot (\rho D_Z^* \nabla C)}_{\text{source term 1}} + \underbrace{\nabla \cdot \left(\rho D_Z^T \nabla T \right)}_{\text{source term 2}} \quad (2.18)$$

where

$$D_Z = \frac{\nu Y_{F,1} D_F + Y_{O,2} D_O}{\nu Y_{F,1} + Y_{O,2}} \quad (2.19)$$

$$D_Z^* = \left(\frac{1}{\nu + 1} \right) \left(\frac{\nu D_F - \nu D_O}{\nu Y_{F,1} + Y_{O,2}} \right) \quad (2.20)$$

and

$$D_Z^T = \frac{1}{\rho T} \left(\frac{\nu D_F^T - D_O^T}{\nu Y_{F,1} + Y_{O,2}} \right) \quad (2.21)$$

where D_i and D_i^T represent the molecular and thermodiffusion coefficients, respectively. The variable Y indicates the mass fraction, the subscripts O and F indicate oxidizer and fuel, and the subscripts 1 and 2 refer to the fuel and oxidizer streams, respectively. The definition of the mass stoichiometric ratio, ν, is given by:

$$\nu = \frac{\nu_O W_O}{\nu_F W_F} \quad (2.22)$$

where W_i are the species molecular weights.

This model is a generalized form of the model by Regele et al. [58], which has no assumptions regarding the species Lewis numbers and accounts for thermal diffusion. To create the thermochemical table, a number of one-dimensional flat flames at different equivalence ratios are computed with FlameMaster [17] using detailed chemistry, mixture-averaged molecular diffusion [73], and Soret diffusion. The reduced order model of Schlup and Blanquart [72] was used for the thermodiffusion coefficients. The necessary thermodynamic and transport properties, $\left(T, \rho, \mu, D_Z, D_Z^*, D_Z^T, D_C, \dot{\omega}_C \right)$, are interpolated onto a two-dimensional chemistry table as a function of C and Z. The one-dimensional flamelets were calculated for equivalence ratios between $\phi = 0.25$ and $\phi = 1.3$. For more details on the full derivation of the new chemistry model, the reader is referred to [33].

The transport equation for Z has two source terms. The first bracketed term is a cross-diffusion term which couples the response of Z to the local fluctuations of C. In particular, the term can be decomposed into two parts [74, 75, 33]:

$$\nabla \cdot \left(\rho D_Z^* \nabla C \right) = -\rho D_Z^* |\nabla C| \kappa + \mathbf{n} \cdot \nabla \left(\rho D_Z^* |\nabla C| \right) \quad (2.23)$$

where

$$\kappa = -\nabla \cdot \mathbf{n} = -\nabla \cdot \left(\frac{\nabla C}{|\nabla C|} \right) \tag{2.24}$$

represents the curvature of the flame front defined by an isosurface of C. This feedback is particularly important since flame curvature is inseparably linked to differential diffusion effects. The second bracketed term incorporates the contribution of Soret diffusion to the differential diffusion effects. This is important since Soret diffusion is known to enhance the thermodiffusive instabilities in laminar flames [26].

2.3   Large eddy simulation

In this section we review the governing equations and subfilter scale modelling of the LES framework.

2.3.1   Governing equations

In the LES framework, the turbulence is separated into large-scale components which are resolved on the grid and small-scale contributions which must be modelled. The governing equations are recast in terms of spatially filtered variables, denoted by an overline, $\overline{(\ )}$, which are resolved quantities. In the framework of LES, the filtered Navier-Stokes equations are:

$$\frac{\partial \overline{\rho}}{\partial t} + \nabla \cdot (\overline{\rho} \widetilde{\mathbf{u}}) = 0 \tag{2.25}$$

$$\frac{\partial \overline{\rho} \widetilde{\mathbf{u}}}{\partial t} + \nabla \cdot (\overline{\rho} \widetilde{\mathbf{u}} \otimes \widetilde{\mathbf{u}}) = -\nabla \overline{p} + \nabla \cdot \boldsymbol{\tau} + \nabla \cdot \overline{\boldsymbol{\tau}}^{SGS} \tag{2.26}$$

The tilde denotes a Favre average quantity, $\widetilde{\phi} = \overline{\rho \phi}/\overline{\phi}$. The turbulent eddy viscosity (μ_t) is evaluated using the Lagrangian dynamic subfilter scale model of Meneveau et al. [76].

In many practical applications, the grid resolution required to resolve the turbulence for DNS is comparable to the grid resolution required for the detailed chemistry. In LES, the smallest scales of turbulence are not resolved and, consequently, the chemistry length scales are also under-resolved. To use finite rate chemistry, significant modelling efforts are required to close subfilter terms in the species and energy transport equations [77, 78, 79]. To reduce the complexity of LES modelling while retaining finite rate chemistry effects, reduced order models such as tabulated chemistry are preferred [80, 81, 82]. The filtered versions of the transport equations for C and Z, Eqs. (2.17) and (2.18), are written as:

$$\frac{\partial \overline{\rho} \widetilde{C}}{\partial t} + \nabla \cdot \left(\overline{\rho} \widetilde{\mathbf{u}} \widetilde{C} \right) = \nabla \cdot \left(\overline{\rho} \left(\widetilde{D}_C + D_C^t \right) \nabla \widetilde{C} \right) + \overline{\dot{\omega}}_C \tag{2.27}$$

$$\frac{\partial \overline{\rho} \widetilde{Z}}{\partial t} + \nabla \cdot \left(\overline{\rho} \widetilde{\mathbf{u}} \widetilde{Z} \right) = \nabla \cdot \left(\overline{\rho} \left(\widetilde{D}_Z + D_Z^t \right) \nabla \widetilde{Z} \right) - \nabla \cdot \left(\overline{\rho} \widetilde{D}_Z^* \nabla \widetilde{C} \right) + \nabla \cdot \left(\overline{\rho} \widetilde{D}_Z^T \nabla \widetilde{T} \right) \tag{2.28}$$

The eddy diffusivities, D_C^t and D_Z^t, are evaluated using the Lagrangian dynamic subfilter scale model of Meneveau et al. [76]. The eddy diffusivity model is consistent with the formulation of Réveillon and Vervisch [83]. Alternative subfilter scale models and the filtering of the chemical source term are discussed in further detail in Chapter 5.

2.3.2 Subfilter scale modelling — fluid mechanics

The filtered equations produce unresolved stresses which need to be modelled. The unresolved turbulent stresses are expressed as:

$$\tau^{SGS} = \mu_t \left(\nabla \widetilde{\mathbf{u}} + \nabla \widetilde{\mathbf{u}}^t \right) \tag{2.29}$$

where μ_t is the turbulent eddy viscosity which is computed following the Smagorinsky model:

$$\mu_t = (C_s \Delta)^2 \, \widetilde{S} \tag{2.30}$$

Here, $\widetilde{S}$ is the characteristic filtered rate-of-strain:

$$\widetilde{S} = \left(2 \widetilde{S}_{ij} \widetilde{S}_{ij} \right)^{1/2} \tag{2.31}$$

where

$$\widetilde{S}_{i,j} = \frac{1}{2} \left(\frac{\partial \widetilde{u}_i}{\partial x_j} + \frac{\partial \widetilde{u}_j}{\partial x_i} \right) \tag{2.32}$$

is the filtered rate-of-strain tensor. The filter width is denoted Δ, and C_s is the Smagorinsky coefficient. The earliest Smagorinsky models determined C_s to be a constant [84]. However, the value of the constant changes depending on the flow configuration, and thus a global constant is not appropriate for complex flows found in many applications. Instead, a local value of C_s is preferred, and is evaluated via a dynamic procedure [85, 86]:

$$C_s^2 = \frac{M_{ij} \mathcal{L}_{ij}}{M_{kl} M_{kl}} \tag{2.33}$$

where

$$\mathcal{L}_{ij} = \widetilde{\widehat{u_i u_j}} - \widehat{\widetilde{u}}_i \widehat{\widetilde{u}}_j \tag{2.34}$$

is the resolved stress, and

$$M_{ij} = 2\Delta^2 \widehat{\overline{S}\overline{S}_{ij}} - 2\widehat{\Delta}^2 \widehat{\widetilde{S}}\widehat{\widetilde{S}}_{ij} \tag{2.35}$$

where the operator $\widehat{(\ )}$ denotes a filtering procedure at a filter width $\widehat{\Delta} > \Delta$. In this work, we use the Lagrangian dynamic model of Meneveau et al. [76] in order to prevent numerical instabilities:

$$C_s^2 = \frac{\langle M_{ij}\mathcal{L}_{ij}\rangle}{\langle M_{kl}M_{kl}\rangle} \tag{2.36}$$

For a variable $\phi\,(t, \mathbf{x}\,(t))$, the average is formed tracing fluid pathlines backward in time:

$$\langle \phi \rangle = \xi \phi\,(t, \mathbf{x}(t)) + (1 - \xi)\,\phi\,(t - \Delta t, \mathbf{x}\,(t - \Delta t)) \tag{2.37}$$

where ξ is a weighting function:

$$\xi = \left(\frac{2\Delta t\,\left[\langle M_{ij}\mathcal{L}_{ij}\rangle\langle M_{kl}M_{kl}\rangle\right]^{1/8}}{3\Delta}\right)\left(1 + \frac{2\Delta t\,\left[\langle M_{ij}\mathcal{L}_{ij}\rangle\langle M_{kl}M_{kl}\rangle\right]^{1/8}}{3\Delta}\right)^{-1} \tag{2.38}$$

The method is not restricted to homogeneous flows and is appropriate for use in the complex flow fields simulated in this thesis. Initially these models were derived for homogeneous isotropic turbulence. They have been used extensively in LES of turbulent reacting flows. A detailed analysis of their validity for such configurations should be performed, but is outside the scope of this work.

2.3.3 Subfilter scale modelling — chemistry

The eddy diffusivities of Eqs. (2.27) and (2.28) are calculated using the same algebraic form as the eddy viscosity. The subfilter scalar flux is expressed as:

$$\tau_\phi^{SGS} = \overline{\rho}D_\phi^t \nabla\widetilde{\phi} \tag{2.39}$$

where D_ϕ^t is the turbulent eddy diffusivity:

$$D_\phi^t = \left(C_s^\phi\Delta\right)^2 \widetilde{S} \tag{2.40}$$

The evaluation of the dynamic coefficient, C_s^ϕ, is similar to that of Eq. (2.33):

$$C_s^{\phi 2} = \frac{\langle M_i\mathcal{L}_i\rangle}{\langle M_iM_i\rangle} \tag{2.41}$$

where

$$\mathcal{L}_i = \widehat{\widetilde{u}_i\widetilde{\phi}} - \widehat{\widetilde{u}}_i\widehat{\widetilde{\phi}} \tag{2.42}$$

and

$$M_i = 2\Delta^2 \widetilde{\widehat{S}\nabla\widetilde{\phi}} - 2\widehat{\Delta}^2 \widehat{\widetilde{S}}\widehat{\nabla\widetilde{\phi}} \tag{2.43}$$

The Lagrangian averaging procedure [76, 83] is also applied to evaluate the Smagorinsky coefficient.

For LES modelling of the tabulated chemistry, an assumed PDF model is typically employed (more details are provided in Chapter 5). In this model, information regarding the subfilter variance, C_v, of the progress variable is necessary. The subfilter variance is calculated using an algebraic model [87]:

$$C_v = \left(C_\phi \Delta\right)^2 |\nabla\widetilde{C}|^2 \tag{2.44}$$

where the coefficient C_ϕ is also determined through a dynamic procedure similar to the one outlined previously:

$$C_\phi^2 = \frac{\langle ML \rangle}{\langle MM \rangle} \tag{2.45}$$

where

$$M = \widehat{\Delta}^2 \nabla\widehat{\widetilde{C}} \cdot \nabla\widehat{\widetilde{C}} \tag{2.46}$$

and

$$L = \widehat{\widetilde{C}\widetilde{C}} - \widehat{\widetilde{C}}\widehat{\widetilde{C}} \tag{2.47}$$

where the hat indicates a test filtering at a filter width $\widetilde{\Delta} > \Delta$. The averaging procedure is also conducted using the Lagrangian method of Meneveau et al. [76].

2.4 Numerical method

To solve the governing equations, the finite difference code NGA [64] is used. A brief description of the code is presented here.

2.4.1 Spatial discretization

The equations are solved using NGA [64], a structured finite difference code with arbitrarily high order spatial accuracy. Relevant details regarding the numerical methods are highlighted here.

To minimize dispersive errors, NGA employs a staggered grid, where scalars (e.g., density and pressure) are stored at the cell centers, and velocity and momentum components are stored at the cell faces. In this work, we will consider both Cartesian, $\mathbf{u} = \left(u_x, u_y, u_z\right)$ in $\mathbf{x} = (x, y, z)$, and cylindrical, $\mathbf{u} = (u_x, u_r, u_\theta)$ in $\mathbf{x} = (x, r, \theta)$ coordinates. The cell faces are numbered as i_1, i_2, i_3, respectively, for the x_1, x_2, x_3 directions. Because of the staggering, variables are offset by 1/2 in certain directions.

For example, the u_x velocity component is stored at $i_1, i_2 + 1/2, i_3 + 1/2$. The variable locations are shown on representative computational cells in Fig. 2.1. To perform the spatial discretization, the physical coordinates (Cartesian or cylindrical) are mapped to computational coordinates of unity spacing, $\zeta = (\zeta_1, \zeta_2, \zeta_3)$, with associated scaling factors defined by differentiating physical space by computational space. In the current work, second-order accurate operators are used to discretize the convective and diffusive terms in the governing equations. Key operators are the second-order interpolation and differentiation operators. For a stencil size $\Delta \zeta_1$ in the ζ_1 direction on a variable, ϕ, these operators are given as:

$$\overline{\phi}^{\zeta_1} = \frac{\phi\left(\zeta_1 + \Delta\zeta_1/2, \zeta_2, \zeta_3\right) + \phi\left(\zeta_1 - \Delta\zeta_1/2, \zeta_2, \zeta_3\right)}{2} \tag{2.48}$$

and

$$\frac{\delta\phi}{\delta\zeta_1} = \frac{\phi\left(\zeta_1 + \Delta\zeta_1/2, \zeta_2, \zeta_3\right) - \phi\left(\zeta_1 - \Delta\zeta_1/2, \zeta_2, \zeta_3\right)}{\Delta\zeta_1} \tag{2.49}$$

respectively. Because all operators are centered, the code does not exhibit dissipative errors. For a complete description of the spatial discretization, including higher order operators, variable density flows, conservation properties, centerline treatments, and discrete equations, the reader is referred to [64].

(a) Cartesian coordinates   (b) Cylindrical coordinates
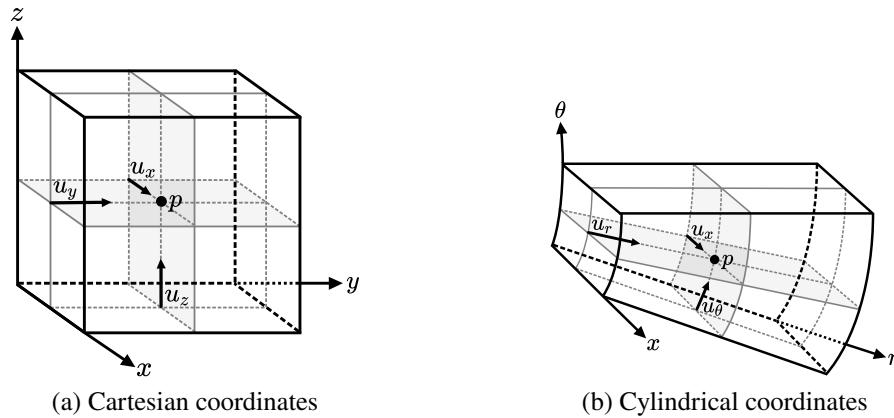
Figure 2.1: Computational cells and variable locations in the staggered grid discretization.

2.4.2 Temporal discretization

The time integration scheme is summarized here. For the full details, the reader is referred to Savard et al. [88]. The scalar and velocity fields are also staggered in time, with the scalar fields being advanced from time $t^{n+1/2}$ to $t^{n+3/2}$ and the velocity fields being advanced from time t^n to t^{n+1}, where the superscript indicates the time step. In the following description the timestep, Δt, is assumed to be uniform. The time integration is iterative and proceeds as follows.

The governing equations are advanced in time using an iterative procedure, where the subscript k denotes the sub-iteration. The total number of subiterations, K, is set a priori. The calculations in this thesis are performed with $K = 4$. First, converged values from the previous time step are used as the initial guesses for the iterative procedure i.e. $k = 0$):

$$p_0^{n+3/2} = p^{n+1/2}, \quad \mathbf{Y}_0^{n+3/2} = \mathbf{Y}^{n+1/2}, \quad (\rho \mathbf{u})_0^{n+1} = (\rho \mathbf{u})^n . \tag{2.50}$$

An estimate for the density is obtained using the Adams-Bashforth prediction:

$$\rho_0^{n+3/2} = 2\rho^{n+1/2} - \rho^{n-1/2} \tag{2.51}$$

ensuring discrete conservation of mass at the beginning of the iterative procedure [89]. For the subiterations $k = 1, \ldots, K$, the time integration proceeds in the following order: advance the scalar field, calculate the density field, predict the velocity field (with no consideration of continuity), correct the velocity field after solving the pressure Poisson equation to ensure mass conservation, and finally, updating the solution. The steps are detailed as:

1. Advance the scalar field:

$$\mathbf{Y}_k^* = \frac{\mathbf{Y}^{n+1/2} + \mathbf{Y}_k^{n+3/2}}{2} \tag{2.52}$$

$$\rho_k^{n+3/2} \mathbf{Y}_{k+1}^{n+3/2} = \rho^{n+1/2} \mathbf{Y}^{n+1/2} + \Delta t \left[(\mathbf{C} + \mathbf{D})_k^{n+1} \cdot \mathbf{Y}_k^* + \mathbf{\Omega}_k^* \right]$$
$$+ \frac{\Delta t}{2} \left(\frac{\partial \mathbf{C}}{\partial \mathbf{Y}} + \frac{\partial \mathbf{D}}{\partial \mathbf{Y}} \right)_k^{n+1} \cdot \left(\mathbf{Y}_{k+1}^{n+3/2} - \mathbf{Y}_k^{n+3/2} \right) \tag{2.53}$$

   where $\mathbf{C}$ and $\mathbf{D}$ are abbreviated notation for the convective and diffusive terms in the scalar equation (Eq. (2.4)), respectively. The corresponding Jacobian matrices for the convective and diffusive terms are expressed as $\partial \mathbf{C}/\partial \mathbf{Y}$ and $\partial \mathbf{D}/\partial \mathbf{Y}$.

2. Next, the density field is predicted from the ideal gas law:

$$\rho_{k+1}^{n+3/2} = \frac{p_0 \left(\sum_{i=1}^N Y_{i,k+1}^{n+3/2}/W_i \right)^{-1}}{RT_{k+1}^{n+3/2}} \tag{2.54}$$

   Although conservation of species densities, ρY_i, is not ensured in this step, upon convergence of the subiterations the conservation of species densities is satisfied.

3. The momentum field is advanced:

$$\mathbf{u}_k^* = \frac{\mathbf{u}^n + \mathbf{u}_k^{n+1}}{2} \tag{2.55}$$

$$\frac{\rho^{n+1/2} + \rho_{k+1}^{n+3/2}}{2} \widehat{\mathbf{u}}_{k+1}^{n+1} = \frac{\rho^{n-1/2} + \rho^{n+1/2}}{2} \mathbf{u}^n$$
$$+ \Delta t \left[(\mathbf{C}_u + \mathbf{D}_u)_k^{n+1/2} \cdot \mathbf{u}_k^* + \nabla p_k^{n+3/2} \right]$$
$$+ \frac{\Delta t}{2} \left(\frac{\partial \mathbf{C}_u}{\partial \mathbf{u}} + \frac{\partial \mathbf{D}_u}{\partial \mathbf{u}} \right)_k^{n+1/2} \cdot \left(\widehat{\mathbf{u}}_{k+1}^{n+1} - \mathbf{u}_k^{n+1} \right) \tag{2.56}$$

where $\widehat{\mathbf{u}}$ is a predicted velocity field which does not necessarily satisfy mass conservation, and is used to compute the hydrodynamic pressure in the following step. The discrete convective and viscous terms are written as $\mathbf{C}_u$ and $\mathbf{D}_u$.

4. The Poisson equation for the hydrodynamic pressure is solved to obtain a correction to ensure mass conservation:

$$\nabla^2 (\delta p)_{k+1}^{n+3/2} = \frac{1}{\Delta t} \left[\nabla \cdot \left(\frac{\rho^{n+1/2} + \rho_{k+1}^{n+3/2}}{2} \widehat{\mathbf{u}}_{k+1}^{n+1} \right) + \frac{\rho_{k+1}^{n+3/2} - \rho^{n+1/2}}{\Delta t} \right] \tag{2.57}$$

The correction is then applied to the velocity field through a projection step

$$\mathbf{u}_{k+1}^{n+1} = \widehat{\mathbf{u}}_{k+1}^{n+1} - \frac{2\Delta t}{\rho^{n+1/2} + \rho_{k+1}^{n+3/2}} \left(\nabla (\delta p)_k^{n+3/2} \right) \tag{2.58}$$

$$p_{k+1}^{n+3/2} = p_k^{n+3/2} + (\delta p)_{k+1}^{n+3/2} \tag{2.59}$$

5. Upon convergence of the subiterations, or when the maximum number of subiterations is reached, the solution is updated:

$$\rho^{n+3/2} = \rho_K^{n+3/2}, \quad p^{n+3/2} = p_K^{n+3/2}$$
$$\mathbf{u}^{n+1} = \mathbf{u}_K^{n+1}, \quad \mathbf{Y}^{n+3/2} = \mathbf{Y}_K^{n+3/2} \tag{2.60}$$

To avoid computing the full chemical Jacobian, $(\partial \mathbf{\Omega}/\partial \mathbf{Y})_k^{n+1}$, in the species transport equations, Savard et al. [88] proposed an approximation which requires only the diagonal. This formulation is used in this thesis.

The steps outlined above describe the semi-implicit iterative time integration method. If the Jacobian terms (e.g. $\partial \mathbf{C}/\partial \mathbf{Y}$, $\partial \mathbf{C}_u/\partial \mathbf{u}$, ...) are set to 0, then the time integration scheme becomes an explicit iterative scheme. The overall time integration

scheme is referred to as "semi-implicit" for three reasons. First, the implicit treatment is applied to each equation individually and successively and not to the overall system of equations all at once. Second, the implicit treatment for the momentum equation is not exact because the equation is quadratic in the velocity. Finally, the full chemical Jacobian is not evaluated.

Upon convergence of the subiterations, the previously described time integration scheme takes the general form:

$$\frac{\phi^{n+1} - \phi^n}{\Delta t} = f\left[\frac{1}{2}\left(\phi^n + \phi^{n+1}\right)\right] \tag{2.61}$$

This time integration scheme resembles the Crank-Nicolson scheme, but is based on the function evaluation at the midpoint value instead of the average of the function evaluated at the n and $n + 1$ timesteps. This discretization eliminates the need for storing the right hand side of the equation twice and allows for discrete energy conservation in time. Specifically, if both sides of Eq. (2.61) are multiplied by $(1/2)(\phi^n + \phi^{n+1})$, then we have:

$$\frac{1}{\Delta t}\left[\frac{1}{2}\left(\phi^{n+1}\right)^2 - \frac{1}{2}(\phi^n)^2\right] = f\left[\frac{1}{2}\left(\phi^n + \phi^{n+1}\right)\right]\left[\frac{1}{2}\left(\phi^n + \phi^{n+1}\right)\right] \tag{2.62}$$

The discrete spatial operators, Eqs. (2.48) and (2.49) ensure that the right hand side of Eq.(2.62) can be expressed in divergence form without the introduction of additional source terms [64, 89]. Thus, the change in the energy with time expressed by the left hand side of the equation depends solely on conserved spatial terms.

2.4.3 Immersed boundary method

Chapter 5 involves the simulation of an injector with a complicated geometry to obtain physically realistic inflow boundary conditions for the combustion chamber. To facilitate the simulation of the injector in the structured grid of NGA, we use the immersed boundary method. For a comprehensive overview of the different immersed boundary strategies, the reader is referred to the review papers by Mittal and Iaccarino [90] and Verzicco [91].

In NGA, we use a velocity reconstruction or interpolation method, similar to that proposed by Kang et al. [92]. Figure 2.2 shows an example of a solid body overlaid on a structured grid, with the edge of the solid body marked with the blue line. Generally speaking, the process is as follows. First, the velocity field is computed according to Eq. (A.3) without consideration of the immersed boundary. Then, cells within the solid region of the immersed boundary are set to zero velocity. For the

cells which are cut (neither fully solid nor fully fluid), the computed velocities on the uncut edges (green and pink faces) are no longer reliable due to the presence of the immersed boundary. The velocities on these edges are reconstructed via interpolation using velocities from neighbouring cells. Figure 2.2 shows an example of the interpolation stencil for the u velocity component in two dimensions. In the figure, the velocity at the pink face, u_c, is reconstructed using information from the closest reliable neighbouring points, $u_{i,j+1}$, $u_{i-1,j}$, and a point on the immersed boundary surface, u_{IB}, which has zero velocity due to the no-slip condition. Finally, velocity components on edges which are cut are set to zero velocity.
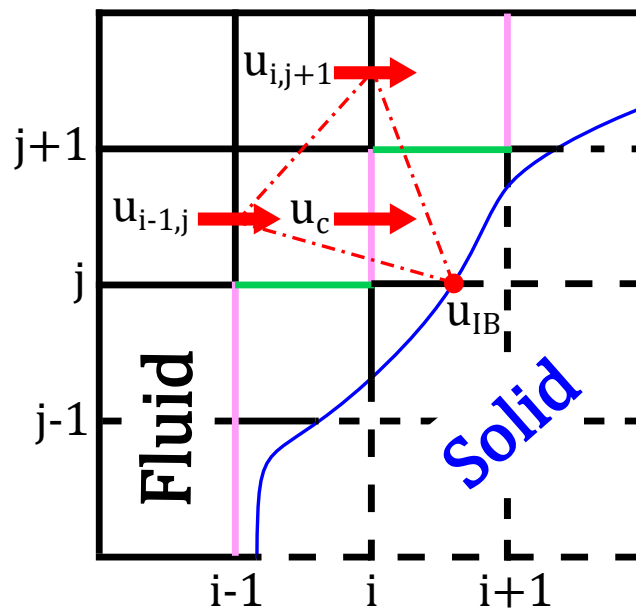
Figure 2.2: Example of interpolation points used to obtain velocity near the immersed boundary in two dimensions.

In a preprocessing step, a 3D STL file representing the geometry of the problem is compared with the grid to determine which cells are cut by the immersed boundary, and the location along each edge of the cell where the cut occurs. In NGA, the immersed boundaries do not move in space or time. As such, the interpolation coefficients are calculated in the initialization of the code, and do not change as the simulation progresses. The linear interpolation formula is given as:

$$u_c = \sum_{n=1}^{N} \gamma_n u_n + \gamma_{IB} u_{IB} \tag{2.63}$$

where $N = 2, 3$ for two- or three-dimensional problems, respectively, and γ are the

pre-computed interpolation weights, where

$$\sum_{n=1}^{N} \gamma_n + \gamma_{IB} = 1 \qquad (2.64)$$

The overall method is first-order accurate.

The velocity reconstruction described above does not satisfy continuity. To ensure global mass conservation, a correction is added to each of the interpolated velocities to ensure that the integral of the mass flux along the surface made from the uncut faces is equal to zero. Then, the Poisson equation, Eq. (A.4), is solved with zero gradient boundary conditions on the pink and green faces. Although this method ensures global mass conservation, it is noted that local mass conservation is not necessarily enforced.

Chapter 3

ISOLATING EFFECTS OF LARGE- AND SMALL-SCALE TURBULENCE ON THERMODIFFUSIVELY UNSTABLE PREMIXED HYDROGEN FLAMES

[1]   M. X. Yao and G. Blanquart. "Isolating effects of large and small scale turbulence on thermodiffusively unstable premixed hydrogen flames". In: *Combustion and Flame* (2024). (Under Review).

In this chapter, DNS are carried out using detailed chemistry and transport across a range of Karlovitz numbers and integral length scales to isolate effects of small-scale and large-scale turbulence. Sections 3.1 and 3.2 describe the problem setup and numerical details. Section 3.3 provides an overview of the results. In Section 3.4, the global effects and the local effects are decoupled to deconstruct the various components of Eq. (1.6) and develop a general expression for I_0. The local response of the flame is investigated in more detail in Section 3.5. The conclusions are drawn in Section 3.7.

3.1   Problem description

In this section, the physical problem and numerical methodology are presented.

3.1.1   Flow configuration

The inflow-outflow configuration [30, 32, 31, 43, 34, 35, 45] is commonly used to study turbulent premixed flames since it allows for the development of a statistically stationary, statistically planar, freely propagating flame without mean shear or strain. The computational domain is rectangular, with domain size $L_x \times L_y \times L_z$ with $N_x \times N_y \times N_z$ points in the x, y, and z directions, respectively, where x is the streamwise direction. The mean inlet velocity at $x = 0$ is set to match the turbulent flame speed such that the flame is stationary within the domain. The boundary condition at $x = L_x$ is a convective outflow. In these simulations, $L_y = L_z = L$, and the domain is periodic in both the y and z directions. The aspect ratio is $L_x/L = 8$. The grid resolution is the same in all three directions, that is, $\Delta x = \Delta y = \Delta z$. A schematic diagram of the flow configuration is shown in Fig. 3.1. The flame is represented by an isosurface of the temperature, and is coloured by the progress

variable source term. The effect of thermodiffusive instabilities are evident by the variations in the source term along the flame front. A detailed discussion of the turbulence generation is presented in the following sections.
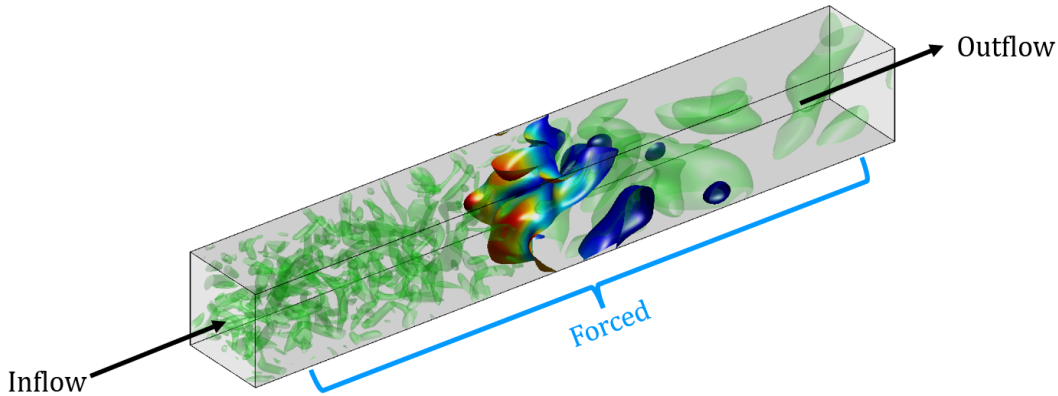
Figure 3.1: Schematic diagram of the DNS flow configuration.

3.1.2 Numerical method

The governing equations are solved using NGA [64], which is a fully conservative, finite-difference, code of arbitrarily high spatial order. In the present work, the spatial and temporal discretization are both second-order accurate. The time integration is conducted via the semi-implicit iterative Crank-Nicolson method [89]. The WENO5 [93] scheme is used for scalar transport. To reduce the computational cost associated with integrating the stiff chemistry in time, the preconditioning strategy of Savard et al. [88] is used.

The grid resolution must be sufficient to fully resolve both the turbulence and chemistry. As such, Δx is set to meet the more restrictive criteria between $k_{max}\eta_u > 1.5$ [94] and roughly 16 points per laminar flame thickness [73]. Here, $k_{max} = \pi/\Delta x$ is the maximum wavenumber which can be resolved on the grid. For hydrogen chemistry, Savard et al. [88] showed that the maximum stable timestep size could be increased from $\Delta t_{max} = 5.2 \times 10^{-8}$ s using an explicit integration to 1.6×10^{-6} s using the semi-implicit time integration. To ensure numerical stability, a slightly lower value was selected as the upper bound in the present simulations. As such, the timestep size is determined based on the more restrictive criteria between $\Delta t = 1 \times 10^{-6}$ s and the convective CFL, $\Delta t \leq 0.8\Delta x/\max(\mathbf{u})$ s.

3.1.3 Chemical model

The fuel mixture consists of hydrogen/air at an equivalence ratio of $\phi = 0.4$. The chemistry is described by the 9-species (see Table 4.1), 54-reaction mechanism proposed by Hong et al. [95] with a few updated rate constants [96, 97]. The chemical model is provided in supplemental material. In this work, the flames are burnt lean to reduce the maximum flame temperature. Since the flame temperatures are generally below 1800K (see Fig. 3.2), NOx is not expected for form [13]. Consequently, to reduce the computational cost, we do not include the NOx pathways in the chemical mechanism. Some important quantities from the one-dimensional, laminar, unstretched, freely propagating flame are summarized in Table 3.1. Consistent with typical studies of flamelets and flamelet modelling, the progress variable, C, is defined as the water mass fraction, Y_{H_2O}.

The flame thickness is defined as:

$$l_F = \frac{T_b - T_u}{\max\left(|\nabla T|\right)} \tag{3.1}$$

and S_L is the laminar flame speed. The subscripts u and b represent the unburnt and burnt mixtures, respectively. With thermal diffusion, the flame speed and peak source term are slightly increased, and the flame thickness is slightly decreased compared to the full transport. The thermal diffusion acts to push the H_2 and H molecules into the preheat zone and away from the reaction zone, thereby slightly reducing the peak source term. For the unity Lewis case, the flame speed is about two times larger, and the peak source term is about 3.7 larger. The quantity C_{peak} denotes the value of C in the one-dimensional flame where the peak source term, $\dot{\omega}_{C,max}^{1D}$, is located.

The nondimensional numbers in the following sections are defined based on values taken from the one-dimensional laminar flame with mixture average transport and thermal diffusion. Results from the three-dimensional flames are normalized by their respective one-dimensional flamelets.

3.1.4 Simulation parameters

A summary of the simulation cases is presented in Tables 3.2 and 3.3. To conduct a comprehensive study of the effect of turbulence on unstable lean premixed hydrogen flames, simulations are carried out at six different Karlovitz numbers (A through F) and four different integral length scales ($C_{0.5}$, C_1, C_2, and C_4). A fully laminar three-dimensional case is also included for reference (LAM). Cases A through

Table 3.1: Relevant parameters from one-dimensional laminar flames. "noSD" refers to the mixture-averaged formulation without Soret diffusion.

Parameter	Mix Avg SD	Mix Avg noSD	Unity Le
T_u [K]	298	298	298
ϕ	0.4	0.4	0.4
S_L [m/s]	0.206	0.215	0.410
δ [mm]	0.816	0.812	0.441
l_F [mm]	0.683	0.656	0.375
ν_u [m^2/s]	1.62×10^{-5}	1.62×10^{-5}	1.62×10^{-5}
C_{peak}	0.0835	0.0832	0.0815
C_{max}^{1D}	0.1033	0.1033	0.1033
$\dot{\omega}_{C,max}^{1D}$	52.57	54.84	195.63

C represent realistic conditions for practical combustors. Cases D through F are relevant for extreme cases such as those found in supernovae. As an additional point of comparison, cases A, B, and C_1 are also run without Soret diffusion, using both unity Lewis transport and mixture average formulations. These cases are summarized in Table 3.3, and are calculated using the same forcing coefficient and domain, thus maintaining the same turbulence properties (e.g., turbulent kinetic energy, dissipation, etc.). However, as noted in Table 3.1, the laminar flame speed and thickness are different, and as such, the Karlovitz number and integral length scale ratio are different. In Table 3.3, unity Lewis cases are denoted with a superscript Le, and mixture-averaged cases with no Soret diffusion are denoted with a superscript $noSD$.

The unburnt Karlovitz number is defined based on the ratio of flame and turbulence timescales:

$$Ka_u = \frac{\tau_F}{\tau_\eta} = \frac{l_F}{S_L} \left(\frac{\varepsilon}{\nu_u} \right)^{1/2} \tag{3.2}$$

where ε is the dissipation, and ν_u is the kinematic viscosity. The flame timescale, τ_F, is defined as l_F/S_L, and the Kolmogorov timescale, τ_η, is $\sqrt{\nu_u/\varepsilon}$. The unburnt turbulent Reynolds number is defined as:

$$Re_t = \frac{u'\ell}{\nu_u} \tag{3.3}$$

where u' is the turbulent intensity (rms velocity), and ℓ is the integral length scale.

The Karlovitz number, integral length scale, and turbulent intensity are often used to characterize the burning regime and are related through the following expres-

sion [98]:

$$\frac{u'}{S_L} = Ka_u^{2/3} \left(\frac{\ell}{l_F}\right)^{1/3} \tag{3.4}$$

with the assumption that $S_L l_F = \nu$. In this study, the integral length scale effects are tested at a fixed Karlovitz number, contrary to other studies which may instead choose to hold u'/s_L constant [99]. In this way, the flame is subject to an identical level of small-scale turbulence, and the effect of the integral length scale can be decoupled from the turbulence intensity and studied in isolation.

Table 3.2: Parameters of the simulations with full mixture average transport and Soret diffusion.

Case	A	B	$C_{0.5}$	C_1	C_2	C_4	D	E	F	LAM
Ka_u	15	60	167	167	167	167	450	900	1900	-
Re_t	24.13	60.79	47.05	118.55	298.76	763.80	229.29	363.97	598.97	-
L [mm]	4.03	4.03	2.01	4.03	8.06	16.1	4.03	4.03	4.03	4.03
ℓ/l_F	1	1	0.5	1	2	4	1	1	1	-
B [s^{-1}]	314	792	2452	1545	973	622	2987	4742	7803	0
u'_0/S_L	2.95	7.43	11.50	14.50	18.27	23.35	28.04	44.51	73.24	0

Table 3.3: Parameters of the simulations with no Soret diffusion. Superscript Le refers to unity Lewis cases, and $noSD$ refers to mixture average cases.

Case	A^{Le}	A^{noSD}	B^{Le}	B^{noSD}	C_1^{Le}	C_1^{noSD}
Ka_u	4.4	14.14	17.5	56.58	47.6	154.07
Re_t	24.13	24.13	60.79	60.79	118.55	118.55
L [mm]	4.03	4.03	4.03	4.03	4.03	4.03
ℓ/l_F	1.72	0.98	1.72	0.98	1.72	0.98
B [s^{-1}]	314	314	792	792	1545	1545
u'_0/S_L	1.48	2.83	3.73	7.12	7.28	13.89

3.2 Turbulence forcing

The flow configuration does not have any large-scale mean shear to generate the turbulence, such as in other studies [100]. Consequently, any injected turbulence would decay as it travels downstream. To prevent this, the flow must be forced across the domain in order to maintain a desired turbulence level. This forcing reproduces the effects of any mean shear not present in the simulation domain [101, 29].

The forcing vector, $\mathbf{f}$, in the momentum equation is the linear forcing of Lundgren [102, 103] with the modification of Carroll and Blanquart [104]. This is written as:

$$\mathbf{f} = B\frac{k_0}{k(x,t)}\left(\rho\mathbf{u} - \overline{\rho\mathbf{u}}(x,t)\right) \tag{3.5}$$

where the bar represents the planar Reynolds average:

$$\overline{\phi} = \frac{1}{L^2} \int_0^L \int_0^L \phi \, dy \, dz \tag{3.6}$$

Here, k_0 represents the target turbulence kinetic energy (TKE), and

$$k = \frac{1}{2} \left(\widetilde{(u'')} + \widetilde{(v'')^2} + \widetilde{(w'')}^2 \right) \tag{3.7}$$

is planar Favre-averaged TKE. The Favre averaging is defined as:

$$\widetilde{\phi} = \frac{\overline{\rho\phi}}{\overline{\rho}} \tag{3.8}$$

with the corresponding fluctuating component

$$\phi'' = \phi - \widetilde{\phi} \tag{3.9}$$

This forcing technique has been used by many authors and validated in detail by Lapointe et al. [31] and Bobbitt et al. [32].

The forcing coefficient, B, directly controls the turbulence quantities of interest. For a given domain size (in the periodic directions), L, the integral length scale is empirically determined to be approximately $\ell \approx 0.16L$ [32]. For a statistically stationary flow, the nominal values for the rms perturbations, u_0', TKE, k_0, dissipation, ε_0, and eddy turnover time, τ_0, are analytically derived to be [104]:

$$u_0' = 3B\ell \tag{3.10}$$

$$k_0 = \frac{27}{2} B^2 \ell^2 \tag{3.11}$$

$$\varepsilon_0 = 27B^3 \ell^2 \tag{3.12}$$

$$\tau_0 = \frac{1}{2B} \tag{3.13}$$

The reported Ka_u numbers are the nominal values given in terms of ε_0, which is directly controlled by B. Typically, the Karlovitz number is an output of the turbulence intensity. However, to conduct a simulation at a target Ka_u, the forcing coefficient is instead backed out:

$$B = \left(\frac{1}{27} \frac{Ka_u^2 \nu_u S_L^2}{(0.16L)^2 l_F^2} \right)^{1/3} \tag{3.14}$$

Turbulence is forced for the first 85% of the domain. Then, the forcing coefficient is relaxed to 0 through a complementary error function in order to prevent negative velocities at the outlet.

To ensure realistic turbulence, an inflow file is generated from a simulation of homogenous isotropic turbulence (HIT). At each timestep, turbulent fluctuations from the HIT are superimposed onto a bulk mean velocity at the inlet. The fluctuations are initially smaller than the mean inlet velocity to prevent negative inflow conditions and grow naturally to their nominal values with the forcing.

3.3 Overview of results

In this section, we provide an overview of the effect of turbulence intensity on the turbulent flame brush. This discussion is meant to be qualitative in nature, and not quantitative. Figures 3.2 and 3.3 show two-dimensional slices of the temperature field for the tested cases. Due to the thermodiffusive instabilities, the three-dimensional laminar flame (LAM) is not planar and exhibits cellular structures. The post-flame temperature is seen to vary along the flame front. The curvature is defined to be positive when the center of curvature is located in the burnt mixture. The temperature is relatively higher in regions of positive curvature, and lower in regions of negative curvature [105]. The preferential diffusion of H_2 concentrates the species into regions of positive curvature, creating a locally rich mixture which enhances the burning. The opposite is true for regions of negative curvature. The mismatch in local propagation speeds creates cellular structures which point toward the burnt mixture.

Figure 3.2 shows the effect of increasing the Karlovitz number at a fixed integral length scale ratio $\ell/l_F = 1$. For the lowest Karlovitz number, the flame exhibits a dominant structure with a continuous flame front. As the Karlovitz number increases, up until $Ka = 450$ (case D), the length scales of the structures at the flame front decrease. The flame front is increasingly disrupted by the turbulence, increasing the amount of small-scale features, leading to a significant increase in the turbulent flame area. The flame front appears more broken as pockets of burnt and unburnt gases are mixed by the turbulence. Due to the thermodiffusive instabilities, the temperature field in the burnt mixture is highly inhomogeneous. At the highest Karlovitz number, $Ka = 1900$ (case F), the turbulent flame brush becomes significantly shorter, and the mixing is smoother as there are fewer disconnected pockets of fluid. Qualitatively, flame F appears similar to thermodiffusively stable high Karlovitz number hydrocarbon flames [31].

Figure 3.3 shows the effect of changing the integral length scale at a fixed Karlovitz number. As the integral length scale is increased, the flame presents significantly
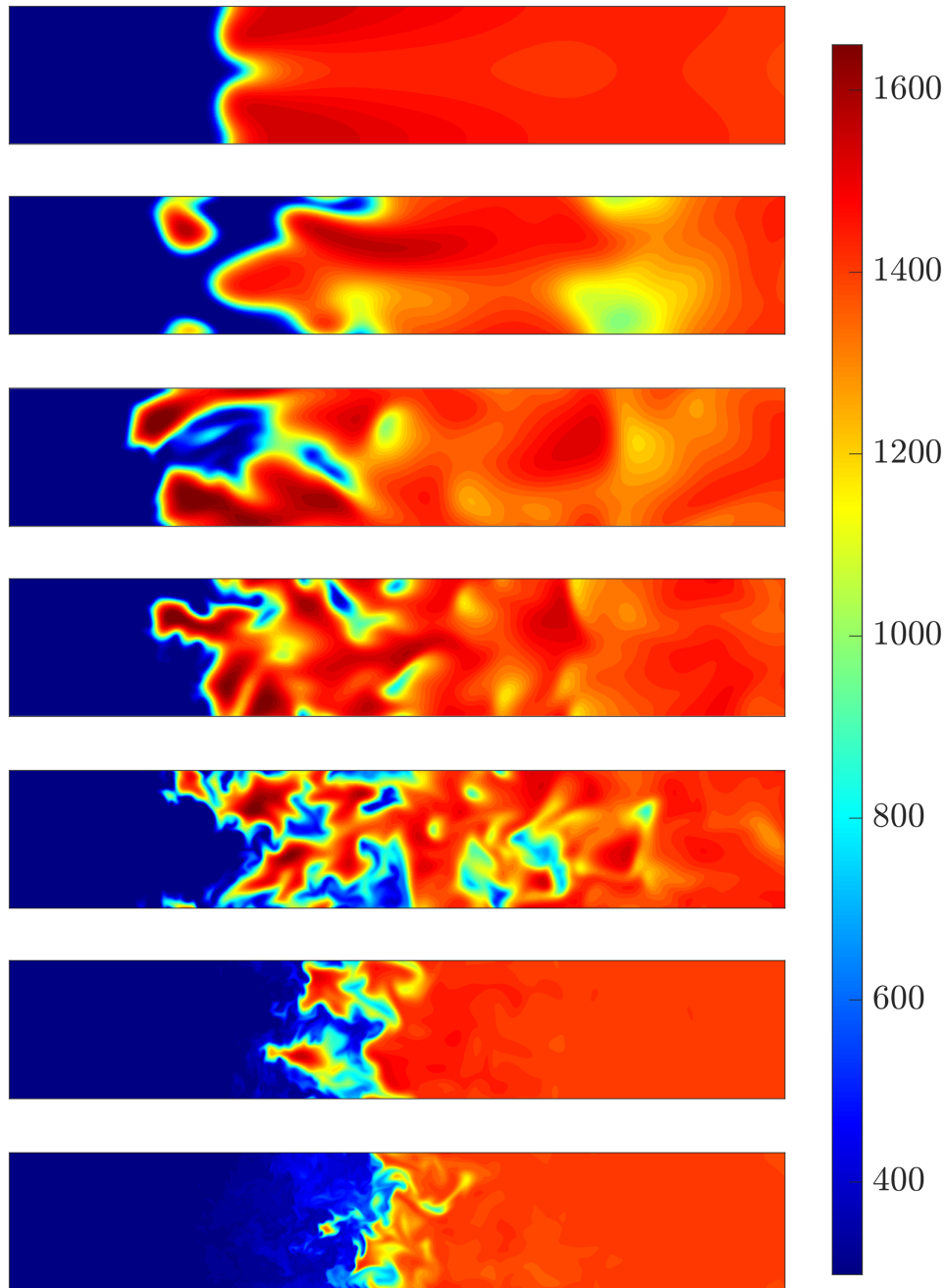
Figure 3.2: Two-dimensional slices of temperature field in the region of the flame. From top to bottom: cases LAM, A, B, C_1, D, E, and F.

more disconnected regions as pockets of unburnt gases are mixed into the burnt mixture, increasing the turbulent flame area. Despite the smaller domain size restricting the volume that the flame can grow in, the structures at the flame front are qualitatively of the same size. It is important to note that for all four cases, the Karlovitz number was kept constant by maintaining the same energy dissipation
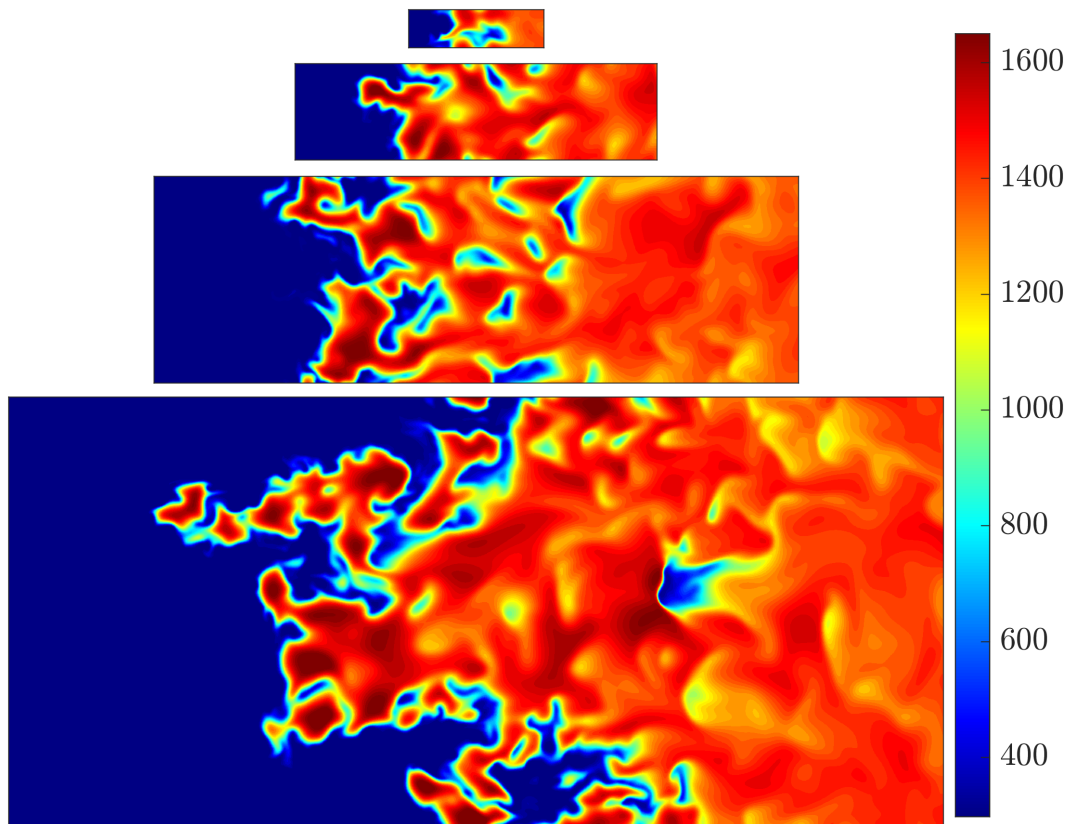
Figure 3.3: Two-dimensional slices of temperature field in the region of the flame. From top to bottom: cases $C_{0.5}$, C_1, C_2, and C_4. The figures are scaled to represent accurately the differences in physical length scales.

rate. Specifically, in the definition of the Karlovitz number, all values are constants except for the dissipation, ε_0. As the integral length scale changes, the forcing coefficient is chosen to keep ε_0 constant according to Eq. (3.12). Although the large-scale turbulence that the flames are subject to is changing, the flames are still subject to the same small-scale turbulence. Thus, it is reasonable that the flames exhibit similar small-scale structures.

3.4 Global properties

The burning efficiency model of Eq. (1.6) aims to explain the relationship between two global quantities: the turbulent flame speed and area. In this section, a detailed study of the turbulent flame speed and area is conducted. Then, an expression for the burning efficiency is proposed.

3.4.1 Turbulent flame speed

From integrating the continuity and water mass fraction equations, the turbulent flame speed is defined as the volume integral of the progress variable production rate:

$$S_T = \frac{1}{\rho_u C_b A} \int_V \dot{\omega}_C dV \tag{3.15}$$

where $A = L \times L$ is the cross-sectional area. An example of the temporal evolution of the turbulent flame speed is shown in Fig. 3.4a for the different Karlovitz numbers. The mean turbulent flame speeds are shown in Fig. 3.4b as a function of the Karlovitz number. The turbulent flame speed increases with the Karlovitz number up to Case D, after which the flame speed decreases. A similar trend was noted by Aspden et al. [20]. Consistent with their results, we find that there is a 1/3 scaling on the Karlovitz number up to case D. In our simulations, the ratio ℓ/l_F is fixed. As such, the scaling between the Reynolds and Karlovitz numbers is given as $Re_t \propto Ka_u^{2/3}$, and hence the turbulent flame speed scales as $Re_t^{1/2}$. A 1/2 power on the Reynolds number was also measured experimentally by Liu et al. [106] for spherically expanding flames with $Le < 1$ based on the theory of Chaudhuri et al. [107]. It is interesting to contrast this to the 1/2 scaling on the Karlovitz number reported by Howarth et al. [39] for the surface-mean local flame propagation speed. The turbulent flame speeds are strongly dependent on the integral length scale ratio varying by a factor of almost 6 from the smallest to largest integral length scales. The inclusion of Soret diffusion results in a higher normalized mean flame speed by about 35% for case A to 15% for case C, compared to the value of 8% reported by Song et al. [45] for thermodiffusively stable flames.

One of the key attributes of the thermodiffusively unstable flames is the existence of superadiabatic burning, that is, burning in regions where the progress variable is higher than the nominal one-dimensional equilibrium value, C_{max}^{1D}. To quantify how much the superadiabatic burning regions contribute to the flame speed, Eq. (3.15) can be split to account for it explicitly:

$$S_T = \frac{1}{\rho_u C_b A} \left[\int_V \dot{\omega}_C \left(C \leq C_{max}^{1D} \right) dV + \int_V \dot{\omega}_C \left(C > C_{max}^{1D} \right) dV \right] \tag{3.16}$$

From this, the superadiabatic ratio is defined as:

$$\beta \equiv \frac{\int_V \dot{\omega}_C \left(C > C_{max}^{1D} \right) dV}{\int_V \dot{\omega}_C dV} \tag{3.17}$$

and represents the percentage of S_T which is attributed to superadiabatic burning. Figure 3.5 shows β for the tested cases. For the laminar case, about 30% of the

(a) Instantaneous

(b) Mean
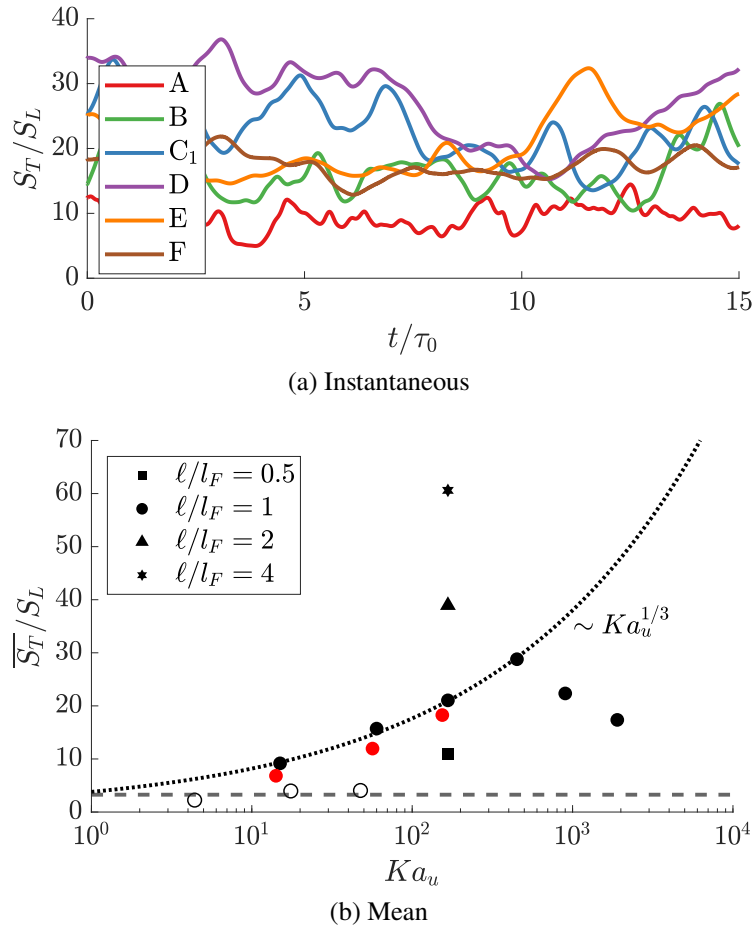
Figure 3.4: Instantaneous (a) and mean (b) normalized turbulent flame speed. Black symbols represent full transport cases, red symbols represent no Soret cases, and open symbols represent unity Lewis cases.

flame speed can be attributed to superadiabatic burning. This value is approximately constant at 40% for cases A through C_1, before decaying rapidly to 13% for case F. This decrease also quantifies the decrease of differential diffusion effects at high Karlovitz numbers. The reduced contribution of the superadiabatic burning at the highest Karlovitz numbers is consistent with the qualitative observations from Fig. 3.2. This rapid reduction in the relative importance of superadiabatic burning may also explain the decrease in turbulent flame speeds after case D in Fig. 3.4b. Finally, the superadiabatic ratio does not appear to depend on the integral length scale, as for cases $C_{0.5}$-C_4, there is a scatter of about ±0.023 without any monotonic trend. In contrast, including Soret diffusion leads to systematically more superadiabatic burning with an increase in the ratio by about 0.065.

To explain the evolution of the turbulent flame speed, it is insightful to rewrite any
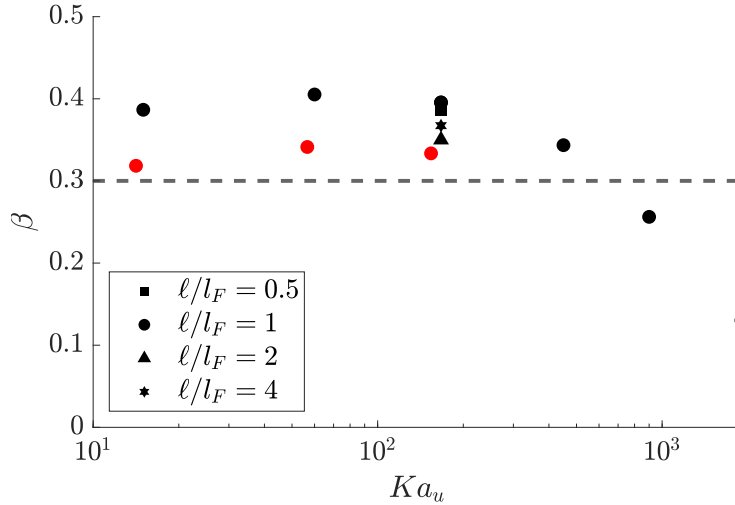
Figure 3.5: Ratio of turbulent flame speed which is attributed to superadiabatic burning. The dashed line represents case LAM, black symbols represent full transport cases, and red symbols represent cases with no Soret diffusion.

volumetric integral as a surface integral along an isocontour of C and an integral in the normal direction:

$$\int_V \dot{\omega}_C dV = \int_n \left(\iint_{A(C)} \dot{\omega}_C dA \right) dn \tag{3.18}$$

Taking $dn = dC/|\nabla C|$, Eq. (3.18) can be rewritten as:

$$\int_V \dot{\omega}_C dV = \int_C \iint_{A(C)} \frac{\dot{\omega}_C}{|\nabla C|} dA dC \tag{3.19}$$

and the turbulent flame speed can be written as:

$$S_T = \frac{1}{1-\beta} \frac{1}{\rho_u C_b A} \int_0^{C_{max}^{1D}} \left\langle \frac{\dot{\omega}_C}{|\nabla C|} \middle| C \right\rangle A(C) dC \tag{3.20}$$

The turbulent flame speed can be interpreted as a convolution of the area of the flame isosurface, $A(C)$, with the gradient-weighted conditional mean source term.

Turbulence can thus impact the flame speed through one of two main pathways. The first pathway is through local effects induced by the turbulence on the mean source term, $\left\langle \frac{\dot{\omega}_C}{|\nabla C|} | C \right\rangle$. As the small-scale turbulence penetrates the flame, it alters the flame structure through enhanced mixing and diffusion. The second pathway is through the area of flame isosurfaces, $A(C)$. As the larger-scale turbulence perturbs the flame front, it wrinkles the flame, altering the curvature, κ, and necessarily increasing the flame area. These effects are detailed in the following subsections.

3.4.2 Area of flame isosurfaces

Previous studies have identified the instantaneous flame front as the isosurface of either T_{peak} or C_{peak} [43, 108]. The flame area is then subsequently calculated as the area of that isosurface. However, the presence of thermodiffusive instabilities in the current simulations necessitate some nuances on the definition of the flame area.

Fundamentally, the flame front is described as the location where the reactions are occurring. Figure 3.6 shows the temperature and the normalized source term with isocontours of C from case A. From the upper plot, it can be seen that the isocontours are irregularly spaced, indicating that the flame area varies depending on the value of C chosen as the isocontour value. From the lower plot, along the isocontour of C_{peak}, the source term varies with the curvature of the isocontour. In regions of positive curvature (center of curvature in burnt mixture), the source term is about 7.5 times larger than the maximum source term from the one-dimensional flame. The curvature concentrates the differential diffusion into these regions, and as a result, the mixture becomes locally richer and the burning is significantly enhanced. Hydrogen diffuses out of regions of negative curvature, creating locally leaner mixtures, and the source term reduces. Interestingly, the source term plot shows a pocket of non-burning low temperature mixture which has been engulfed into the burnt mixture and is captured by the isosurface of C_{peak}. This artificially increases the flame area, and the effects can become more pronounced as the flow fields become more complex with higher levels of turbulence, as shown in Fig. 3.2.

To illustrate the effect of the isosurface value selection, Fig. 3.7 shows the normalized area of isosurfaces as a function of C, $A(C)/A$, for the various Karlovitz number flames. The isosurfaces are created using the classical marching cubes method [109]. For each value of C, an isosurface is created using the marching cubes algorithm, which is then used to calculate the area, $A(C)$. The $A(C)$ profiles may be decomposed into two regions. At lower values of the progress variable (for $C < C_{peak}$), $A(C)$ increases modestly with progress variable. At a fixed C, it increases monotonically with the Karlovitz number from case LAM to case D. Such an increase is expected: more intense turbulence means more flame wrinkling and hence a larger isosurface area. At larger values of the progress variable (for $C > C_{peak}$), $A(C)$ increases sharply with progress variable before reaching a large spike at $C = C_{max}^{1D}$, with a subsequent drop-off to 0. The spike is indicative of the strong post-flame inhomogeneities present due to differential diffusion effects. In both regions, as the Karlovitz number is further increased (cases E and F), the
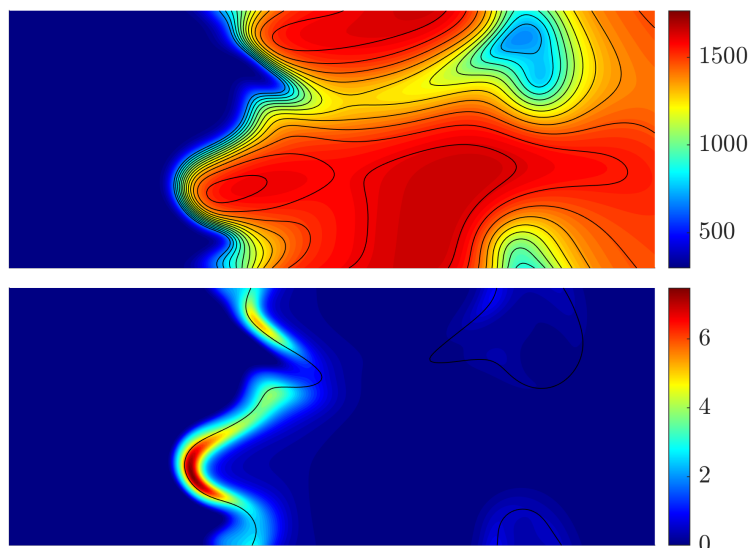
Figure 3.6: Temperature, T (top), and normalized source term, $\dot{\omega}_C/\dot{\omega}_{C,max}^{1D}$ (bottom) for case A. Black isolines on the temperature represent 0.4 to 1.6 times C_{peak} in increments of 0.1. The black isoline on the source term is at C_{peak}.

differential diffusion effects are suppressed. This translates into overall flatter $A(C)$ profiles, with smaller spikes and quicker decay to zero in superadiabatic regions ($C > C_{max}^{1D}$).
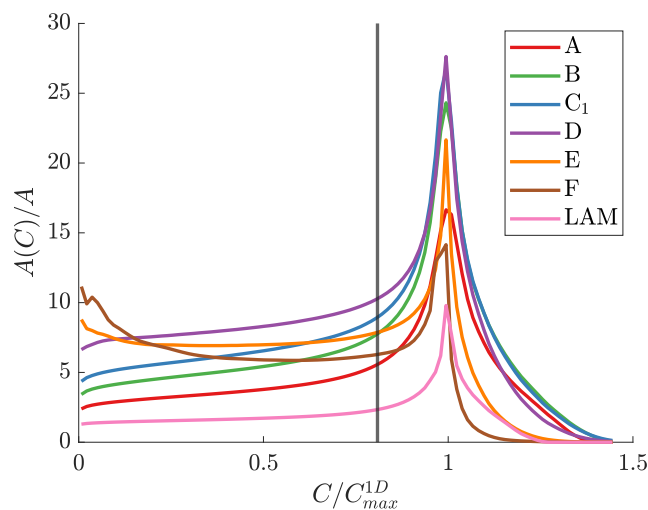
Figure 3.7: Normalized area of flame isosurfaces as a function of normalized progress variable for flames at $\ell/l_F = 1$. The vertical line denotes the location of C_{peak}.

The influence of the integral length scale on the flame area is shown in Fig. 3.8. Figure 3.8a shows the effect of the integral length scale ratio on the flame isosurface area for cases C_x. As ℓ/l_F is increased, the ratio $A(C)/A$ increases systematically.

The larger integral length scales introduce more large-scale wrinkling. A linear dependence was observed for turbulent hydrocarbon flames by Lapointe [110]. To investigate this dependence further, Fig. 3.8b shows $A(C)/A$ scaled by ℓ/l_F. The profiles are almost collapsed, indicating that $A(C)/A$ scales almost linearly with the integral length scale ratio. In the present simulations, the domain size and integral length scale are inseparably linked since $\ell \approx 0.16L$ [32].

As pointed out by Aspden [20], it is unclear if the domain size or the integral length scale are the cause of the linear trend of the ratio $A(C)/A$. To elucidate their individual contributions, a single snapshot of case C_2 is decomposed into four quadrants. Each quadrant is characterized by the same integral length scale as the original full domain, but has a reduced domain width by a factor of 2. The normalized flame isosurface areas for all four quadrants and the full domain are shown in Fig. 3.8c. The overlapping profiles indicate that the ratio $A(C)/A$ is independent of the domain width. The domain width does impact the flame isosurface area $A(C)$ through the cross-sectional area $A = L^2$, but not their ratio.

3.4.3 Turbulent flame area

Given the large variations in $A(C)$, defining a single A_T value for a given flame presents some arbitrariness, and hence different definitions may be proposed.

Inspired by Eq. (3.20), a natural definition is to use a source term-weighted average flame area:

$$A_T \equiv \frac{\displaystyle\int_0^{C_{max}^{1D}} \left\langle \frac{\dot{\omega}_C}{|\nabla C|} \Big| C \right\rangle A(C)\mathrm{d}C}{\displaystyle\int_0^{C_{max}^{1D}} \left\langle \frac{\dot{\omega}_C}{|\nabla C|} \Big| C \right\rangle \mathrm{d}C} \tag{3.21}$$

The weighting gives more importance to areas with enhanced burning at the flame front, and significantly reduces the contribution of non-burning regions, such as those shown in Fig. 3.6. Figure 3.9 shows the area of flame isosurfaces for case A. For the stable unity Lewis number case, the flame area is approximately constant regardless of the chosen isosurface value. This constant value is well reproduced by the source term-weighted average flame area. For the full transport case, the turbulent flame area calculated using Eq. (3.21) intersects the plot of $A(C)$ approximately at C_{peak}.

The influences of the Karlovitz number and integral length on the mean turbulent flame areas are shown in Fig. 3.10. The area exhibits some dependence on the Karlovitz number, increasing from about 2.3 for the LAM case to about 10.3 for case

(a) Effect of integral length scale

(b) Scaled by integral length scale ratio

(c) A snapshot of case C_2 (line), compared to the flame isosurface area for each quarter of the domain (markers).
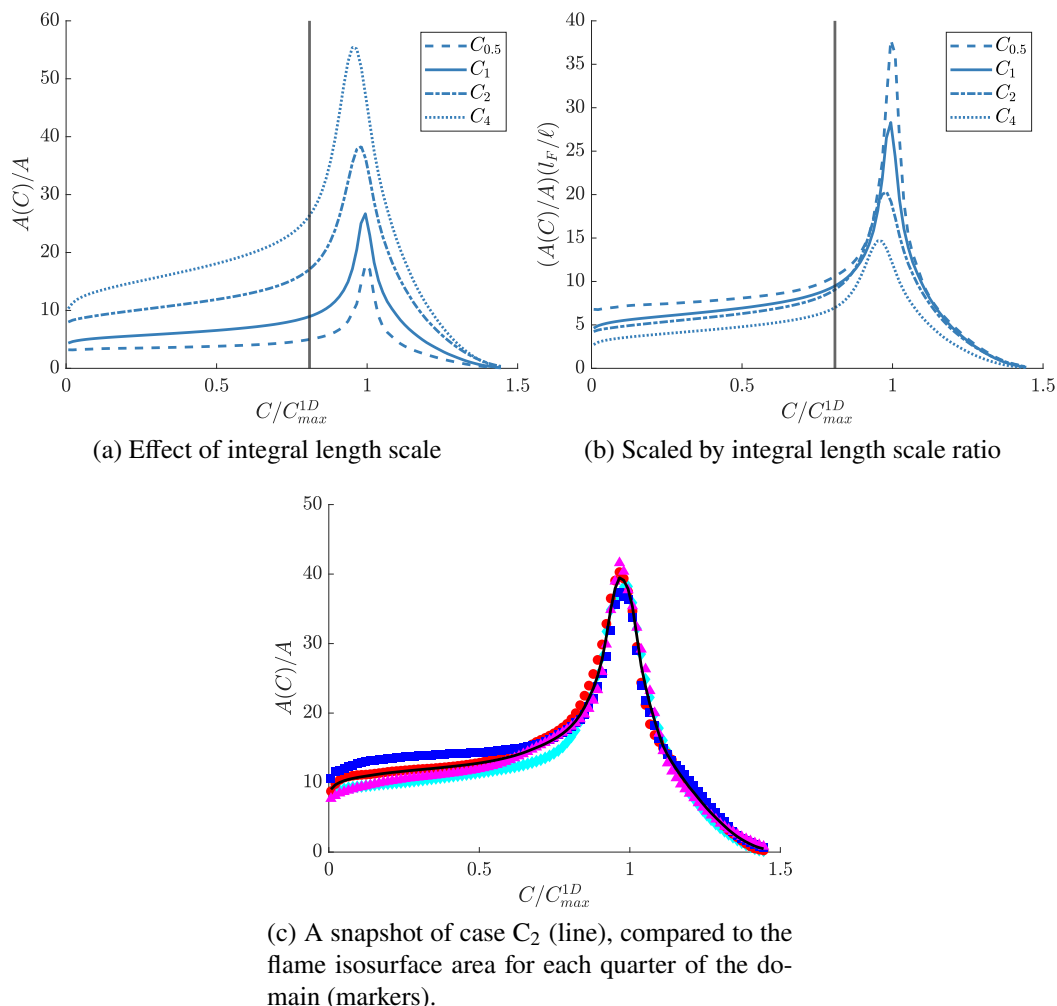
Figure 3.8: Effect of integral length scale and domain area on the flame isosurface area.

D. The dependence on the integral length scale is stronger. The flame area increase follows a linear trend for the first three integral length scale ratios, before deviating from the trend at $\ell/l_F = 4$. Fig. 3.10b also shows an empirical $\propto (\ell/l_F)^{0.75}$ trend for comparison, which fits the data better at higher integral length scale ratios. Based on the current results, it is not possible to say whether the trend is generalizable to larger integral length scale ratios. These observations are consistent with the results shown in Fig. 3.8. In hydrocarbon flames, Lapointe [110] found a linear dependence of A_T/A on ℓ/l_F, up to an integral length scale ratio of 4, and Song et al. [36] found similar trends for thermodiffusively stable premixed hydrogen flames up to an integral length scale ratio of 6. In all cases, the turbulent flame areas calculated by Eq. (3.21) are very close to the values obtained from the isosurface
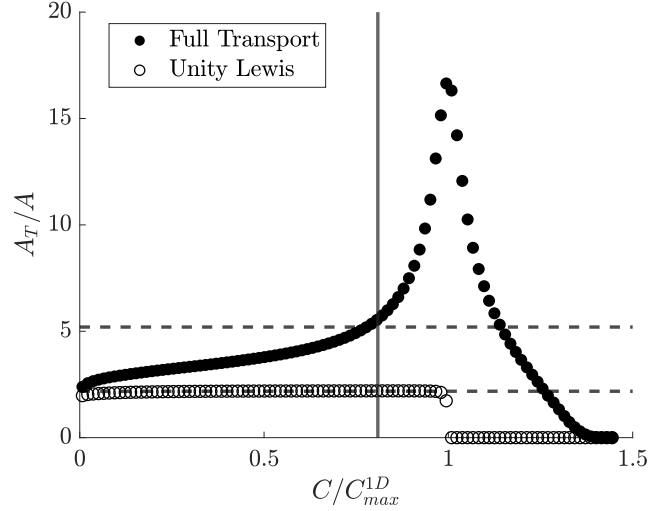
Figure 3.9: Area of flame isosurfaces as a function of progress variable for flame A with full transport and unity Lewis transport (open symbols). The dashed lines correspond to the mean turbulent flame areas calculated using Eq. (3.21). The vertical line denotes the location of C_{peak}.

area of C_{peak}.

The decrease of A_T/A at the highest Karlovitz numbers is hypothesized to be attributed to two main sources. The first is that the flame becomes too broad, and the domain is too small to accommodate the associated large-scale wrinkling (see section 3.3). The second is that the thermodiffusive instabilities are suppressed as the effective Lewis number approaches unity, thereby reducing the flame area which was being enhanced. The reduction of the effective Lewis number was quantified by Savard and Blanquart [19] for simulations without Soret diffusion.

3.4.4   Burning efficiency

The turbulent flame speed and area are related to each other through the burning efficiency parameter from Eq. (1.6). As such, the definition of the turbulent flame area is intrinsically linked to that of the burning efficiency.

Taking the expressions for S_T and A_T from Eqs. (3.20) and (3.21), S_T/S_L can be written as:

$$\frac{S_T}{S_L} = \frac{1}{1-\beta} \frac{\int_0^{C_{max}^{1D}} \left\langle \frac{\dot{\omega}_C}{|\nabla C|} \middle| C \right\rangle \mathrm{d}C}{\int_0^{C_{max}^{1D}} \frac{\dot{\omega}_C^{lam}}{|\nabla C|^{lam}} \mathrm{d}C} \frac{A_T}{A} \tag{3.22}$$
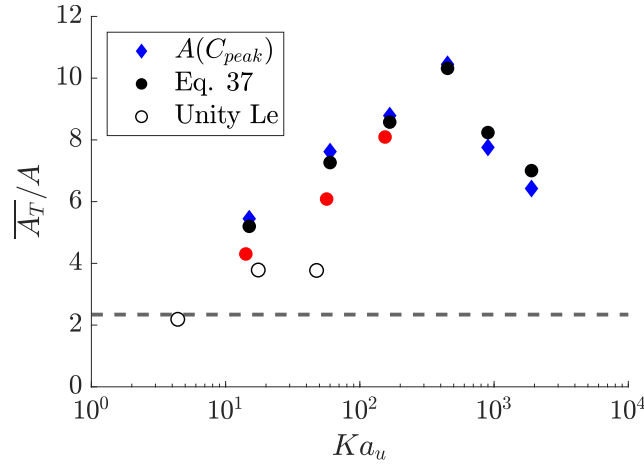
(a) Effects of Karlovitz number at a fixed $\ell/l_F = 1$.
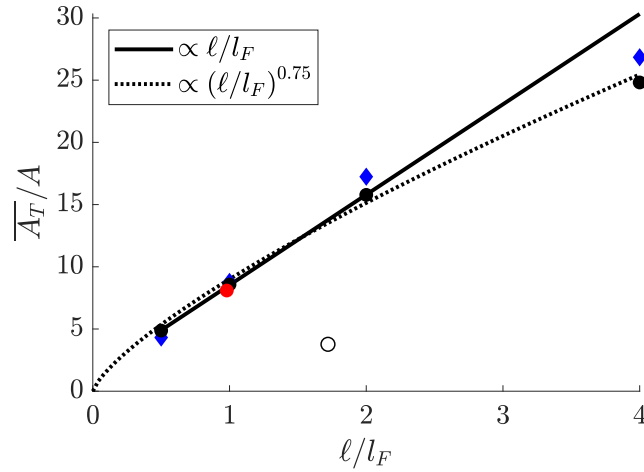
(b) Effects of integral length scale ratio for case C conditions.
The solid line is a linear trend fit to the first three data points.

Figure 3.10: Impact of the Karlovitz number (a) and integral length scale ratio (b) on the mean normalized turbulent flame area. Black symbols represent full transport cases, open symbols represent unity Lewis number cases, and red symbols represent no Soret cases. The dashed line in (a) represents case LAM.

This equation is mathematically equivalent to Eq. (1.6) with

$$I_0 \equiv \frac{1}{1 - \beta} \frac{\int_0^{C_{max}^{1D}} \left\langle \frac{\dot{\omega}_C}{|\nabla C|} \middle| C \right\rangle \mathrm{d}C}{\int_0^{C_{max}^{1D}} \frac{\dot{\omega}_C^{lam}}{|\nabla C|^{lam}} \mathrm{d}C} \tag{3.23}$$

The burning efficiency provides a way to relate two global quantities, S_T and A_T. To study local flame behaviour, Howarth et al. [39] proposed a predictive empirical model for the surface-mean local flame propagation speed. The expression for I_0 is a generalization of the one proposed by Lapointe and Blanquart [43], as it does not

rely on the key assumption that the source term scales with its value at C_{peak}. The calculated values of I_0 are plotted in Fig. 3.11. There are three key observations.
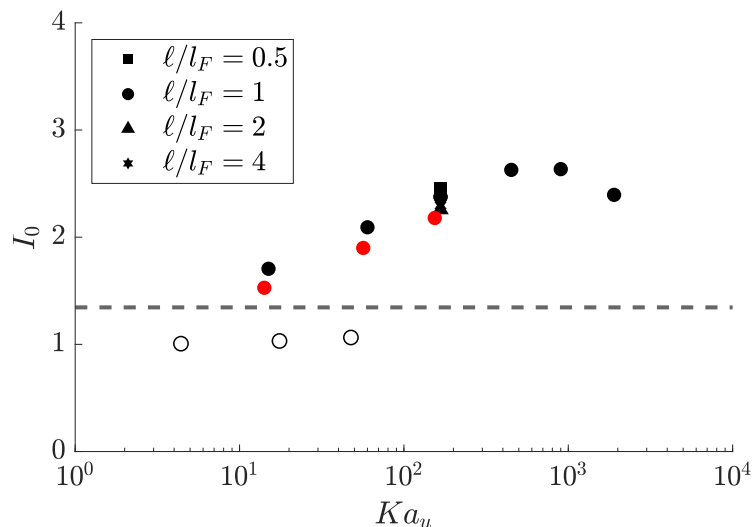
Figure 3.11: Burning efficiency as calculated by Eq. (3.23) versus Karlovitz number. The dashed line is obtained from case LAM. Black symbols represent full transport cases, open symbols represent unity Lewis solutions, and red symbols represent cases with no Soret diffusion.

First, at a fixed Karlovitz number, the burning efficiency appears to be almost independent of the integral length scale. For cases $C_{0.5}$ through C_4, I_0 falls within the range of 2.26 to 2.45.

Second, the burning efficiency increases with the Karlovitz number up until case D, and then decreases at case F. At low turbulence intensities, the burning efficiency asymptotes to the value from case LAM. Notably, due to the thermodiffusive instabilities, the burning efficiency of the laminar case is 1.35, indicating that the instabilities play a role in the burning efficiency enhancement. At the high Karlovitz numbers, the decrease in the burning efficiency is consistent with the decrease observed in the superadiabatic ratio. Following Fig. 3.5, at the highest Karlovitz numbers, differential diffusion effects are virtually suppressed. Consequently, the relevant laminar flame speed would be that of a unity Lewis number flame, which is larger than that with full transport (see Table 3.1). Since the current results are calculated based on the nominal S_L for full transport, the values of I_0 are inflated at higher Ka_u.

Finally, the cases without Soret diffusion are systematically lower than those with, ranging from a 8.3% to 10.4% decrease in the burning efficiency. The decreases

observed in the flame speed and flame area are further characterized by a lower burning efficiency.

3.4.5 Comparison of burning efficiency expressions

In this work, an expression for the burning efficiency was proposed in Eq. (3.23). This can be compared to the expression proposed by Lapointe and Blanquart [43] in Eq. (1.7). Their expression relies on the fundamental assumption that the source terms and gradients scale locally with their value at C_{peak}. Stated differently, the conditional mean turbulent profiles have the same shape as the laminar profiles. The new expression does not make such an assumption, and depends on the full profiles. The addition of the superadiabatic ratio, β, further incorporates the effects of superadiabatic burning, which do not exist in the stable hydrocarbon flames investigated by Lapointe and Blanquart [43].

A comparison of the expressions is shown in Fig. 3.12. For the thermodiffusively stable flames of Lapointe and Blanquart [43], the two expressions show strong agreement. The same can be said for the unity Lewis number cases of the present work. However, for the thermodiffusively unstable flames, the two expressions produce drastically different results, with Eq. (1.7) systematically underestimating I_0. The incorporation of the superadiabatic ratio and the full source term profiles are necessary to obtain correct values of I_0 for thermodiffusively unstable flames. Note that, to eliminate the effect of different ambient temperatures when comparing results with previous simulations [31], we used the reaction zone Karlovitz number:

$$Ka_\delta = \frac{\delta^2}{\eta_\delta^2} \tag{3.24}$$

where η_δ is the Kolmogorov length scale calculated using ν at C_{peak}. The local flame response, including the source term, is discussed in the following section.

3.5 Local flame response

As described in Eq. (3.23), the burning efficiency is dictated by the local response of the flame to the imposed turbulence. In this section, we explore the interplay between chemical source term, turbulence, and flame curvature.

3.5.1 Chemical source term

The conditional mean progress variable source term profiles are plotted in Fig. 3.13. Consistent with the previous observation related to the burning efficiency, at a given Karlovitz number, the source term profiles in Fig. 3.13a show only a weak
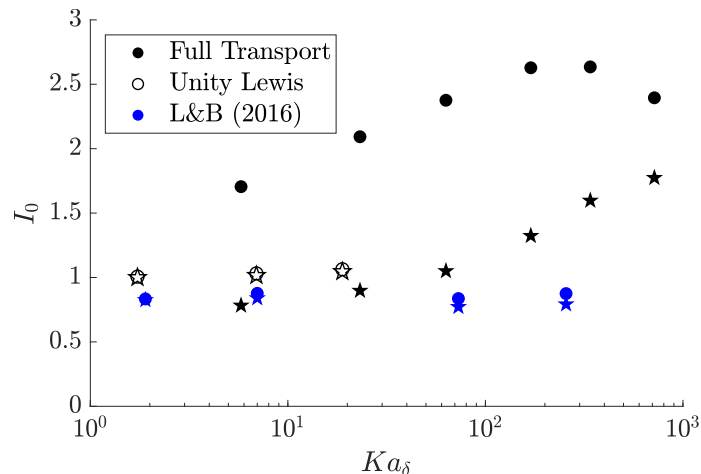
Figure 3.12: Comparison of I_0 calculated using Eq. (3.23) (circles) and Eq. (1.7) (stars) for the *n*-heptane flames of Lapointe and Blanquart [43] (blue symbols), the present lean hydrogen flames with full transport (black symbols), and the lean hydrogen flames with unity Lewis number (open symbols).

dependence on the integral length scale. The profiles show strong agreement until the peak, where the peak value shows a slight increase with increasing integral length scale. However, the differences are minor in comparison to the increase in flame area with increasing integral length scale. Non-zero source terms beyond the nominal maximum C_{max}^{1D} value correspond to superadiabatic mixtures.

(a) Effect of integral length scale

(b) Effect of Karlovitz number
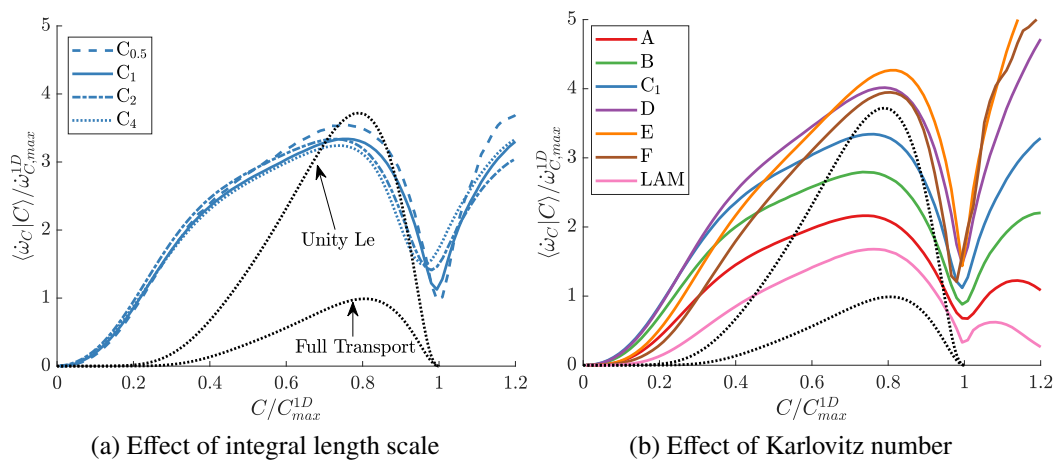
Figure 3.13: Effect of the integral length scale (a) and Karlovitz number (b) on the conditional mean source term profiles. The dotted lines indicate profiles from limiting one-dimensional flames.

Regardless of the Karlovitz number, the shape of the profiles (Fig. 3.13b) is changed significantly, even for the laminar case. Before the peak source terms, the three-dimensional mean profiles exhibit a bump (around $C \approx 0.35$) which is not present for

the one-dimensional profiles. For all cases, the area under the curve is significantly larger than for the one-dimensional profiles. The thermodiffusive instabilities spread the burning across a wider range of C values. Although the magnitude of the source terms is different, they share roughly the same shape until case D. After case D, the profiles start to resemble the unity Lewis profile more closely. This change in the shape of the source term is consistent with the decrease in the burning efficiency of Fig. 3.11. The change of the mean flame structure conditioned on different progress variables has also been noted by other researchers [34, 20].

To quantify this evolution, Fig. 3.14 shows the evolution of the peak source term and its location versus Karlovitz number. The magnitude is found to increase until case D, where it reaches a steady value, slightly above that of the unity Lewis number flamelet. Similarly, the location of the peak source term shifts to reach the value of the one-dimensional unity Lewis number flame. This asymptoting to the unity Lewis number values at high Karlovitz numbers is the result of the gradual disappearance of differential diffusion effects and was also observed in hydrocarbon flames [31].

(a) Maximum value

(b) Location of maximum
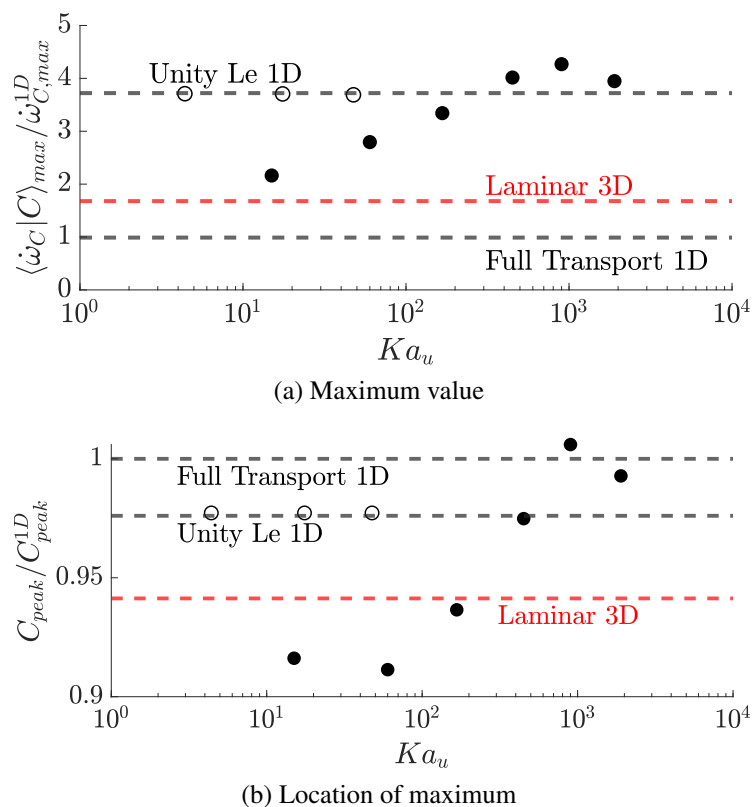
Figure 3.14: Peak normalized conditional mean progress variable source term (a) and its location in progress variable space (b).

3.5.2 Flame curvature

The curvature is calculated as the divergence of the normal vector:

$$\kappa = -\nabla \cdot \mathbf{n} = \nabla \cdot \frac{\nabla C}{|\nabla C|} \tag{3.25}$$

where the curvature is positive when the center of curvature is located in the burnt mixture. Similar to Day et al. [108], the curvature is calculated everywhere in the domain, and then sampled at an isosurface of interest, in this case, C_{peak}.

(a) Effect of Karlovitz number   (b) Effect of integral length scale ratio
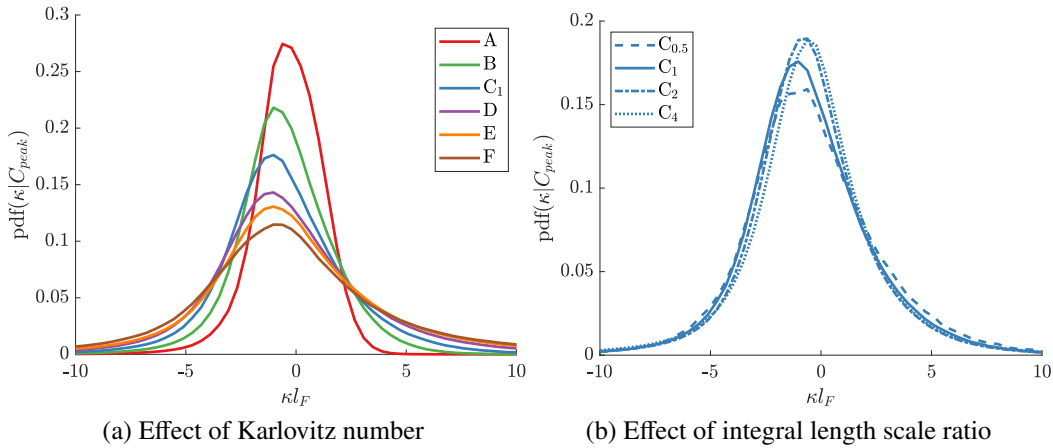
Figure 3.15: Probability density function of the normalized curvature, sampled at C_{peak}.

The probability density function of the curvature, normalized by l_F, and sampled at C_{peak} is shown in Fig. 3.15. Overall, the profiles are skewed slightly towards negative curvature, which is consistent with Lapointe and Blanquart [43]. As the Karlovitz number is increased, the peak drops by more than a factor of 2, and the variance is increased. The turbulence introduces fluctuations at smaller scales, which in turn increases the curvature. In contrast, the effect of the integral length scale (shown in Fig. 3.15b) is much less severe. The distribution narrows slightly with a higher peak value as the integral length scale is increased. This observation reflects the negligible impact of the integral length scale/domain size on the geometry of the flame front (at a fixed Karlovitz number).

The spread of the curvature probability density function is measured by the standard deviation, σ_κ, which is shown in Fig. 3.16. The laminar reaction zone thickness, δ, is defined as the distance over which the fuel consumption rate exceeds 5% of its maximum value. The trends are similar to those observed by Lapointe and Blanquart [43], although the magnitudes are systematically higher, indicating

relatively smaller radii of curvature compared to hydrocarbon flames at the same reaction zone Karlovitz numbers. The standard deviation appears to scale with a quantity which lies between the reaction zone thickness and the Kolmogorov length scale.
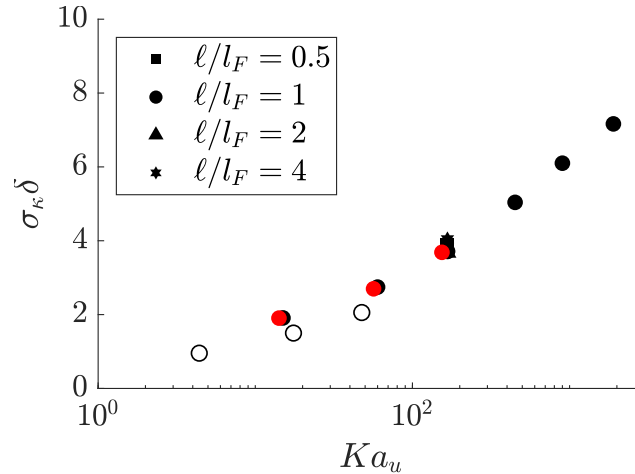
(a) Normalized by reaction zone thickness
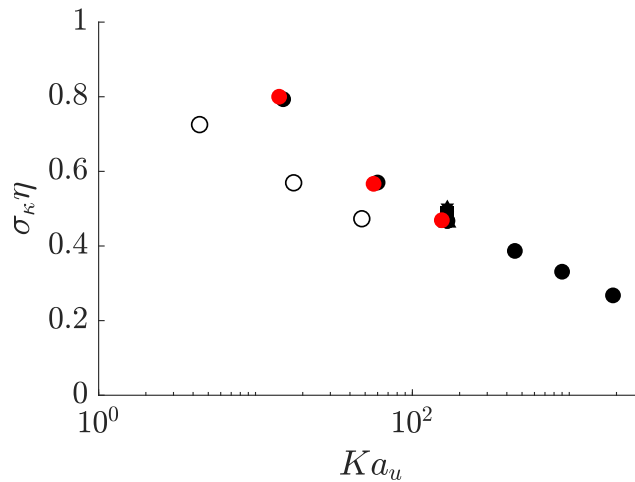
(b) Normalized by Kolmogorov length scale

Figure 3.16: Standard deviation of the curvature probability density function at C_{peak}, normalized by the reaction zone thickness (a) and Kolmogorov length scale (b). Black symbols represent full transport cases, red symbols represent no Soret cases, and open symbols represent unity Lewis cases.

3.5.3 Propagating surface vs. material surface

To provide insight into the evolution of the flame front, we follow the analysis of Yeung et al. [111] which considers a flame front as an infinitely thin propagating surface with an intrinsic propagation speed. As turbulence is introduced, a competition arises between self-propagation and flow-induced motion. Initially, the flame

front behaves as a propagating surface and can respond to the turbulence-induced curvature. However, once turbulence is increased beyond a certain point, the flame acts as a material surface, convected by the flow and unable to control its shape. At this point, the geometry of the flame front is independent of flame quantities and scales purely with turbulence quantities. For stable flames, the transition between propagating and material surfaces is characterized by the ratio of the propagating velocity, S_L^0, and the Kolmogorov velocity scale, u_η. This was discussed in detail by Savard and Blanquart [30], who found that reaction zones under intense turbulence fields behave as material surfaces for n-heptane/air flames.
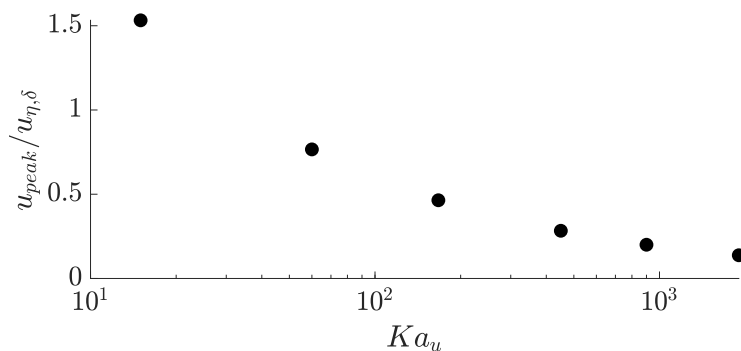
Figure 3.17: Ratio of $u_{peak}/u_{\eta,\delta}$ for the flames in this paper, illustrating the transition between propagating versus material surface behaviour.

The extension to highly turbulent, unstable, lean hydrogen/air flames requires more discussion. First, there is no unique propagation speed as the thermodiffusive instabilities cause any laminar flames to have a local propagation speed varying from close to zero (local extinction) up to several times S_L (for LAM case) [112]. Second, as the Karlovitz number increases, the flame may not be assumed to be infinitely thin. For these reasons and since we are interested in the propagation of a surface located at the reaction zone, we choose u_{peak}, the gas velocity at the peak source term from the one-dimensional laminar flame. The Kolmogorov velocity, $u_{\eta,\delta} = \left(v_{peak}\varepsilon_0\right)^{1/4}$, is calculated using the viscosity at the peak source term from the one-dimensional laminar flame.

The ratio is shown in Fig. 3.17. The ratio for case A is higher than one, indicating that the flame is expected to behave as a propagating surface. In this case, the intrinsic instability of the flame is expected to have a large contribution to the flame geometry. As the Karlovitz number is pushed higher, the ratio drops to be much less than one, indicating that turbulence is expected to have the dominant effect on the flame geometry.

The effect of laminar instabilities on the propagation of turbulent flame fronts was presented in the analytical study of Chaudhuri et al. [107] and confirmed experimentally for thermodiffusively unstable flames by Liu et al. [106]. One of the key metrics of interest is the ratio u'/S_L. When this ratio is greater than one, it indicates that turbulence fluctuations are larger than the natural propagation speed, and turbulence effects are expected to have a stronger effect compared to laminar effects. In the wrinkled flamelet regime, the propagation is dictated by cellular instabilities, and in the thickened flamelet regime, the propagation is dictated by turbulence. The flames in this paper (see Tables 3.2 and 3.3) are within the region where turbulence effects are expected to dominate over laminar effects, and this agrees with the results of Fig. 3.17.

3.5.4 Chemical source term

The two-dimensional mean source terms conditioned on C and κ are shown in Fig. 3.18. As the Karlovitz number is increased, the mean source term is spread over a larger range of κ values. The effect of curvature on the source term appears to be diminishing with increasing Ka_u. To quantify this effect, Fig. 3.19 shows the mean source term conditioned on κ at C_{peak}. As the Karlovitz number is increased, the source term profile becomes flatter. Critically, the profiles asymptote towards the dashed line, which represents the peak source term from a one-dimensional unity Lewis flame normalized by that of the full transport flame. These figures show clearly that the effect of curvature is becoming less pronounced, which is consistent with the observation that differential diffusion effects are being dampened by the turbulence. In the limit of infinite Karlovitz number, it is expected that the effective Lewis number is unity [19], and the source term would become fully independent of curvature [75].

3.6 A priori assessment of Z-C tabulation

In Section 2.2, one of the proposed methods for chemistry tabulation was a two-equation model based on the progress variable, C, and a mixture fraction-like variable, Z. In this section, we study the conditional statistics of local flame geometry and chemistry effects. The validity of the two-equation parameterization of the flame is discussed for the wide range of Karlovitz numbers in the present simulation database. The analysis is important in addressing the LES modelling in Chapter 5.
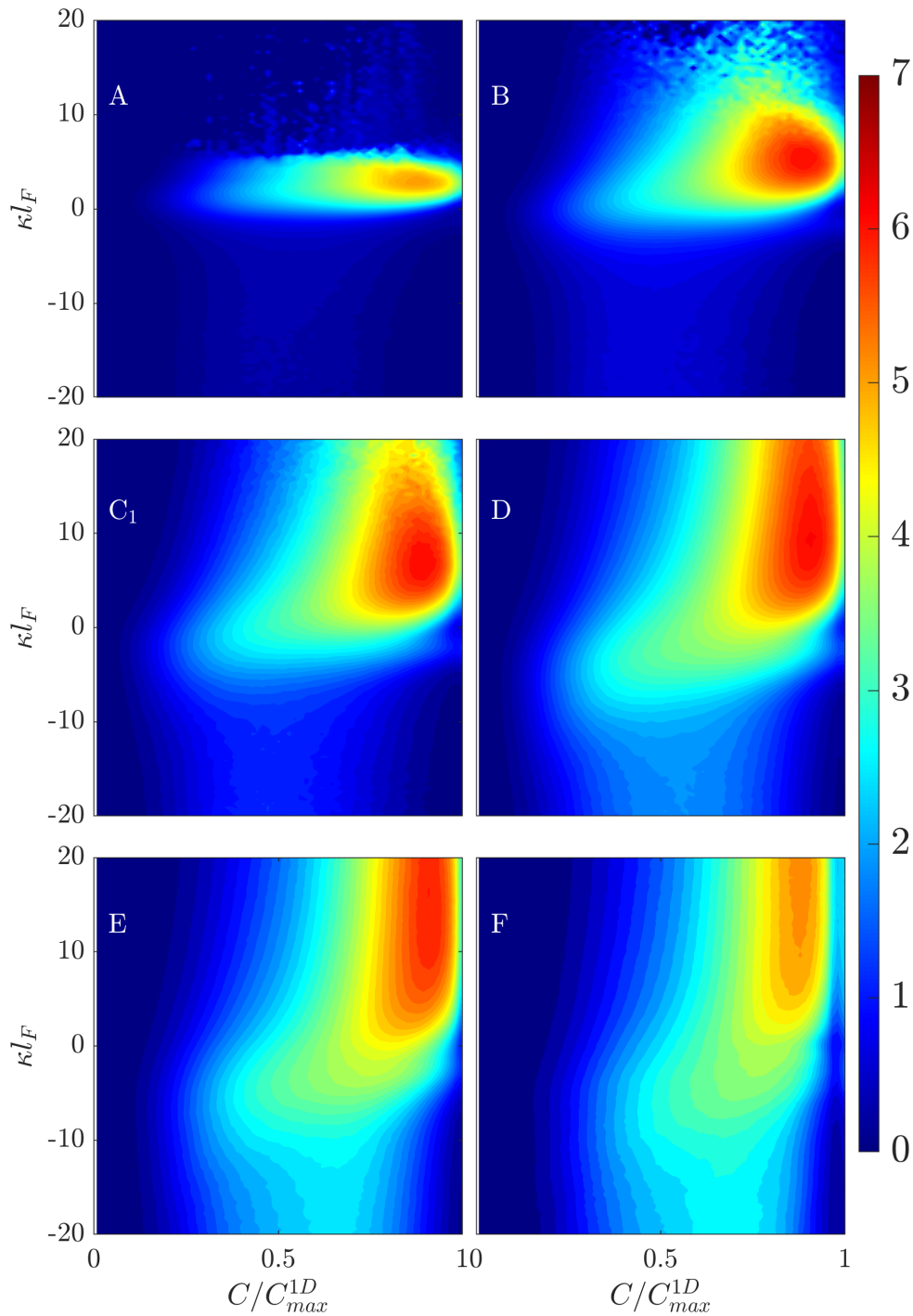
Figure 3.18: Normalized two-dimensional mean source term $\langle \dot{\omega}_C | C, \kappa \rangle / \dot{\omega}_{C,max}^{1D}$.

3.6.1 Local equivalence ratio fluctuations

Differential diffusion causes local focusing and defocusing of the species diffusion flux, resulting in fluctuations of the local equivalence ratio. These fluctuations can be characterized by the mixture fraction, which is defined for a one-step irreversible
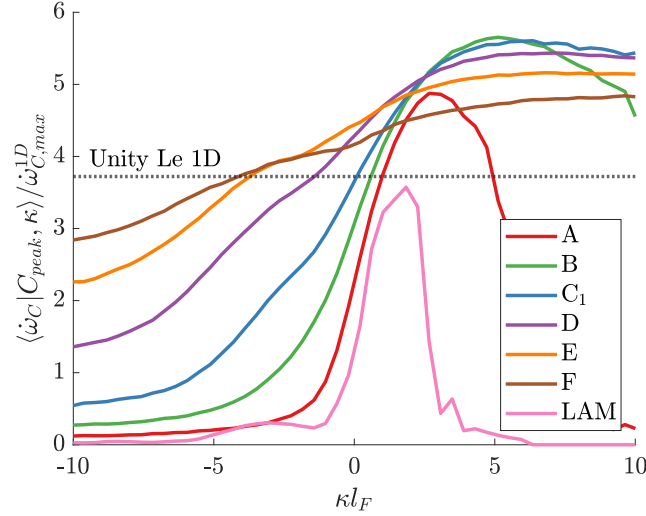
Figure 3.19: Mean source term conditioned on C_{peak} and κ. The dotted line represents $\dot{\omega}_{C,peak}^{1D,Le}/\dot{\omega}_{C,peak}^{1D}$.

chemical reaction as [58]:

$$Z_{mix} = \frac{\nu Y_F - Y_O + Y_{O,2}}{\nu Y_{F,1} + Y_{O,2}} \tag{3.26}$$

where ν is the mass stoichiometric ratio, $Y_{O,2}$ is the oxidizer mass fraction in air, and $Y_{F,1}$ is the fuel mass fraction of the fuel stream. In this work, $Y_{O,2} = 0.232$, $Y_{F,1} = 1$, and $\nu = 8$. Y_O and Y_F represent the local oxidizer and fuel mass fractions.

The joint probability density functions of Z_{mix} and C for the different Karlovitz number cases at $\ell/l_F = 1$ are shown in Fig. 3.20. The black solid lines represent one-dimensional conditional means, $\langle Z_{mix}|C\rangle$. For reference, the blue dotted lines represent the nominal one-dimensional flamelet ($\phi = 0.4$), and the minimum flamelet representing the lean flammability limit ($\phi = 0.25$). The black dashed line represents the physical limit of Z_{mix} versus C for fully burnt conditions from the conservation of mass. Based on the assumption of one-step chemistry, the following relations can be derived [98, 33]:

$$Y_F = Y_{F,1}Z_{mix} - \frac{C}{\nu + 1} \tag{3.27}$$

$$Y_O = Y_{O,2}\left(1 - Z_{mix}\right) - C\left(\frac{\nu}{\nu + 1}\right) \tag{3.28}$$

For lean flames, $Y_F = 0$ at the maximum value of C. The physical bound is thus determined by $Z_{mix} = C/(\nu + 1)$. In Fig. 3.20, it can be seen that the distribution of Z_{mix} and C show some violation of both the minimum flamelet and fully burnt limits.
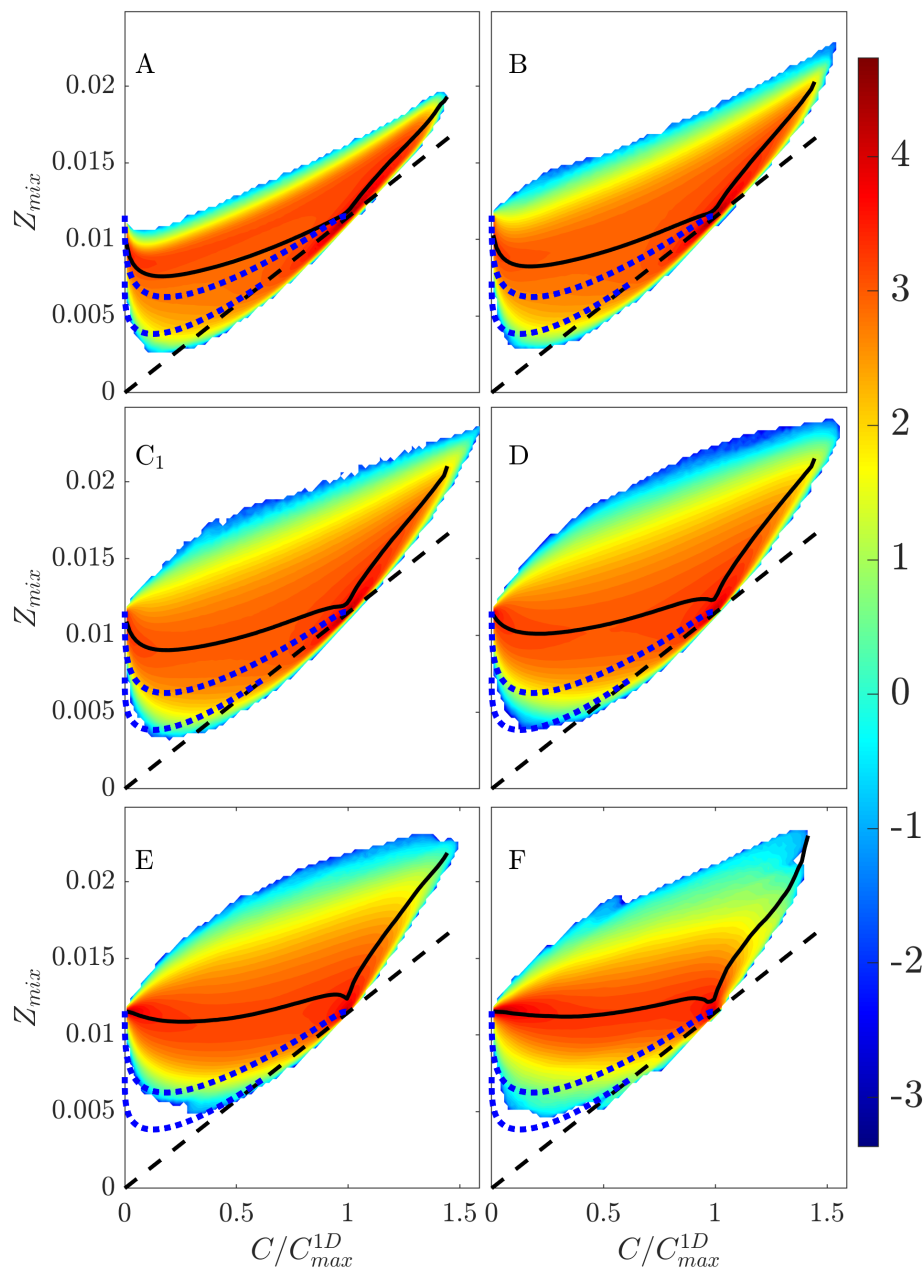
Figure 3.20: Joint probability density function, $\log_{10}\left(\text{pdf}\left(Z_{mix}, C\right)\right)$, of Z_{mix} and C for the different Karlovitz number cases. The black solid lines are mean profiles of Z_{mix} conditioned on the progress variable, $\langle Z_{mix}|C\rangle$, the blue dotted lines represent the nominal and minimum laminar one-dimensional flamelet solutions, and the black dashed line represents the physical bound for equilibrium chemistry.

It is important to note that these limits are theoretical for one-step chemistry. For detailed chemistry, the limits are also verified under thermodynamic equilibrium, for example, one-dimensional laminar flames. However, for thermodiffusively unstable flames, the values can go temporarily beyond the nominal limits. Values of $C > C_{max}^{1D}$

represent superadiabatic burning. The only way for superadiabatic burning to occur is if there is a higher than nominal concentration of fuel. This is reflected in the increase of Z_{mix} past C_{max}^{1D}.

As the Karlovitz number is increased, the jPDF becomes less spread across Z_{mix}, and becomes more uniform across the values of C. The conditional mean profiles, $\langle Z_{mix}|C \rangle$, are also shown in black solid lines, and exhibit similar trends. For case A, the profile of Z_{mix} first decreases to a minimum before increasing to the nominal value at $C = C_{max}^{1D}$. The magnitude of the dip is gradually reduced as the Karlovitz number is increased. For case F, the conditional mean is almost constant with respect to C. These trends clearly outline the diminishing impact of differential diffusion at high Karlovitz numbers.
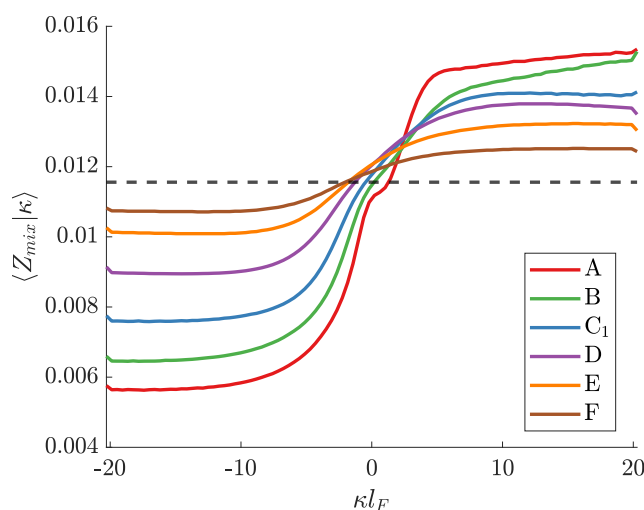
Figure 3.21: Mean of Z_{mix} conditioned on the flame curvature, κ. The dashed line represents the nominal value of Z_{mix} for a $\phi = 0.4$ hydrogen flame.

Because the local differential diffusion effects are strongly related to the flame geometry, it is also of interest to quantify the effect of flame curvature. Figure 3.21 shows the mean of Z_{mix} conditioned on κ. In regions of negative curvature, the burning is inhibited; this is characterized by values of Z_{mix} which are lower than nominal, indicating leaner fuel mixtures. In regions of positive curvature, the burning is enhanced due to the diffusion focusing effect; in these cases, the value of Z_{mix} is higher than nominal, indicating richer fuel mixtures. The effect is more pronounced at lower Karlovitz numbers, with case A exhibiting the largest deviation from nominal. The discrepancy is larger for negative curvatures than for positive curvatures. This could be related to the fact that high negative curvatures have more prominent consequences, as the flame can be extinguished in these regions. As the

Karlovitz number is increased, the differences decrease in magnitude. The results clearly show that differential diffusion effects become increasing less impactful as the Karlovitz number is increased.

3.6.2   Chemical source term

As discussed previously, the local equivalence ratio fluctuations, represented by Z_{mix}, are closely related to the flame curvature (see Fig. 3.21). To investigate the effect of Z_{mix} on the source term, the two-dimensional conditional mean source term, $\langle \dot{\omega}_C | C, Z_{mix} \rangle$, is plotted in Fig. 3.22. The source term has a strong dependence on Z_{mix}, which is the basis for the development of two-equation tabulated chemistry models [58, 33]. This dependence has also been outlined by Berger et al. [28] for a slot burner. Although the dependence of the source term on Z_{mix} is clear, its shape and magnitude qualitatively appear consistent as function of Karlovitz number. The exception is in unrealized conditions. For example, because case A has smaller curvatures (see Figs. 3.15 and 3.18), it does not reach the same magnitude of Z_{mix} compared to the higher Karlovitz numbers, and as such, the source term is zero in these regions. This observation is in contrast to the dependence of the source term on the flame curvature (see Fig. 3.18), which exhibits a change in magnitude and shape as the Karlovitz number is increased.

For further comparison, Figs. 3.23 and 3.24 show one-dimensional cuts of the two-dimension mean at given values of C and Z_{mix}, respectively. At intermediate and large values of the progress variable, the conditional means collapse as a function of Z_{mix} regardless of the Karlovitz number (Fig. 3.23c and d). Similarly, for intermediate and large values of Z_{mix}, the conditional means collapse as a function of C for all Karlovitz numbers (Fig. 3.24c and d). These two observations confirm the validity of a two-equation Z-C tabulation. Difference are observed in the preheat zone (i.e., at small values of C, Fig. 3.23a) and close to the lean flammability limit (i.e., at small values of Z_{mix}, Fig. 3.24a). In these regions, the source term is almost an order of magnitude smaller. At the peaks, the spread of the profiles are of the same absolute magnitude as for other regions. However, because the magnitude of the source term is small, the spread is relatively larger. Their impact on the flame dynamics is expected to be minimal.

3.7   Conclusions

A series of DNS of lean premixed hydrogen/air flames was conducted across a range of Karlovitz numbers and integral length scale ratios. The results have been used
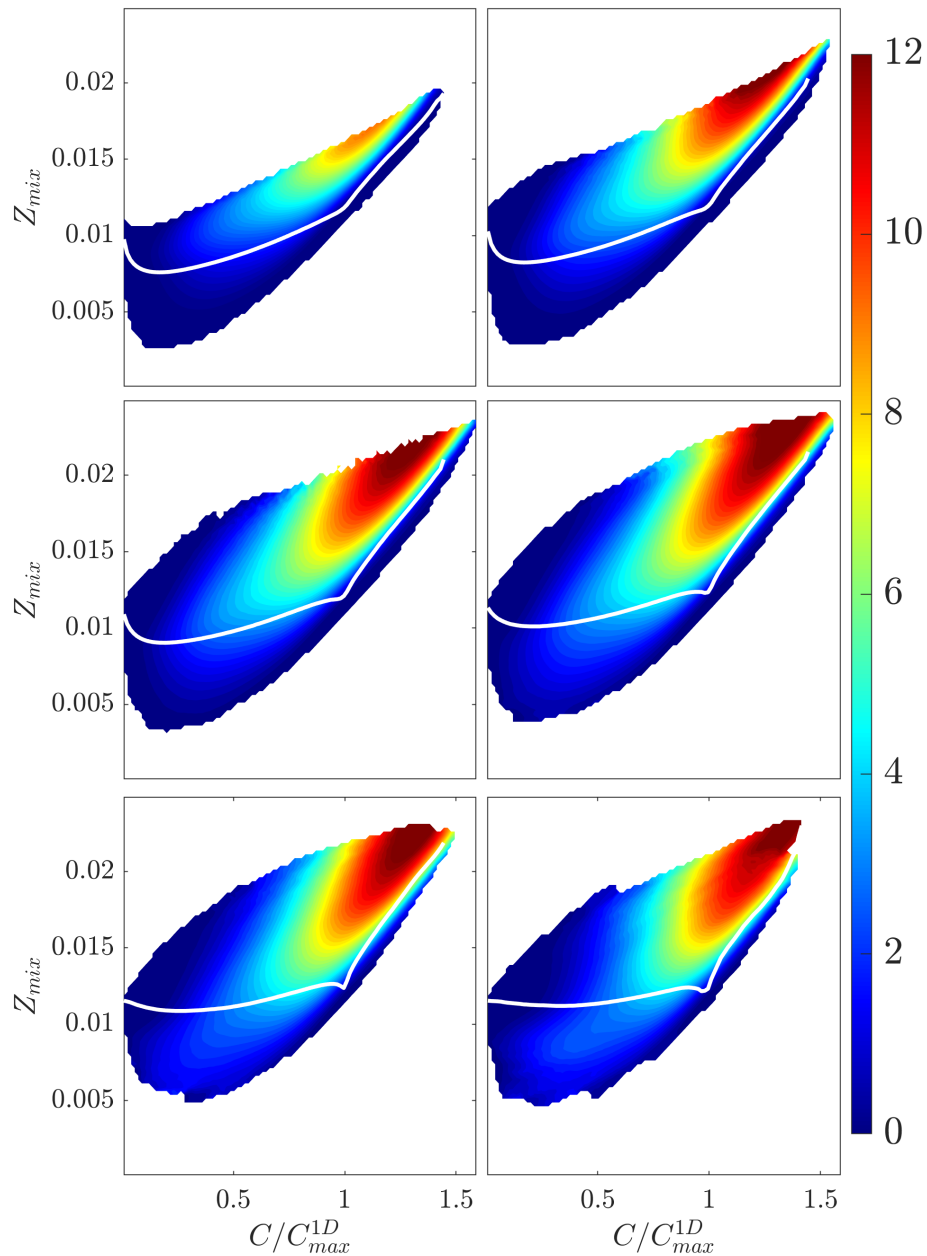
Figure 3.22: Normalized two-dimensional mean source term $\langle\dot{\omega}_C|Z_{mix},C\rangle/\dot{\omega}_{C,max}^{1D}$.

to isolate the controlling parameters in the turbulent flame speed enhancement via Eq. (1.6). A new general expression for the burning efficiency is proposed, which is based on the conditional mean source term, gradient of the progress variable, and the percentage of superadiabatic burning.

At a given Karlovitz number, the ratio of flame isosurface areas to the cross section area, $A(C)/A$, increases linearly with the integral length scale ratio until $\ell/l_F = 2$, and slightly deviates from the trend at $\ell/l_F = 4$. However, the chemical source term

(a) $C/C_{max}^{1D} = 0.2$

(b) $C/C_{max}^{1D} = 0.5$

(c) $C/C_{max}^{1D} = C_{peak}/C_{max}^{1D}$

(d) $C/C_{max}^{1D} = 1$
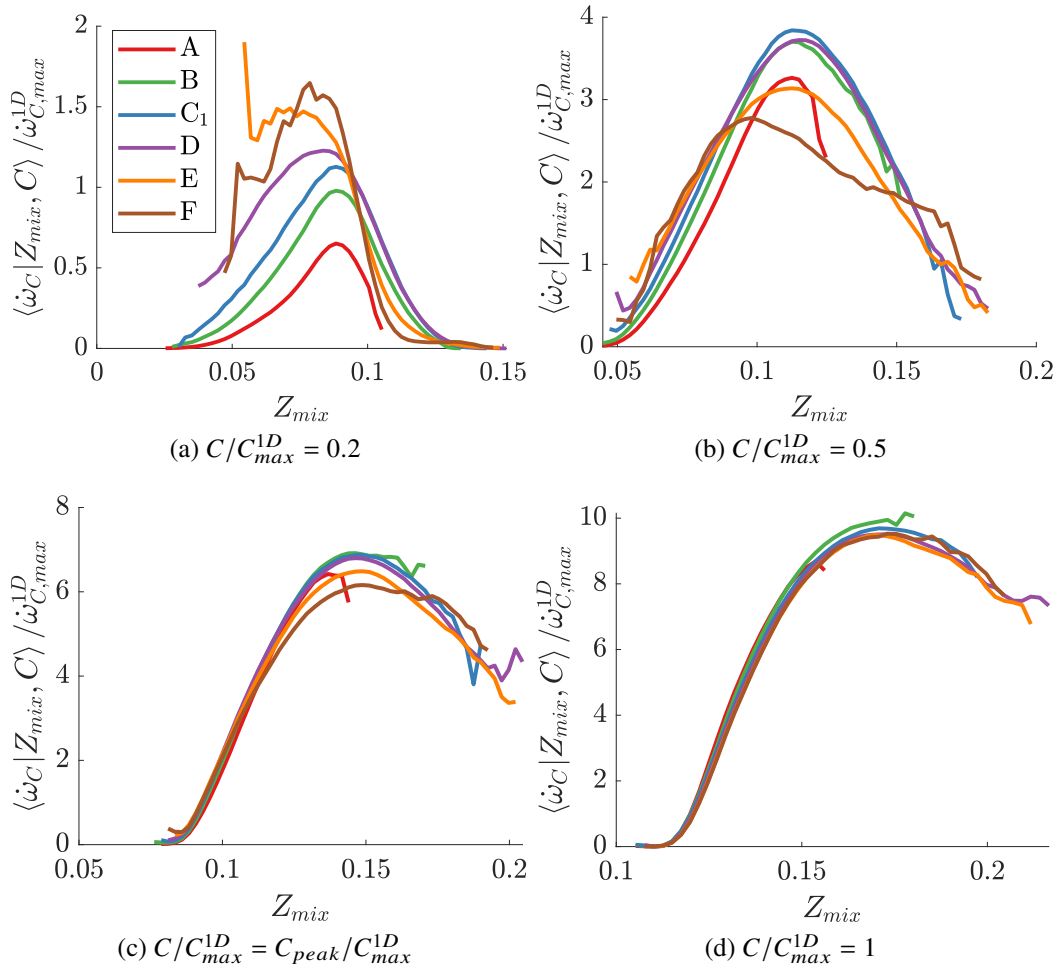
Figure 3.23: Profiles of the two-dimensional condition mean, $\langle \dot{\omega}_C | Z_{mix}, C \rangle$ at given values of C.

conditioned on the progress variable does not show significant differences. As such, the flame speed enhancement can be fully attributed to an increase in the flame area.

At a given integral length scale ratio, ℓ/l_F, the turbulent flame speed, flame area, and burning efficiency all increase with the Karlovitz number before decreasing. These can be explained by the gradual disappearance of differential diffusion effects. As the Karlovitz number is increased, the shape of the mean chemical source term approaches that of the one-dimensional unity Lewis number flame, indicating that the relative importance of differential diffusion effects is lower. Consequently, the thermodiffusive instabilities are also dampened, causing a reduction in the flame area. The flames are shown to behave as a material surface, indicating that turbulence controls the flame front propagation, and not large-scale laminar instability structures. At the small scales, the curvature of the flame front scales
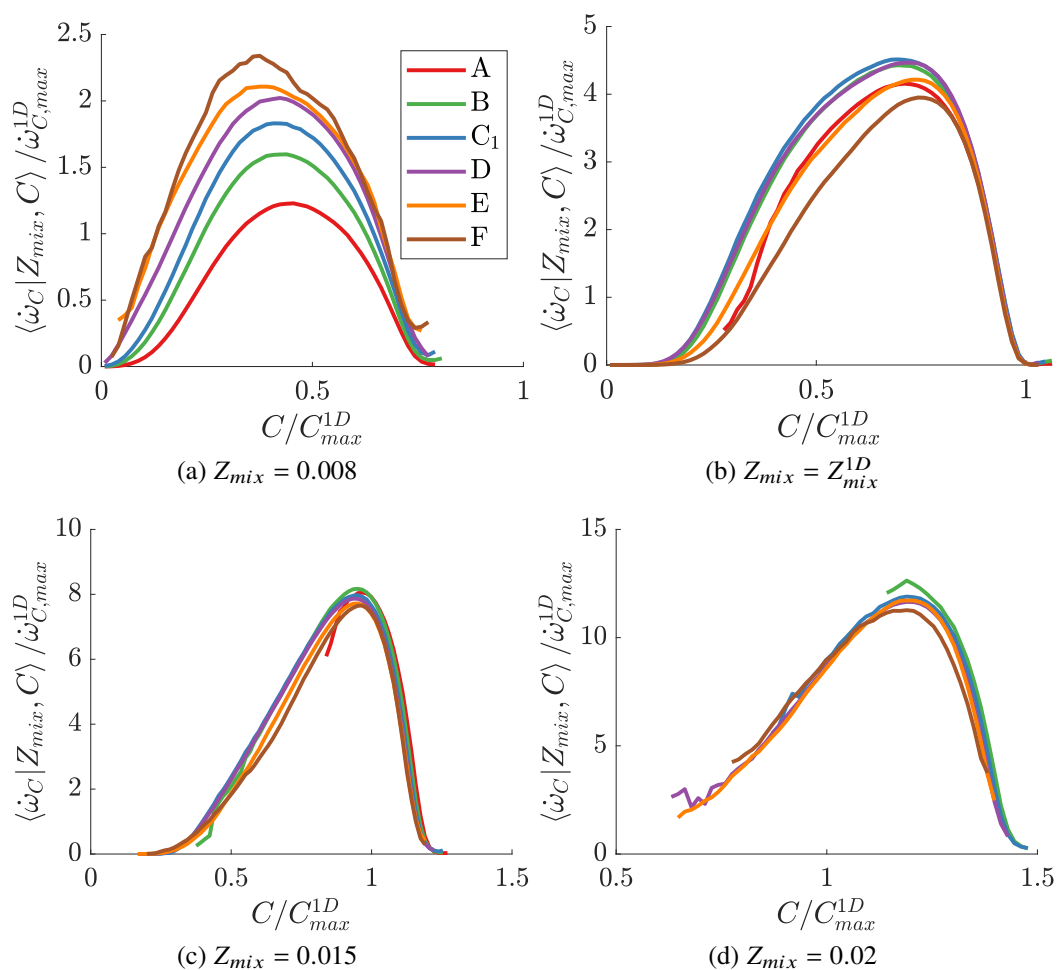
Figure 3.24: Profiles of the two-dimensional condition mean, $\langle \dot{\omega}_C | Z_{mix}, C \rangle$ at given values of Z_{mix}.

with a quantity that lies between the reaction zone thickness and the Kolmogorov length scale.

Although the qualitative observations do not change when Soret effects are neglected, the inclusion of Soret diffusion results in an increase of the mean flame speed by about 35% for case A to 15% for case C. The associated increase in the burning efficiency is approximately 10%.

C h a p t e r   4

IMPACT OF SORET DIFFUSION ON THE EFFECTIVE SPECIES LEWIS NUMBER MODEL IN PREMIXED TURBULENT FLAMES

Savard and Blanquart [19] extracted the effective Lewis numbers from turbulent hydrogen/air flames to predict the flame structure from a DNS dataset. However, the dataset had no Soret diffusion, and was conducted at a small integral length scale. The objective of this chapter is to extend their analysis to include Soret diffusion and integral length scale effects using the DNS data obtained in Chapter 3.

The chapter is organized as follows. Section 4.1 discusses the mean flame structure and associated modelling framework. Section 4.2 extracts the effective Lewis numbers and compares the results to those of Savard and Blanquart [19]. A short discussion of the results is provided in Section 4.3, followed by conclusions in Section 4.4.

4.1   Average flame structure

In this work, we are interested in the flame structure, defined as the average species profiles versus temperature. Results from the DNS will be presented, and their relationship to mean equations will be discussed.

4.1.1   Conditional fuel mass fraction profiles

The spatio-temporal mean of the fuel mass fraction conditioned on temperature, $\langle Y_{H_2}|T\rangle$, for each turbulent flame is shown in Fig. 4.1. Two limiting one-dimensional flamelet solutions are shown which bound the current results, one with full mixture-averaged transport including thermodiffusion, and one with unity Lewis numbers and no thermodiffusion. In this work, laminar flamelet solutions are obtained using FlameMaster [17].

Figure 4.1a shows the effect of Karlovitz number on the fuel mass fraction profile. It is important to note that the three-dimensional laminar case (LAM) is offset from the one-dimensional solution, indicating that the three-dimensional thermodiffusive instabilities affect the overall flame structure. As the Karlovitz number is increased (from A to F), the profiles move closer towards the unity Lewis number profile and
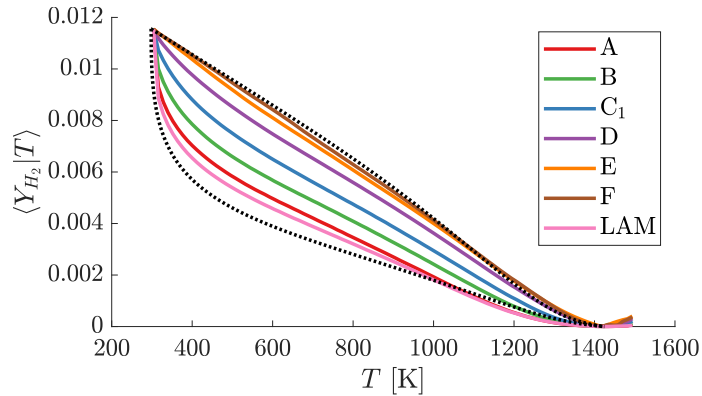
(a) Effect of Karlovitz number
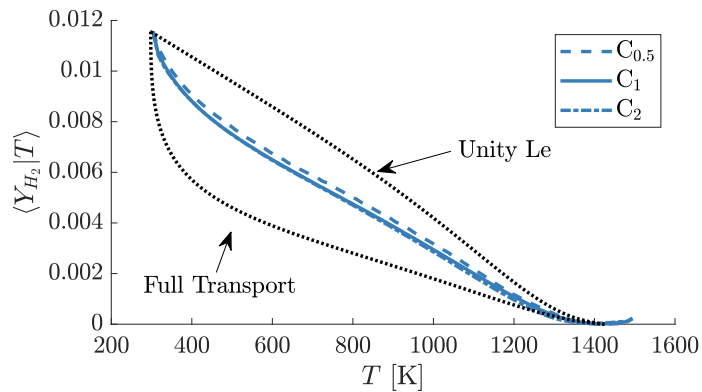
(b) Effect of integral length scale

Figure 4.1: Conditional mean profiles of hydrogen mass fraction against temperature.

become more linear. Turbulent mixing enhances diffusion, leading to a decreased relative importance of molecular diffusion. This transition was quantified for turbulent hydrogen/air flames without Soret effects by Savard and Blanquart [19], and the phenomenon has been reported subsequently by other authors [20].

Figure 4.1b shows the effect of integral length scale on the fuel mass fraction profile for a given Karlovitz number. Cases C_1 and C_2 are overlapping and almost indistinguishable. Case $C_{0.5}$ lies slightly closer to the unity Lewis number solution, although the difference is minor. These results indicate that turbulent fluctuations smaller than the flame thickness have a more significant impact in disrupting the flame structure than turbulent eddies larger than the flame thickness.

4.1.2 Mean equations

The flame structure is controlled by the temperature and species equations, Eqs. (2.3) and (2.4). To facilitate the analysis, it is desirable to reduce these equations to their

main controlling parameters.

The species diffusive flux, originally expressed in terms of the mole fraction, X_i, may be rewritten as:

$$\mathbf{j}_i = -\rho D_i \nabla Y_i - \rho D_i Y_i \frac{\nabla W}{W} - D_i^T \frac{\nabla T}{T} + \rho Y_i \mathbf{u}_c \tag{4.1}$$

Savard and Blanquart [19] conducted a budget analysis of the species transport equation using a one-dimensional laminar flame. The terms corresponding to the gradient of the molecular weight and correction velocity were found to be negligible in comparison to the other terms, and will thus be dropped in the present analysis. Although they did not account for Soret diffusion, other researchers have shown that the diffusive flux due to temperature gradients is significant, particularly for light species such as H and H_2 [44]. Savard and Blanquart [19] also conducted a budget analysis of the temperature equation. They showed that the dominating terms were the advection, diffusion, and source term of temperature.

To analyze and quantify the effect of turbulence on the mean flame structure, we consider the Reynolds-averaged Navier-Stokes (RANS) equations. Following the simplifications introduced above, the Reynolds-averaged temperature and species transport equations are written as:

$$\frac{\partial \overline{\rho}\widetilde{T}}{\partial t} + \nabla \cdot \left(\overline{\rho}\widetilde{\mathbf{u}}\widetilde{T} \right) = \nabla \cdot \left[\overline{\rho} \left(\alpha + \alpha_t \right) \nabla \widetilde{T} \right] + \overline{\dot{\omega}}_T \tag{4.2}$$

$$\frac{\partial \overline{\rho}\widetilde{Y}_i}{\partial t} + \nabla \cdot \left(\overline{\rho}\widetilde{\mathbf{u}}\widetilde{Y}_i \right) = \nabla \cdot \left[\overline{\rho} \left(D_i + \alpha_t \right) \nabla \widetilde{Y}_i + \overline{\rho} D_i^T \nabla \widetilde{T} \right] + \overline{\dot{\omega}}_i \tag{4.3}$$

where the overline and tilde denote Reynolds and Favre averages respectively, and α_t is the turbulent diffusivity. The contributions of the unresolved turbulent fluctuations are modelled through the use of turbulent mass and thermal diffusivities. Consistent with the observation from Fig. 4.2, the turbulent diffusivity for species and temperature are assumed to be equal, implying a unity turbulent Lewis number.

From Eqs. (4.2) and (4.3), effective Lewis numbers can be identified for each species as:

$$\mathrm{Le}_{i,\mathrm{eff}} = \frac{\alpha + \alpha_t}{D_i + \alpha_t} = \frac{1 + \psi}{1/\mathrm{Le}_i + \psi} \tag{4.4}$$

where $\psi = \alpha_t/\alpha$. Note that the turbulent diffusivity is assumed to enhance the thermal and mass diffusivity equally, implying a unity turbulent Schmidt number. In the limit of infinite α_t, the effective Lewis numbers tend to unity, such that

there are no more differential diffusion effects. This model was proposed first by Peters [98] and validated later by Savard and Blanquart [19]. However, in their work, neither considered the impact of Soret diffusion.

4.2 Effective Lewis numbers

In this section, we present a detailed discussion on the derivation and extraction of the effective Lewis numbers.

4.2.1 Preliminary observations

Savard et al. [113] pointed out that the structure of a one-dimensional laminar premixed flame of n-heptane/air does not change when all species and thermal diffusivities are changed by the same factor. To show this remains true even in the case of hydrogen/air flames where there is significant preferential diffusion, Fig. 4.2a shows the H_2 mass fraction profile as a function of temperature from one-dimensional flamelet solutions. The magnitudes of all D_i and α were multiplied by a factor of 0.1 and 10, effectively maintaining the same species Lewis numbers. The thermodiffusion coefficients, D_i^T, were also adjusted accordingly to maintain the same relative effect.

The corresponding laminar flame speeds, $S_L = 6.46, 19.8, 64.6$ cm/s, are altered by a factor of $\left(D_i/D_{i,0}\right)^{0.5}$, consistent with theoretical scalings [113]. However, there is no distinguishable change in the flame structure. This indicates that the magnitude of the diffusivities does not control the flame structure. Changes to the flame structure must be attributed to varying Lewis numbers.

Finally, it should be noted that both species and thermodiffusion coefficients vary through the flame, and as such, their ratios (i.e., the Lewis numbers) may not be constant. Figure 4.2b shows the flame structures obtained with mixture-averaged transport and Soret, constant Lewis number and Soret, and mixture-averaged without Soret. The results highlight the importance of including Soret diffusion as it lowers the fuel mass fraction profile in the preheat zone. In contrast, the results show that using constant Lewis numbers for each species is sufficient to reproduce the flame structure [114].

4.2.2 Effective Soret diffusion

Quantifying the reduction of thermodiffusion as turbulent mixing increases requires more attention. The temperature equation, Eq. (4.2), recovers the same functional form as the one-dimensional laminar flame when the spatial coordinate and velocity
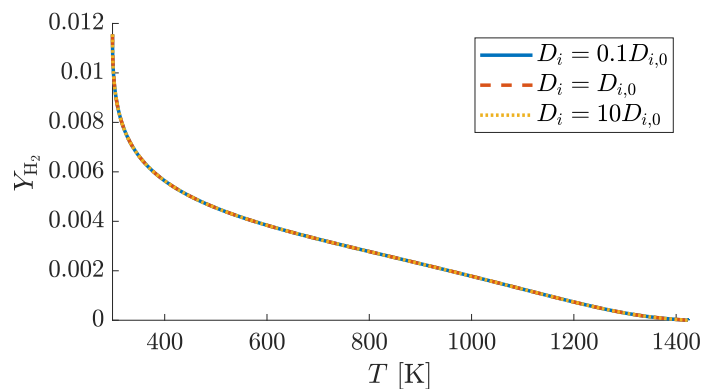
(a) Effect of diffusivity magnitude
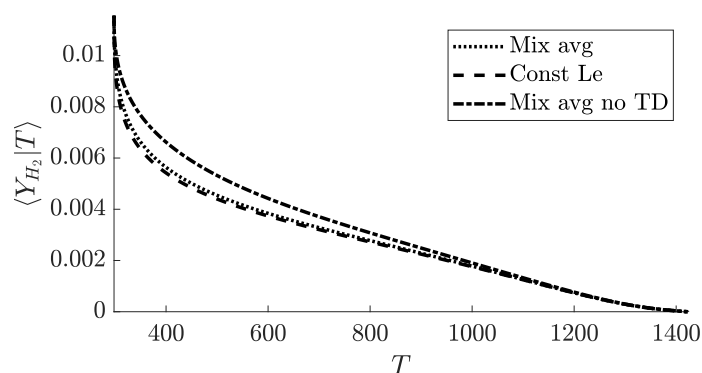
(b) Effect of Soret diffusion

Figure 4.2: H_2 mass fraction profiles from one-dimensional flat flames.

are both rescaled by $\sqrt{1 + \psi}$. In other words, the thermal diffusivity in Eq. (4.2) becomes α. Performing the same rescaling in the species equations, Eq. (4.3), the molecular diffusion coefficient becomes $\alpha/\mathrm{Le}_{i,\mathrm{eff}}$ and the thermodiffusion coefficient becomes $D_i^T/(1 + \psi)$. Practically, the original Lewis numbers are replaced by their effective values, and the thermodiffusion coefficients are reduced by $(1 + \psi)$.

4.2.3 Extraction of the effective Lewis numbers

The identification of the effective Lewis numbers follows the procedure outlined by Savard and Blanquart [19] with one important difference: the effective Lewis numbers of all species are modified according to Eq. (4.4). The Soret diffusion coefficients are proportionally scaled down by a factor of $1/(1 + \psi)$. The mass fraction profiles from the DNS and flamelet solutions are both interpolated onto the same uniform grid in temperature space for comparison. The L_2-norm of the error between the conditional mean of H_2 from the DNS and the laminar flamelet is minimized. The vector $\mathbf{Le_{eff}}$ containing all species effective Lewis numbers is

identified according to:

$$\textbf{Le}_{\textbf{eff}} = \underset{\textbf{Le}^*}{\text{argmin}}\frac{1}{N}\sum_{n=1}^{N}\left(Y_{\text{H}_2}\left(\textbf{Le}^*, T_n\right) - Y_{\text{H}_2}^{DNS}\left(T_n\right)\right)^2 \tag{4.5}$$

where $\textbf{Le}^*$ is obtained from Eq. (4.4), and N is the number of points.

In their work, Savard and Blanquart [19] indicated that in the limit of no turbulence, the effective Lewis numbers should asymptote to the one-dimensional laminar Lewis numbers. However, case LAM is the true limiting case of no turbulence. As such, the Lewis numbers used in Eq. (4.4) should be those of case LAM. As mentioned previously, the fuel mass fraction profile for case LAM in Fig. 4.1a deviates strongly from the full transport one-dimensional laminar profile due to the presence of thermodiffusive instabilities. In other words, the Lewis numbers necessary to reproduce the average flame structure of case LAM are not those of the one-dimensional flat flame. The effective Lewis numbers for this case are identified first and are provided in Table 4.1, along with the one-dimensional laminar values for reference.

Table 4.1: Species Lewis numbers.

Species	Le_i^{1D}	Le_i^{LAM}
N_2	1.391	1.231
H	0.190	0.260
O_2	1.449	1.260
O	0.734	0.805
OH	0.744	0.813
H_2	0.312	0.405
H_2O	0.833	0.882
HO_2	1.201	1.126
H_2O_2	1.229	1.142

4.2.4   Results

Figure 4.3 shows the effective H_2 mass fraction profiles of flames A and F obtained following the method outlined in Section 4.2 with and without Soret diffusion. Including Soret diffusion is necessary to obtain the correct shape of $\langle Y_{\text{H}_2}|T\rangle$. Since Soret diffusion is driven by a temperature gradient, the amount of H_2 diffusing into the preheat zone is decreased compared to the case with no Soret diffusion calculated at the same effective Lewis number. Consequently, the profile with no Soret diffusion overestimates the fuel mass fraction in that region. This effect is more pronounced for the lower Karlovitz numbers. As the turbulence is increased,

the relative impact of Soret diffusion is reduced. For case A, $\text{Le}_{\text{H}_2,\text{eff}} = 0.47$ and $1/(1 + \psi) = 0.769$. For case F, the Lewis number is increased to $\text{Le}_{\text{H}_2,\text{eff}} = 0.922$ and $1/(1 + \psi) = 0.043$, significantly reducing the effect of Soret diffusion.
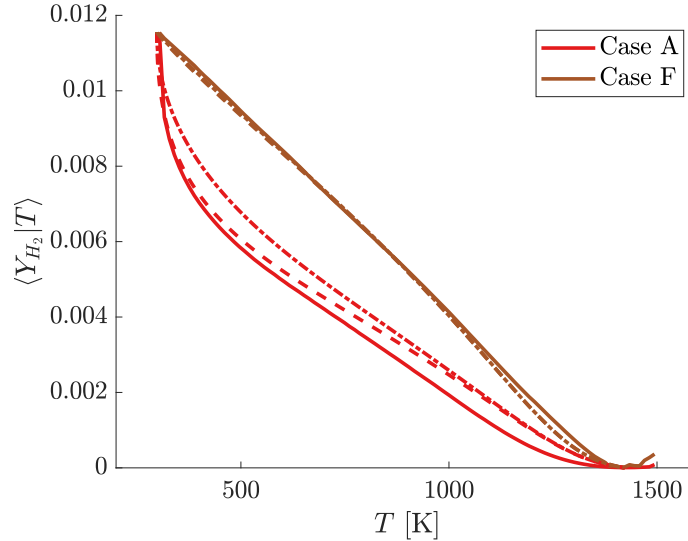
Figure 4.3: Structure of the H_2 mass fraction profiles for cases A and F. Corresponding flamelet solutions with (dashed) and without (dash dot) Soret diffusion are also shown at the same effective Lewis numbers.

The extracted values of $\psi = \alpha_T/\alpha$ are shown in Fig. 4.4. As expected, the magnitude of the turbulent diffusion coefficient increases as the Karlovitz number increases. Savard and Blanquart [19] proposed a Karlovitz number model which takes the form:

$$\text{Le}_{i,\text{eff}}^{\text{Ka}} = \frac{1 + a\,\text{Ka}}{1/\text{Le}_i + a\,\text{Ka}} \tag{4.6}$$

where a is a proportionality coefficient which was adjusted to fit the data. They proposed two alternative exponents on Ka in Eq. (4.6) based on length scale ($\text{Ka}^{2/3}$) or timescale (Ka^2) arguments. From Fig. 4.4 it can be seen that the best agreement is with the exponent of one. However, the 2/3 exponent also shows good agreement, especially at the lower Karlovitz numbers.

The corresponding effective Lewis numbers of H_2 as a function of Karlovitz number are shown in Fig. 4.5. The effective Lewis number increases with Karlovitz number, starting from the LAM value and ultimately plateauing at unity. The integral length scale has virtually no impact on the extracted effective Lewis numbers, lending support for the argument that the turbulent diffusivity is largely controlled by eddies on the order of the flame thickness. Stated differently, only turbulent fluctuations on
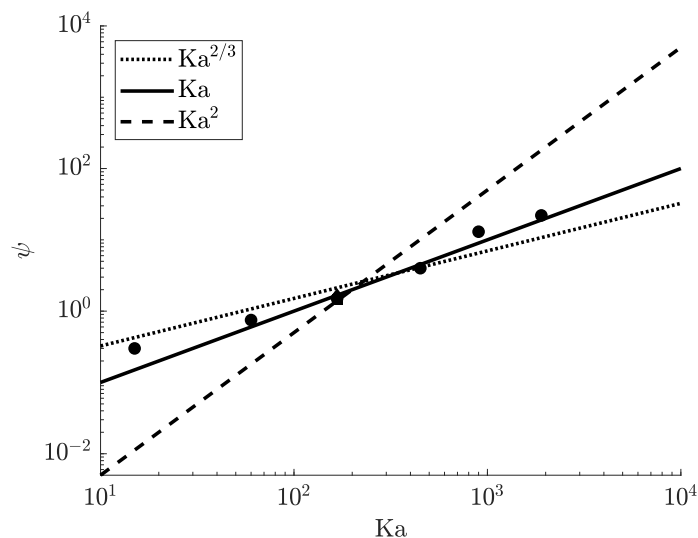
Figure 4.4: Value of ψ versus Karlovitz number obtained from fitting flamelets. Cases $C_{0.5}$ (diamond) and C_2 (square) are also shown.

a length scale smaller than the flame thickness may contribute to altering the overall flame structure.

The data also shows strong agreement with the results of Savard and Blanquart [19], obtained using DNS results of turbulent flames without Soret diffusion. Soret diffusion has been shown to enhance the development of cellular structures due to thermodiffusive effects [26], and result in markedly different mean profiles. However, when properly accounted for, Soret diffusion does not have an impact on the effective Lewis number model.

4.3 Discussion

The effective Lewis numbers have an impact on the effective one-dimensional laminar flame speed and thickness, ranging from $S_L = 0.206$ to 0.410 m/s and $l_F = 0.683$ to 0.375 mm for full transport and unity Lewis number, respectively. Naturally, calculating the Karlovitz number using the nominal values of S_L and l_F leads to overpredicted values compared to using the effective values, as shown in Fig. 4.6. As the Karlovitz number increases, the laminar flame thickness decreases and the laminar flame speed increases, leading to an overall decrease of the effective Karlovitz number experienced by the flame. At the highest tested Karlovitz numbers, the effective Karlovitz number is smaller by a factor of more than three.

Based on a matched asymptotic analysis using one-step chemistry, the fuel Lewis
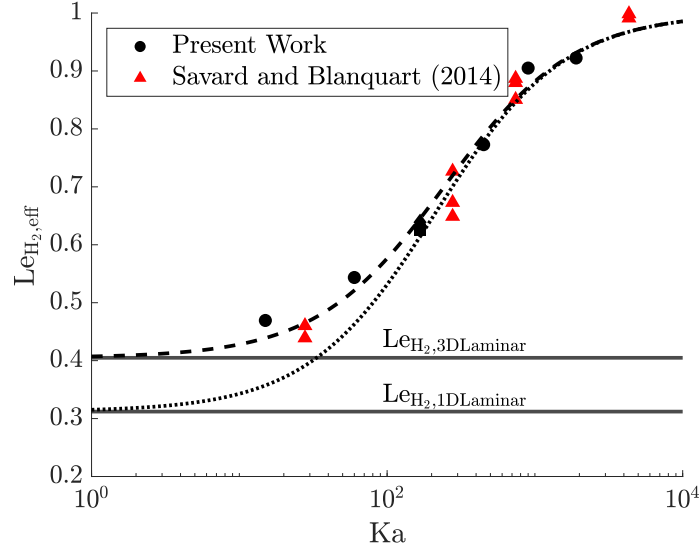
Figure 4.5: Effective Lewis number as a function of Karlovitz number. The model in Eq. (4.6) is shown with dashed ($a = 0.01$) and dotted ($a = 0.015$) lines asymptoting to the laminar one-dimensional or three-dimensional effective Lewis numbers, respectively. Cases $C_{0.5}$ (diamond) and C_2 (square) are also shown.
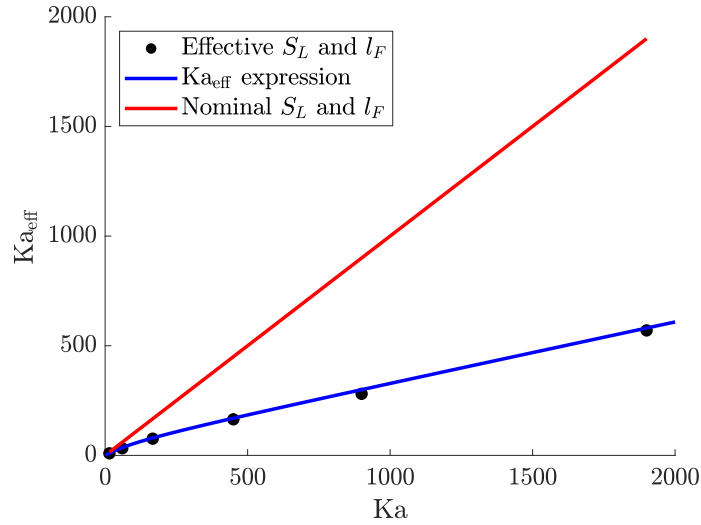
Figure 4.6: Effective Karlovitz number as a function of nominal Karlovitz number.

number dependence is explained as [115]:

$$\frac{S_{L,1}}{S_{L,2}} = \left(\frac{Le_{H_2,2}}{Le_{H_2,1}}\right)^{0.5} \tag{4.7}$$

$$\frac{l_{F,2}}{l_{F,1}} = \left(\frac{Le_{H_2,1}}{Le_{H_2,2}}\right)^{0.5} \tag{4.8}$$

where the subscripts 1 and 2 represent two different sets of diffusion models. Although the relations were derived for one-step chemistry, it has been shown that,

using detailed chemistry, the flame thickness scaling works very well, whereas an exponent of 0.6 is suitable for the flame speed scaling [19]. Using this proposed exponent, the effective Karlovitz number can be approximated as:

$$\text{Ka}_{\text{eff}} = \left(\frac{\text{Le}_{\text{H}_2}^{\text{1D}}}{\text{Le}_{\text{H}_2,\text{eff}}} \right)^{1.1} \text{Ka} \tag{4.9}$$

The effective Karlovitz number using Eq. (4.9) with Eq. (4.4) is compared to the calculated effective Karlovitz numbers in Fig. 4.6. The agreement is very good, indicating good applicability of the model.

It was suggested by Aspden et al. [112] to use the three-dimensional freely propagating flame to determine the Karlovitz number. The current analysis relates the effective Lewis numbers to the freely propagating flame, providing an alternative method of characterizing turbulent hydrogen flames. The Karlovitz number model can easily be used to identify the effective Lewis number, and important parameters such as S_L and l_F can easily be obtained from a laminar flame solver.

4.4 Conclusions

We leveraged a recent database of direct numerical simulations of turbulent lean hydrogen/air premixed flames [116] and performed a detailed analysis of their effective Lewis numbers. This analysis extends previous work by Savard and Blanquart [19] to consider both Soret diffusion and integral length scale effects.

The average flame structure, defined as the mean species mass fraction profiles conditioned on temperature, was shown to be that of a one-dimensional flame with effective Lewis numbers and effective thermodiffusion coefficients. The effective Lewis numbers follow a model first introduced by Peters [115]. Inspired by the species and temperature Reynolds-averaged transport equations, the effective thermodiffusion coefficient was proposed to be the corresponding one-dimensional value scaled down by a factor of $1/(1 + \psi)$. This scaling factor ranges from 0.769 for the lowest Karlovitz number to 0.043 for the highest Karlovitz number. As turbulence enhances the mixing through the added turbulent diffusivity, the relative impact of both molecular and Soret diffusion are reduced.

The extracted effective Lewis numbers of H_2 were compared to those of Savard and Blanquart [19], and showed excellent agreement. However, it was shown that the correct reference species Lewis numbers used in deriving effective Lewis numbers should be those of the three-dimensional laminar case, and not those of the one-

dimensional laminar case. Although Soret diffusion changes the flame structure, it has a negligible impact on the extracted effective Lewis numbers.

Finally, the extracted effective Lewis numbers were found to be independent of the integral length scale. This observation confirms that the turbulent fluctuations most susceptible to alter the flame structure are those of the size of the flame thickness.

Chapter 5

CAPTURING DIFFERENTIAL DIFFUSION EFFECTS IN LARGE EDDY SIMULATION OF TURBULENT PREMIXED FLAMES

[1]   M. X. Yao and G. Blanquart. "Capturing differential diffusion effects in large eddy simulation of turbulent premixed flames". In: *Proceedings of the Combustion Institute* (2024). (Under Review).

The objectives of this chapter are twofold: 1) to apply the two-equation model of Schlup and Blanquart [33] in the framework of LES and 2) to assess its ability to capture burning behaviour that is not captured through traditional methods in the simulation of a low-swirl burner.

The chapter is structured as follows. Section 5.1 outlines the details of the geometry and boundary conditions. The chemical models being used are reviewed in Section 5.2, and the LES filtering of tabulated chemistry is reviewed in Section 5.3. The results of the LES are presented in Section 5.4. The conclusions are drawn in Section 5.5.

5.1   Burner geometry and boundary conditions

We consider the series of experimental measurements performed by Cheng et al. [11] in a low-swirl burner (LSB). A brief overview of the geometry is presented here. For a more detailed description, the reader is referred to [11].

A three-dimensional rendering of the low-swirl injector (LSI) is shown in Fig. 5.1. As can be seen, the LSI is composed of two parts: 1) a central pipe ($R_c = 1.89$ cm) that holds a perforated screen, consisting of 54 holes with a blockage ratio of about 46%, and 2) a co-annular channel ($R_i = 2.86$ cm) composed of 16 vanes with 40° exit blade angles. In the simulations, 42% of the flow passes through the central pipe. After a recess region, the premixed gas mixture of fuel and air is injected into an enclosed axisymmetric combustion chamber with inner radius $R_e = 9$ cm. The combustion chamber has a length of $L = 31$ cm, after which there is a contraction and an exit section.

To simplify the numerical simulations, the computational domain was decomposed into two parts: the swirler and the combustion chamber. The flow through the
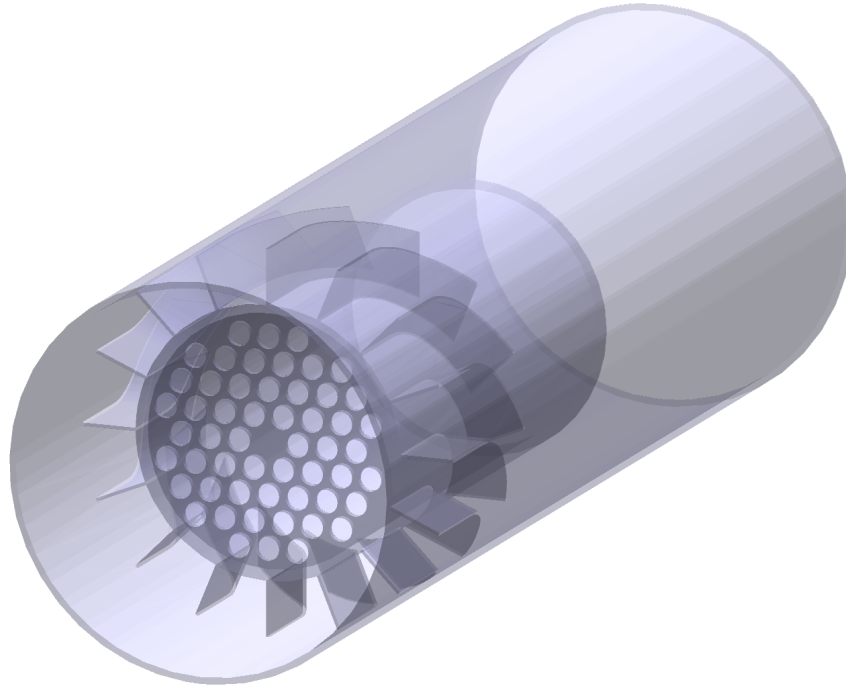
Figure 5.1: Three-dimensional rendering of the low-swirl injector.

swirler was investigated first with non-reacting LES, and the outflow conditions downstream of the injector but upstream of the combustion chamber were recorded as a function of time. Then, these outflow conditions were used as inflow conditions for the reacting LES of the combustion chamber. As a result, the flow through the swirler needs to be computed only once, and simulations of the turbulent flame with different fuels can be performed on a coarser mesh. This first calculation is meant to produce realistic turbulence fluctuations with the correct mean velocities. As the kinematic viscosities between the two unburnt mixtures differs by only 11%, a single inflow profile may be generated without significant impact.

Given the complexity of the LSI, the fine details of the geometry of the injector were represented with the immersed boundaries technique [90]. In particular, we use a velocity reconstruction (or interpolation) approach similar to that proposed by Kang et al. [92]. This approach provides an efficient description of the flow around complex geometries on structured meshes. For an accurate description of the flow field, the geometry of the swirler assembly was represented on a cylindrical mesh of $N_x \times N_r \times N_\theta = 256 \times 120 \times 256$ grid points. Figure 5.2 shows the contour of velocity magnitude through the swirler. The flow through the central perforated screen resembles grid turbulence and decays slowly with downstream distance. The flow through the swirled vanes transitions rapidly from laminar to turbulent as it is

accelerated. The bulk axial velocity through the entire geometry (central pipe and swirled vanes) at the exit plane is $U_0 = 18$ m/s, and the mean azimuthal velocity is 10.2 m/s.
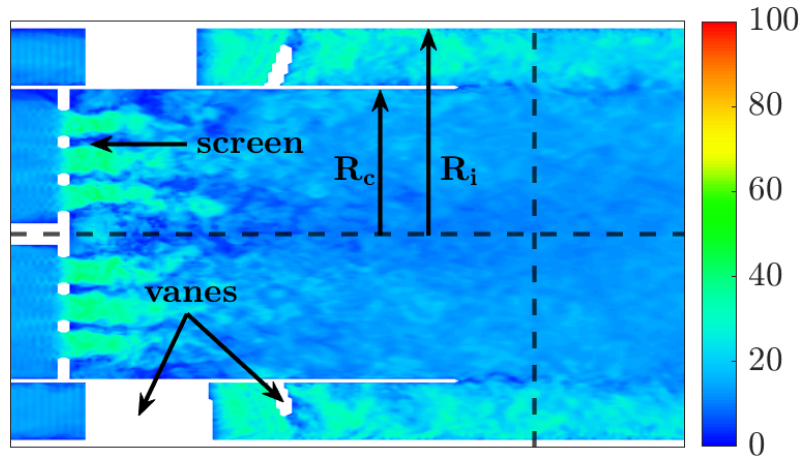
Figure 5.2: Two-dimensional contour of velocity magnitude through the swirler. The empty white regions correspond to cuts through the walls and swirler vanes. The vertical dashed line represents the location where the inflow conditions for the combustion chamber were extracted.

To further characterize the flow field in the LSI, Fig. 5.3 shows the axial, u_x, and azimuthal, u_θ, velocity fields. Behind the perforated screen, the u_x velocity field exhibits small recirculation regions near the annulus pipe and at the centerline. In the figure, the solid vertical lines represent locations at which the velocity magnitude fields, $|\mathbf{u}|$, are plotted in Fig. 5.4. In the center pipe, the flow is seen to develop from the perforated screen into isotropic turbulence. At the outlet plane, the two regions exhibit mixing at the shear layer.

5.2 Chemical model

Two separate fuel/air mixtures are considered. For hydrogen combustion, the 9-species, 54-reaction (forward and backward counted separately) chemical mechanism by Hong et al. [95] was used with updated rate constants [96, 97]. For methane, the GRI 3.0 mechanism [117] was used. The equivalence ratios under consideration are $\phi = 0.4$ for the hydrogen/air flame (laminar flame speed $S_L = 0.206$ m/s and laminar flame thickness $l_F = 6.8 \times 10^{-4}$ m) and $\phi = 0.59$ for methane/air ($S_L = 0.102$ m/s and $l_F = 1.0 \times 10^{-3}$ m).
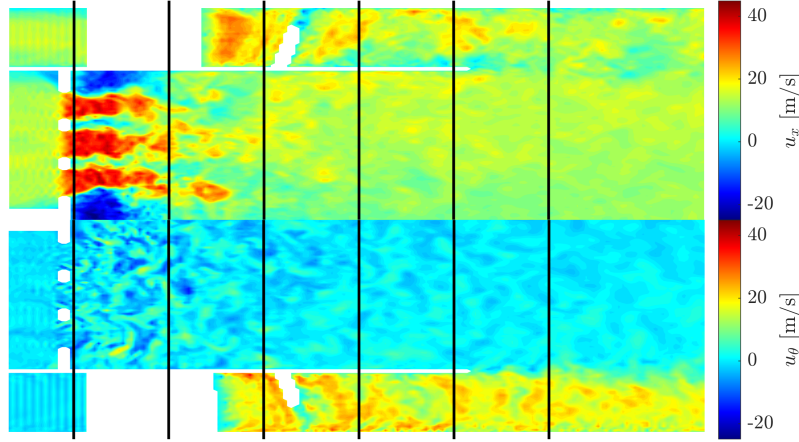
Figure 5.3: Two-dimensional contour of axial velocity (top), u_x, and azimuthal velocity (bottom), u_θ. The black lines represent locations for which the velocity fields are plotted in Fig. 5.4.

5.3 Filtered tabulated chemistry approaches

Two separate tabulation strategies are used in the simulations of the turbulent reacting flow in the combustion chamber. The presentation starts with a discussion of the different subfilter scale models and follows with a discussion of the specific modelling approaches. In this work, the progress variable is defined as the mass fraction of water, $C = Y_{\mathrm{H_2O}}$.

5.3.1 Common modelling strategies

In Eq. (2.27), a model must be provided for the filtered source term, $\overline{\dot{\omega}}_C$. In LES, the filtering over a given volume V can be expressed as

$$
\begin{aligned}
\overline{\dot{\omega}}_C &= \frac{1}{V} \iiint \dot{\omega}_C dV \\
&= \frac{1}{V} \int_n \left(\iint_{A(C)} \dot{\omega}_C dA \right) dn \\
&= \frac{1}{V} \int_C \langle \dot{\omega}_C | C \rangle \frac{A(C)}{|\nabla C|} dC \\
&= \int_C \langle \dot{\omega}_C | C \rangle P(C) dC
\end{aligned}
\tag{5.1}
$$

by splitting the volume integral into an integral over an isosurface of C, $A(C)$, and an integral in the normal direction, n. There are two terms that require closure: the conditional mean source term, $\langle \dot{\omega}_C | C \rangle$, and the subfilter density function, $P(C)$. The first term was first discussed in Chapter 3, and will be revisited in Subsections 5.3.2-5.3.4 in the context of LES modelling.
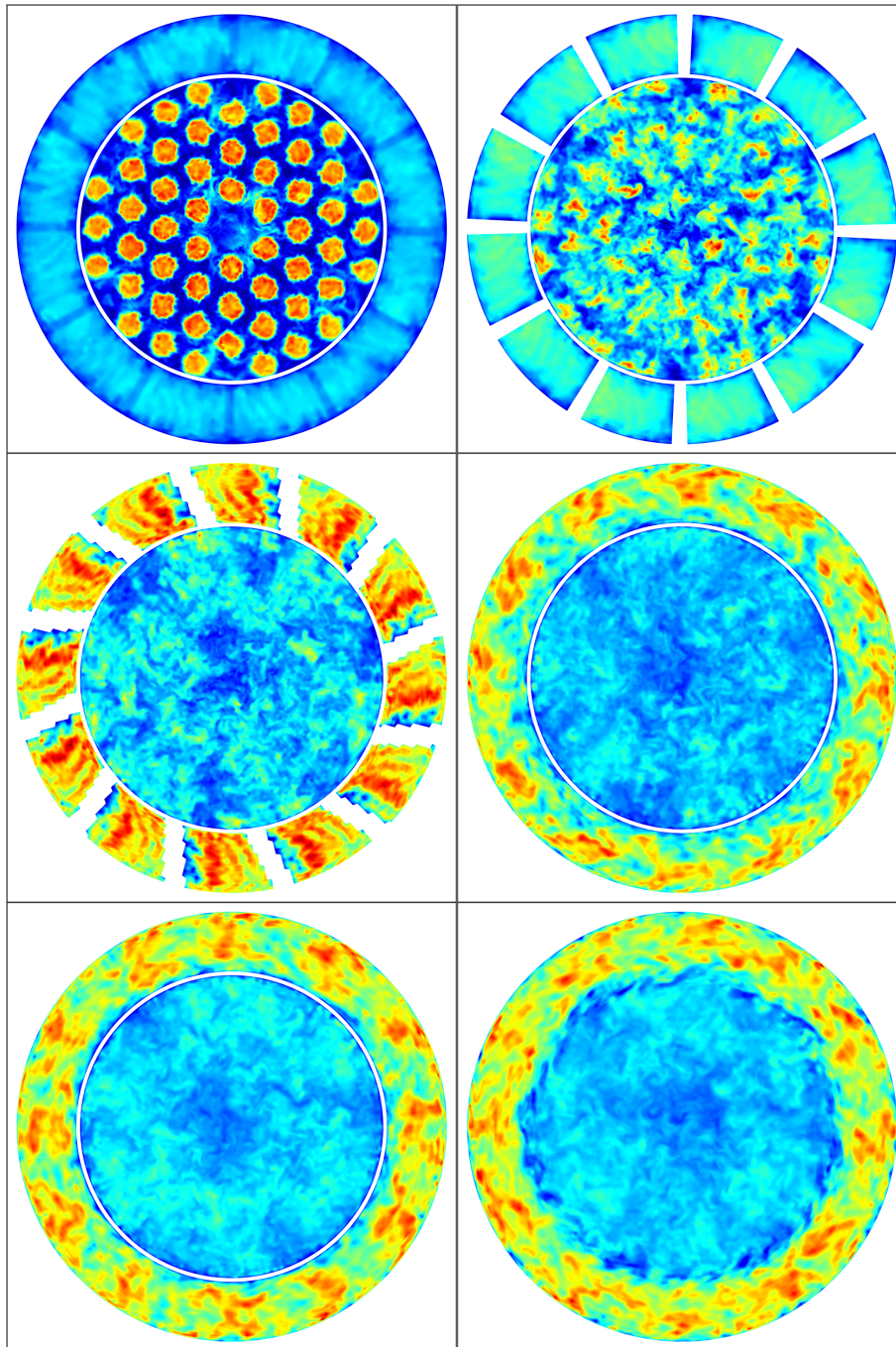
Figure 5.4: Two-dimensional contour plots of Velocity magnitude, $|\mathbf{u}|$, in the $r - \theta$ plane at locations marked in Fig. 5.3.

To close to the second term, one approach is to solve a governing equation for the filtered density function (FDF) [118]. However, the computational expense is greatly increased due to the need for instantaneous statistical convergence [81]. Furthermore, although the chemical source term appears explicitly in this formulation

and thus requires no closure, the FDF equations require closure for the molecular mixing, the modelling of which still remains a challenge [119].

A much simpler and computationally cheaper method is to presuppose a probability density function, which is characterized by a local value of the resolved progress variable (the mean), $\widetilde{C}$, and its second moment (the variance), C_v. The filtered source term is then expressed as:

$$\overline{\dot{\omega}}_C\left(\widetilde{C}, C_v\right) = \int_0^{C_{max}} \langle \dot{\omega}_C | C \rangle \, P\left(C | \widetilde{C}, C_v\right) dC \tag{5.2}$$

The table is filtered a priori according to Eq. (5.2) with a presumed pdf, and C_v is added as a table dimension. Although different presumed pdfs have been proposed [80], the standard method is the β-pdf [82, 120, 121], which is written:

$$P(C | \widetilde{C}, C_v) = \frac{c^{a-1} (1 - c)^{b-1}}{\int_0^1 c^{a-1} (1 - c)^{b-1} \, dC} \tag{5.3}$$

where

$$a = \widetilde{c}\left(\frac{\widetilde{c}\,(1 - \widetilde{c})}{C_v} - 1\right) \tag{5.4}$$

and

$$b = a\left(\frac{1}{\widetilde{c}} - 1\right) \tag{5.5}$$

where c is the normalized progress variable. The β-pdf is preferred because the distribution is flexible enough to represent the range of unmixed conditions (delta distributions) to well-mixed conditions (Gaussian distribution). The use of a β-pdf has been assessed a priori and a posteriori in low Karlovitz number flames by Mukhopadhyay et al. [122] and high Karlovitz number flames by Lapointe et al. [123, 124]. In the LES, C_v is calculated according to the algebraic model of Eq. (2.44) and used along with $\widetilde{C}$ to look up tabulated values.

5.3.2 Model 1: One equation with laminar source term

Based on the volume averaging concept of LES, Eq. (5.1) shows that the filtered source term should depend on the conditional mean source term $\langle \dot{\omega}_C | C \rangle$. Classically, this source term is assumed to be the same as the source term profile from the one-dimensional unstretched laminar flame. This model is expected to perform well for unity Lewis number fuels (e.g., methane), as the flame propagation is not dependent on curvature and differential diffusion effects. This model is the simplest, and will be used as a base case for comparison.

5.3.3   Model 2: One equation with turbulent source term

Equation (5.2) is valid when $C < C_{max}^{1D}$. However, for thermodiffusively unstable flames, as shown in Chapter 3, we have superadiabatic burning, and the progress variable can exceed the one-dimensional maximum. The filtered source term should be revisited. Following the derivation in Section 3.4, we decompose the volume integral into regions where $C \leq C_{max}^{1D}$ and where $C > C_{max}^{1D}$:

$$\overline{\dot{\omega}}_C = \frac{1}{V} \iiint_{C \leq C_{max}^{1D}} \dot{\omega}_C dV + \frac{1}{V} \iiint_{C > C_{max}^{1D}} \dot{\omega}_C dV \tag{5.6}$$

To first approximation and consistent with the discussion of the turbulent flame speed in Section 3.4, we express the second term as a fraction of the total integral using the superadiabatic ratio β. This results in:

$$\overline{\dot{\omega}}_C \approx \frac{1}{1 - \beta} \int_{C < C_{max}^{1D}} \langle \dot{\omega}_C | C \rangle P(C) dC \tag{5.7}$$

In Chapter 3, it was shown that for hydrogen flames, the shape of $\langle \dot{\omega}_C | C \rangle$ is strongly dependent on the turbulence intensity, which is characterized by the Karlovitz number. To determine the analogous source term for tabulation, an estimate of the Karlovitz number is thus required.
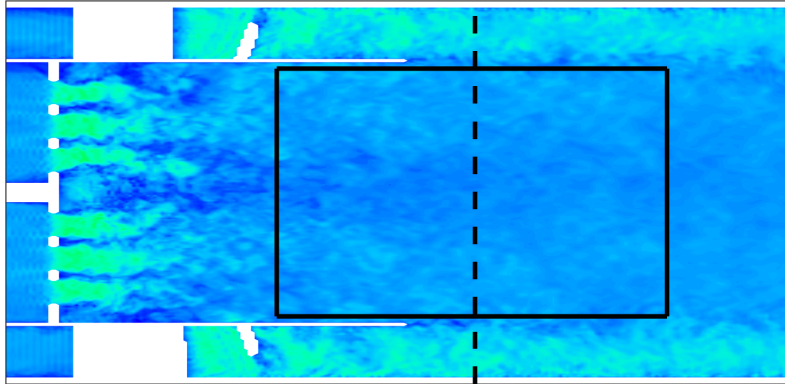
Figure 5.5: Two-dimensional contour of velocity magnitude through the swirler. The boxed area represents the region over which the estimated dissipation is calculated. The vertical dashed line represents the location where the inflow conditions for the combustion chamber were extracted.

Recall that the definition of the Karlovitz number, Eq. (3.2), depends on the turbulent dissipation, ε. To obtain an estimate of the turbulence intensity which would hit the flame, the dissipation is calculated within the center pipe region, characterized by grid decaying turbulence. The region of interest is shown in Fig. 5.5. The plane of extraction for the inlet boundary conditions of the combustion chamber is centered

within the region of interest. The dissipation is estimated as (see Chapter 5 of reference [125]):

$$\varepsilon = 2\left(v + v^t\right)\left\langle s_{ij}s_{ij}\right\rangle \tag{5.8}$$

where v^t is the kinematic eddy viscosity and s_{ij} is the fluctuating rate-of-strain tensor of the resolved filtered velocity. Averaging across the selected region provides an estimate of the dissipation of $\varepsilon \approx 700 \text{ m}^2/\text{s}^3$. Using this estimate of ε, an estimate of the Karlovitz number can be obtained as $Ka_u \approx 20$. This is close to case A, which has a dissipation of $\varepsilon_0 = 347$. For reference, case B has a dissipation of $\varepsilon_0 = 5571$, which is much higher than our estimate of ε. The results suggest that the conditional mean source term which should be tabulated is that of case A.

In summary, this model is the same as Model 1, except that the conditional mean source term is taken to be that of case A multiplied by $1/(1 - \beta)$ for $C \leq C_{max}^{1D}$. We use a constant value of β, with the assumption that the flame is characterized by one Karlovitz number, which is estimated at the centerline. The addition of β incorporates the effects of superadiabatic burning ($C > C_{max}^{1D}$).

5.3.4 Model 3: Two equations

To account for the effects of differential diffusion, Regele et al. [58] proposed a two-equation model. A mixture fraction-like variable, Z, was included to complement the progress variable and to capture fluctuations in the local equivalence ratio. Its transport equation included source terms resulting from differential diffusion. More recently, Schlup and Blanquart [33] re-derived the Z transport equation by lifting previous limiting assumptions made in [58] and by including Soret diffusion. For details on the derivation of the (C, Z) model, the reader is referred to [33]. The model has been validated across a wide range of configurations at DNS resolutions, including 1D, 2D, and 3D laminar freely propagating flames, 2D tubular flames, and 3D turbulent flames [126].

The filtered progress transport equation takes the same form as Eq. (2.27) with one difference. Now, $\dot{\omega}_C$ is a function of both C and Z. Following the a priori analysis of Berger et al. [63], the filtered source term can be expressed as:

$$\overline{\dot{\omega}}_C\left(\widetilde{C}, C_v, \widetilde{Z}\right) = \iint \dot{\omega}_C\left(C, \phi\right) P\left(C|\widetilde{C}, C_v\right) \delta\left(\phi - \hat{\phi}\right) dC d\phi \tag{5.9}$$

where δ is the delta distribution. To generate the table, one-dimensional flat flames at varying nominal equivalence ratios are filtered using a β-pdf in C. The results are tabulated in terms of $\widetilde{C}$, C_v, and $\widetilde{Z}$. Berger *et al.* [63] showed that using a

β-pdf for the progress variable significantly reduced the source term error, and including higher order moments did not significantly increase the accuracy of the LES modelling.

It is important to note that the two-equation model is meant to capture the combustion dynamics both across the flame, parameterized by $\widetilde{C}$, and along the flame front, parameterized by $\widetilde{Z}$. Differential diffusion effects are strongly coupled to the local flame curvature, with regions of positive curvature having locally rich mixtures, and regions of negative curvature having locally lean mixtures (center of curvature located in the burnt mixture). Thus, for the model to be most effective, the grid resolution should be sufficient to resolve smaller-scale structures on the order of the flame thickness.

5.3.5 Alternative modelling approaches

One of the criticisms of the presumed β-pdf method is that in one-dimensional laminar simulations of the filtered equations with such a source term, the laminar flame speed is not reproduced. A method which has been proposed to reproduce correctly this behaviour is to spatially filter the one-dimensional flamelets a priori, and construct a table based on the filtered flamelet profiles [127].

In this model, any quantity ϕ from the laminar one-dimensional unstretched flamelet is filtered analytically:

$$\overline{\phi}(x) = \int G(x - x')\, \phi(x')\, \mathrm{d}x' \tag{5.10}$$

where

$$G(x) = \left(\frac{6}{\pi \Delta^2}\right)^{1/2} \exp\left(-\frac{6x^2}{\Delta^2}\right) \tag{5.11}$$

is a one-dimensional Gaussian filtering kernel. The subfilter closure is then calculated analytically and necessary values are tabulated with respect to the filter width, Δ, and the progress variable, C. Although the model performs well in cases of uniform grids, in the presence of grid stretching or nonuniform grids the definition of the filter width can be ambiguous.

In their proposed model, the governing equation for C reads:

$$\frac{\partial \overline{\rho}\widetilde{C}}{\partial t} + \nabla \cdot \left(\overline{\rho}\widetilde{u}\widetilde{C}\right) = \nabla \cdot \left(\alpha_C \overline{\rho} D_C \nabla \widetilde{C}\right) + \overline{\dot{\omega}}_C + \Omega_C \tag{5.12}$$

where

$$\alpha_C\left(\widetilde{C}, \Delta\right) = \frac{\overline{\rho D_C |\nabla C^{1D}|}}{\overline{\rho} D_C |\nabla \widetilde{C^{1D}}|} \tag{5.13}$$

and

$$\Omega_C\left(\widetilde{C}, \Delta\right) = -\nabla \cdot \left(\overline{\rho u \widetilde{C^{1D}}} - \overline{\rho u}\widetilde{C^{1D}}\right) \tag{5.14}$$

are analytical subfilter scale closures for the diffusive and convective fluxes based on the filtered one-dimensional laminar profiles. The subfilter closure for the diffusive flux is shown in Fig. 5.6. Figure 5.6a shows $\widetilde{C}$ at varying filter widths. In all cases, the progress variable is monotonically increasing with x. As a result, the diffusive fluxes in Fig. 5.6b share the same sign, and the closure for α_C is well behaved (always positive).
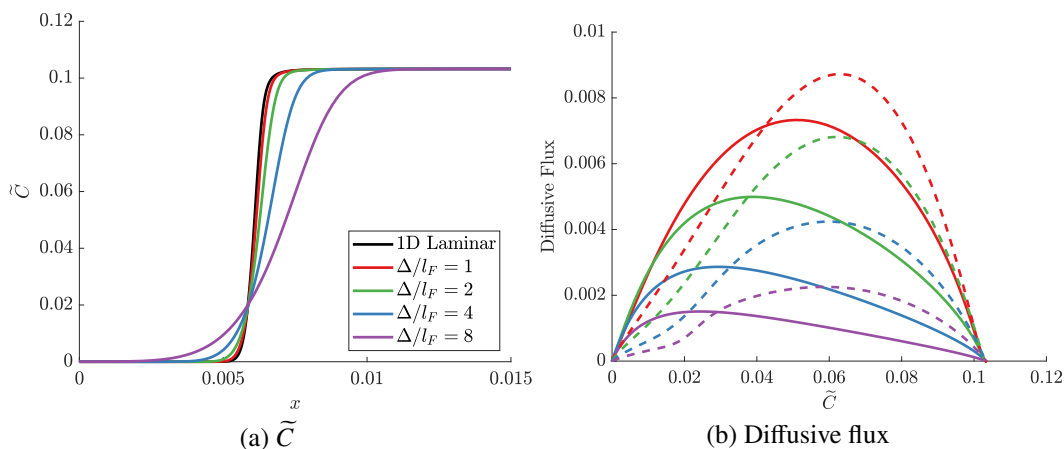
Figure 5.6: Profiles of $\widetilde{C}$ (a) and diffusive fluxes (b) at varying filter widths. For (b), the solid lines represent $\overline{\rho D_C |\nabla C^{1D}|}$, and the dashed lines represent $\overline{\rho} D_C |\widetilde{C^{1D}}|$.

To implement the spatially filtered LES framework in the two-equation model, similar closure terms would need to be derived for the $\widetilde{Z}$ equation. Figure 5.7 shows the same terms for the $\widetilde{Z}$ transport equation. Unlike the $\widetilde{C}$ profiles, the $\widetilde{Z}$ profiles in Fig. 5.7a are not monotonically increasing with x. This leads to two main issues. The first is that there are regions where the diffusive fluxes have opposite signs. This leads to negative values of α_Z, resulting in negative effective diffusion coefficients and introducing numerical instabilities. The second issue is that the profiles do not cross 0 at the same point, leading to singularities in the evaluation of α_Z.

5.4 LES results of the combustion chamber

The simulations of all combustion chambers are conducted on a cylindrical mesh of $N_x \times N_r \times N_\theta = 256 \times 120 \times 256$ grid points. Along the inlet pipe and combustion chamber walls, the grid is refined in the radial direction. The grid is uniform in the axial direction until $x = 0.08$ m before grid stretching is applied. This grid resolution is on the order of the laminar flame thickness at the flame front. The experimental
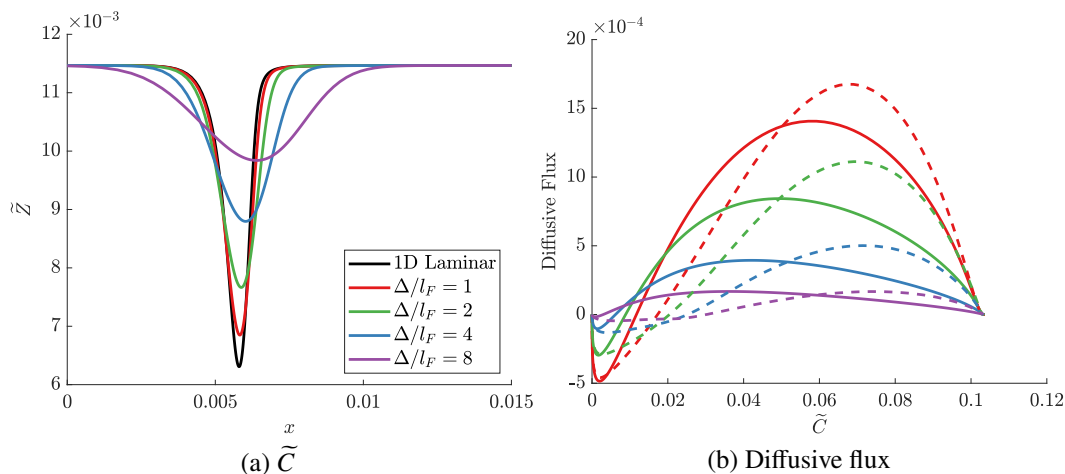
Figure 5.7: Profiles of $\widetilde{Z}$ (a) and diffusive fluxes (b) at varying filter widths. For (b), the solid lines represent $\overline{\rho D_Z |\nabla Z^{1D}|}$, and the dashed lines represent $\overline{\rho} D_Z |\widetilde{Z^{1D}}|$.

data used for comparison are taken from Cheng et al. [11], who measured the velocity fields using particle image velocimetry (PIV).

5.4.1 Methane flame

The first experiment under consideration is a lean premixed methane/air flame ($\phi = 0.59$). Because methane is a unity Lewis number fuel, this simulation is conducted with Model 1 (see Section 5.3.2). It serves to validate the boundary conditions, grid resolution, and treatment of the tabulated chemistry within the LES framework. The progress variable is defined as the sum of the mass fractions of CO_2, CO, H_2O, and H_2.

Figure 5.8 shows the instantaneous contour plots of the velocity magnitude and the progress variable. The flame location is marked with a black contour at C_{peak}, the location of the peak source term in progress variable space from the one-dimensional laminar flame. Because of the high axial velocity and high swirl, the flow at the edge of the inner pipe opens up (at an angle close to 45°) and creates a recirculation region slightly downstream of the inlet. This recirculation region is the key flow feature responsible for the stabilization of the flame front. The flame exhibits an "M" shape and is anchored at the edges of the inlet pipe. Because the combustion chamber is enclosed, hot gases are entrained in the recirculation regions in the corners and heat the outer shear layers that are associated with the inflow profile. Note that the present simulation framework does not include heat losses that are likely to occur at the burner exit, which may influence the visible luminosity of the flame.
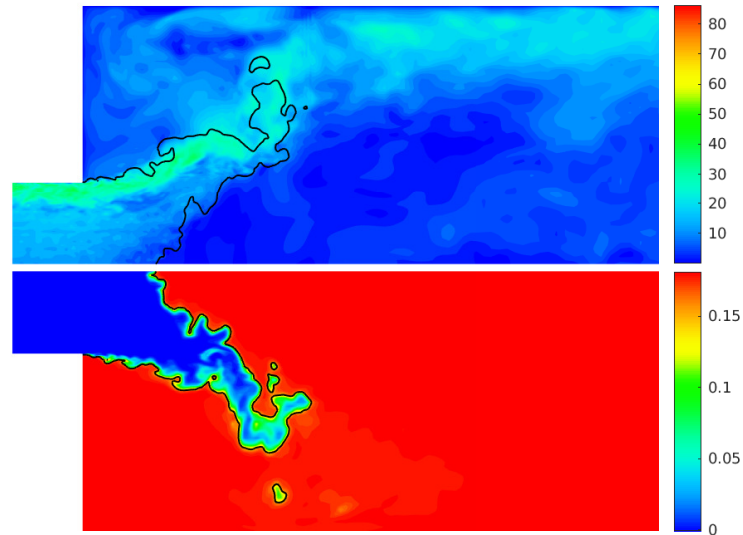
Figure 5.8: Instantaneous profiles of velocity magnitude (top) and progress variable (bottom) for the simulation of the turbulent flame of methane/air. An isocontour at $C_{peak} = 0.149$ indicates the location of the flame front (black line).

The mean centerline velocity is shown in Fig. 5.9. Close to $x = 0$ m, the experimental data exhibits some outliers, with some velocity measurements which are smaller than the neighbouring points. For completeness, we show the full range of experimental data. The decay of the mean axial velocity is well reproduced by the simulations. More importantly, the location of the recirculation zone (represented by a negative mean axial velocity) is captured reasonably well. The start of the recirculation region is at 4.7 cm from the simulation and 6.6 cm from the experiments.
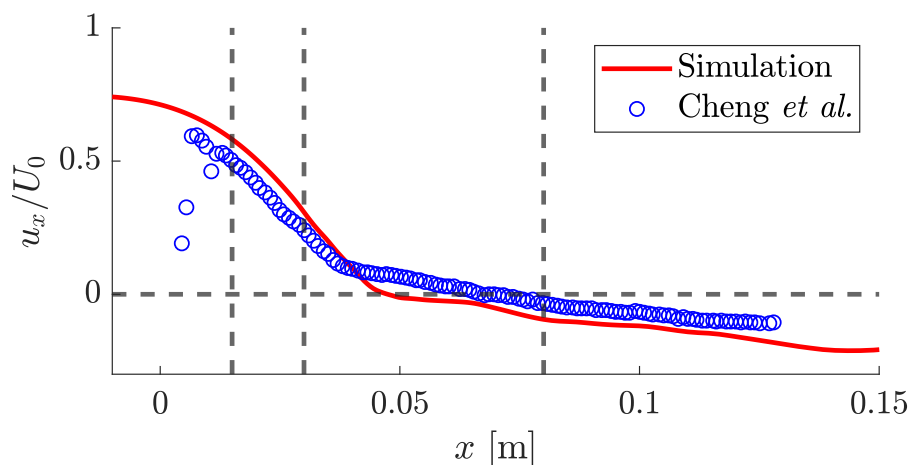
Figure 5.9: Mean axial velocity along the centerline of the methane flame. The vertical dashed lines represent stations at three axial locations where radial statistics are collected.

Three axial locations are chosen to investigate key regions of interest in the flow field. The station at $x = 0.015$ m is close to the inlet and serves to verify the inflow boundary conditions. The station at $x = 0.03$ m is chosen after the flow field starts to open, and as such, shows high sensitivity to the accuracy of the model. Finally, the station at $x = 0.08$ m is further into the chamber, and represents a region where the flow is fully opened and has had time to develop. The first two stations occur before the recirculation region, and the last one is further downstream.

The axial and radial velocity profiles at these three axial locations are compared in Fig. 5.10. In all cases the agreement is good. Some discrepancies in the mean quantities and fluctuations do exist, however. When considering these discrepancies, it is important to note that the experimental measurements suffer from some uncertainties. For instance, they are not perfectly symmetric and optical access to part of the domain was difficult (for $r < -30$ mm at $x = 80$ mm). The authors report contamination of the PIV data by laser reflection and particle deposition on the inner wall of the quartz enclosure [11]. Given these uncertainties, the agreement with experimental data is good, verifying the simulation framework.

5.4.2 Hydrogen flames

Cheng et al. [11] reported significant differences in the flow field between the methane and the hydrogen flames. In particular, they noted that the decay of the centerline velocity was lower, and there was larger acceleration in the post flame. This has the effect of pushing the inner recirculation region farther downstream, to $x \approx 0.13$ m.

The turbulent hydrogen flames are simulated using three different models, which are

- Model 1: $(\widetilde{C}, C_v)$ tabulation based on the one-dimensional laminar flamelet source term (see Section 5.3.2),

- Model 2: $(\widetilde{C}, C_v)$ tabulation based on the one-dimensional turbulent mean source term (see Section 5.3.3),

- Model 3: $(\widetilde{C}, C_v, \widetilde{Z})$ tabulation based on the work of Schlup and Blanquart [33] (see Section 5.3.4).

The progress variable fields for the two cases are shown in Fig 5.11. Differential diffusion has visible impacts on the flow field. There are two main observations.
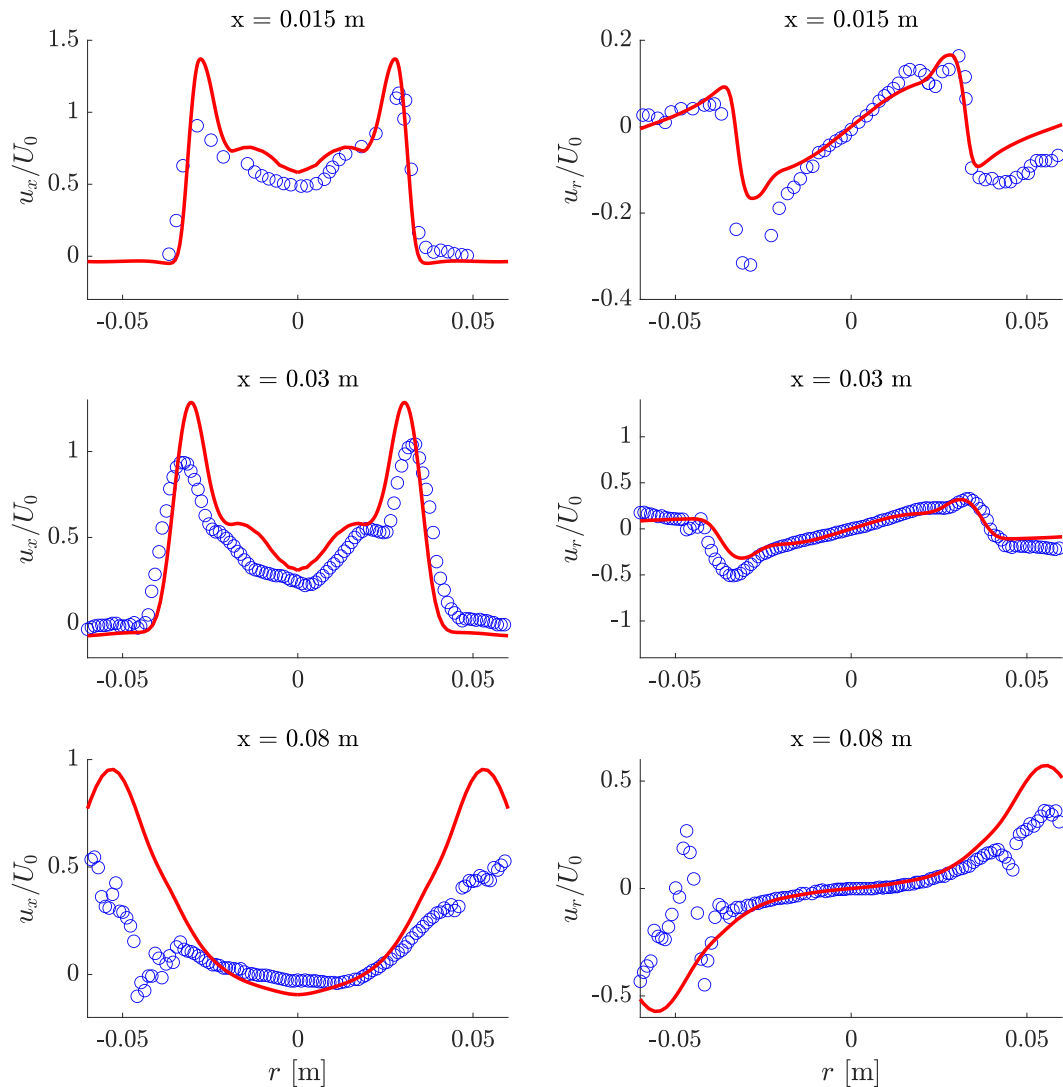
Figure 5.10: Mean radial profiles of the axial (top) and radial (bottom) velocity components of the methane/air flame.

First, in case 1, the flame looks qualitatively similar to the methane flame. This result is expected since the only two parameters which differ between the two simulations are the density ratio between burnt and unburnt gases and the laminar flame speeds. The turbulent flames appear slightly shorter, a result of the higher laminar flame speed ($S_L = 0.206$ m/s for H_2 versus $S_L = 0.102$ m/s for CH_4). In contrast, case 2 exhibits a much shorter flame and is anchored closer to the burner entrance. This observation is also true of case 3. However, there are significant progress variable fluctuations in the burnt gases of case 3, whereas the burnt gases of cases 1 and 2 are uniform. These fluctuations are attributed to Z capturing the curvature and differential diffusion effects.

(a) Case 1

(b) Case 2

(c) Case 3
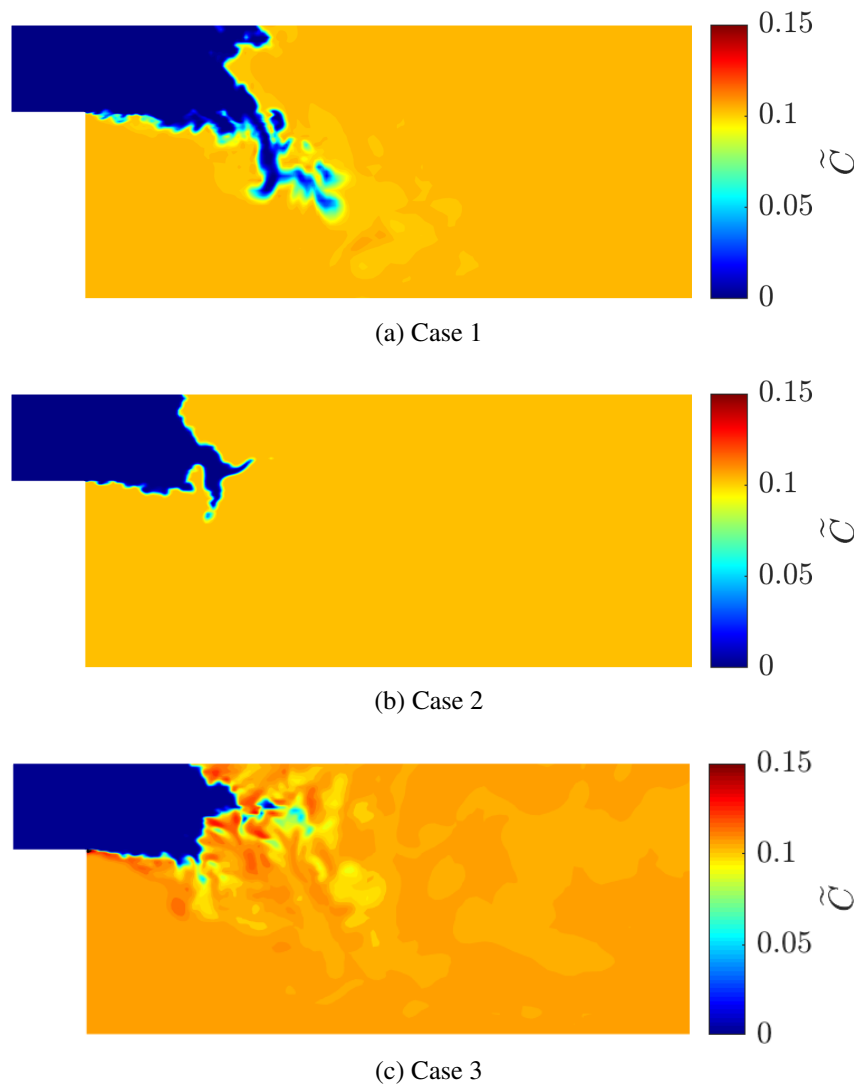
Figure 5.11: Progress variable fields for the two different hydrogen tabulated chemistry models.

The effect of the chemistry modelling on the flow field is illustrated in the mean velocity profiles shown in Figs. 5.12 and 5.13. In Fig. 5.12, the experimental data shows an increase in the mean axial velocity at the centerline after the flame, in clear contrast with the methane flame which shows a constant decay. This results in the recirculation region being pushed to $x \approx 0.13$ m. The $(\widetilde{C}, C_v)$ tabulation of case 1 completely fails to reproduce this unique flow feature, and the mean axial velocity decays just like that of the methane flame. Case 2 shows an increase in the post-flame axial velocity, as a result of the increased source term. Although the performance is superior to case 1, the peak is lower than the experimental measurements and the decay of the velocity profile is underpredicted. The velocity profile does not show the
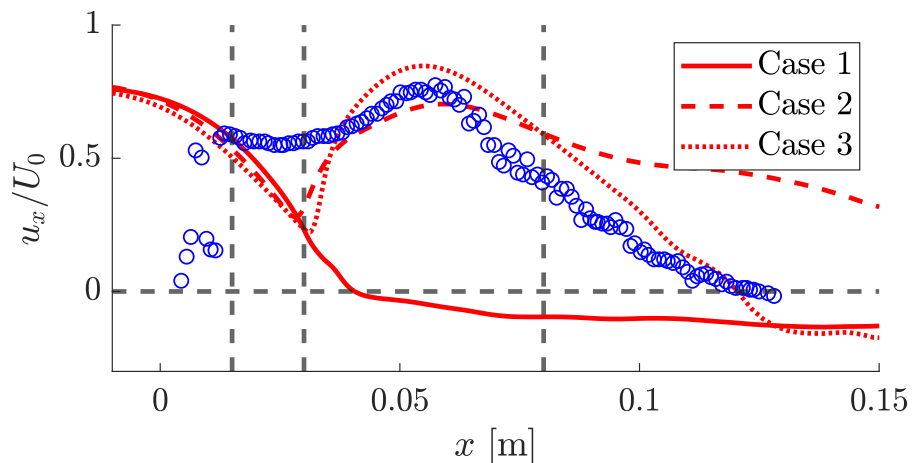
Figure 5.12: Mean axial velocity along the centerline of the hydrogen flame comparing the two LES models.

presence of a recirculation region. Case 3 is able to reproduce the increase in axial velocity, its subsequent decay, and the ultimate location of the recirculation region. Although there are improvements in the flow field prediction, the measured velocity profile is smoother in the post flame region, and does not exhibit the dip which is present in the simulation results. This could be due to underpredicted fluctuations in the x-direction. Additionally, Cheng et al. [11] reported significant broad-band noise generation from the hydrogen flame, which may play a role. However, acoustic effects are not captured by the present low Mach solver. Overall, the two-equation model, derived to capture the effects of curvature and differential diffusion, is able to reproduce the unique flow features compared to the one-equation model, even when tabulating the turbulent mean source term.

The failure of the one-equation model is further illustrated in Fig. 5.13. At the first station, the profiles show that case 1 does not have the correct spreading rate, as the radial velocity is underestimated compared to cases 2 and 3. At the second station, the radial velocity is still underpredicted for case 1, agrees well with case 2, and is slightly overpredicted for case 3. At the centerline, all cases underpredict the axial velocity. At the final station, cases 2 and 3 show the increase in axial velocity at and around the centerline, correctly reproducing the push of the recirculation region downstream. Overall, the modelling approaches in case 3 are able to overcome the deficiencies of the $(\widetilde{C}, C_v)$ tabulation of cases 1 and 2. For regions close to the inlet and flame, shown in Fig. 5.13, case 2 performs well. However, further downstream, case 2 fails to reproduce the flow field.

The velocity flow field is further examined in Fig. 5.14, which shows the mean
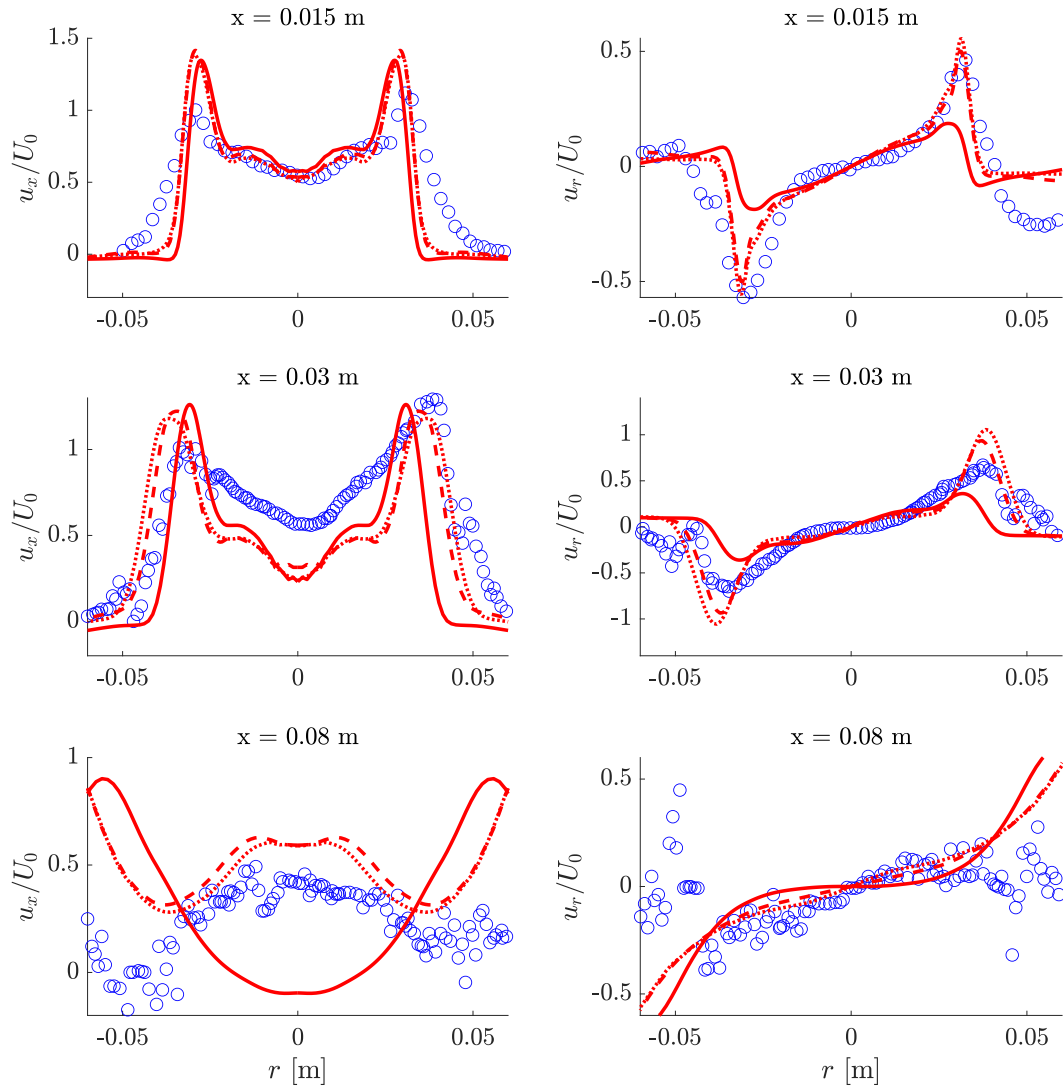
Figure 5.13: Mean radial profiles of the axial (top) and radial (bottom) velocity components of the hydrogen/air flame for cases 1 (solid), 2 (dashed), and 3 (dotted).

streamwise velocity, $\langle \widetilde{u} \rangle$, with streamlines superimposed. For case 1, the central recirculation zone dominates the central region of the chamber. For case 2, the post-flame acceleration is larger than expected. This causes the recirculation region to be destroyed, and the streamlines pass along the centerline directly to the outlet. Finally, for case 3, there still remains a central recirculation region. Compared to case 1, it is pushed further downstream and is much smaller in size.

To quantify the filtering of the LES, Fig. 5.15 shows the mean progress variable variance conditioned on $\widetilde{C}$ obtained from the simulations using model 2 compared to the variance obtained from filtering one-dimensional laminar flames. The one-dimensional flames are filtered with a Gaussian kernel at varying filter widths,

(a) Case 1

(b) Case 2

(c) Case 3
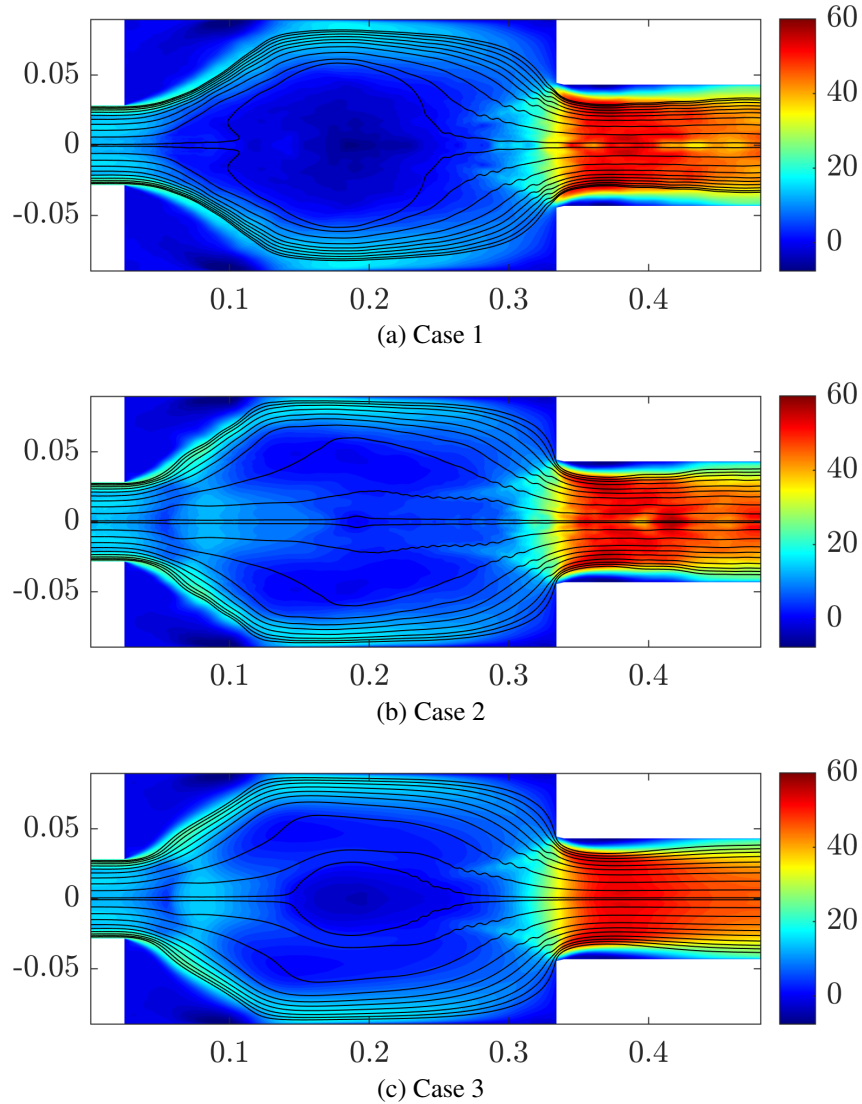
Figure 5.14: Mean $\widetilde{u}$ field with streamlines superimposed.

expressed as a multiple of the laminar flame thickness, and the variance is computed as:

$$C_v = \widetilde{CC} - \widetilde{C}\widetilde{C} \tag{5.15}$$

For values of $\widetilde{C}$ close to 0 and C_{max}^{1D} the variance predicted from the LES follows the profile of $\Delta = 2l_F$. At intermediate values of $\widetilde{C}$, the variance lies between $\Delta = 0.5l_F$ and $\Delta = l_F$. On average, the effective filter width that the flame experiences is on the order of the laminar flame thickness. Once again, values at $\widetilde{C} > C_{max}^{1D}$ correspond to superadiabatic burning, not present in one-dimensional flat flames. To measure the effect of the subfilter pdf modelling, the ratio of the source term sampled both with variance (β-pdf) and without variance (δ-pdf) is computed. For most of the values,

the values sampled using the β-pdf are below those of the δ-pdf. Overall, the ratio is within the range of 0.5 to 1.1. The pdf of the ratio is shown in Fig. 5.16.
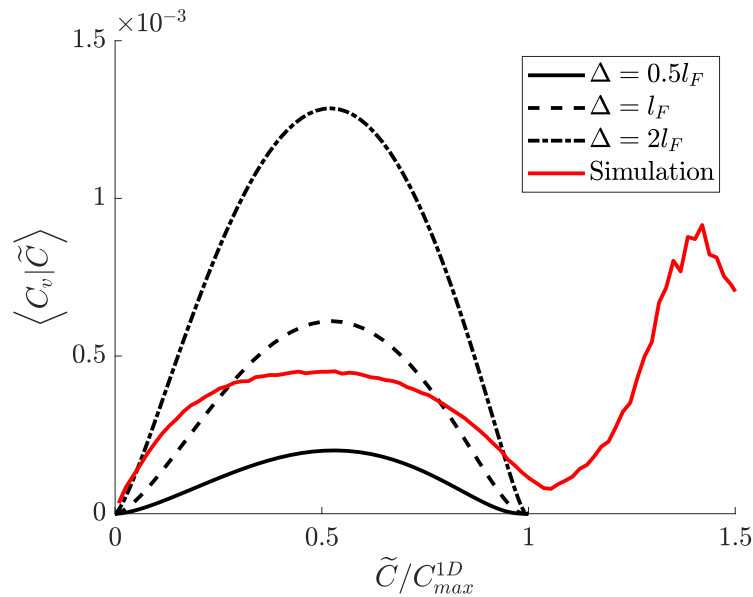
Figure 5.15: Conditional mean variance from the simulation (model 2) compared to variance obtained from filtering one-dimensional flames at varying filter widths Δ.
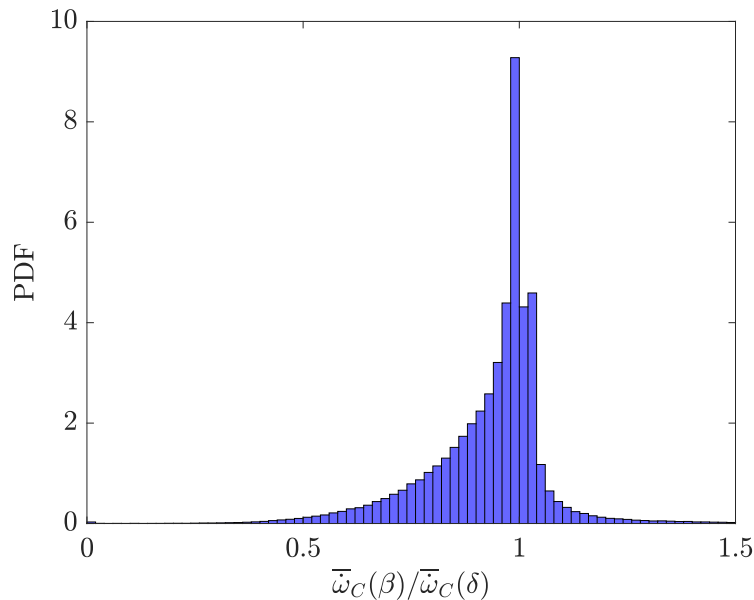
Figure 5.16: Probability density function of the ratio of source terms sampled using β-pdf and δ-pdf for $0.03 < \widetilde{C} < 0.1$.

Figure 5.17 shows a close-up view of the mixture fraction and normalized source term for model 2. The nominal value of the mixture fraction for the given equivalence

ratio is 0.0116. The $\widetilde{Z}$ field in Fig. 5.17 shows significant fluctuations along and behind the flame front. These fluctuations indicate significant differential diffusion effects since $\widetilde{Z}$ is meant to capture the effects of local fluctuations in the equivalence ratio. The effect on the flame can be seen in the plot of the normalized source term. There is a clear dependence on the flame geometry, where in regions of positive curvature (center of curvature located in the burnt mixture), the source term is seen to be greater than the one-dimensional laminar maximum. Conversely, in regions of negative curvature, the source term is reduced, and the flame is even extinguished in some areas. The addition of the Z equation is necessary to capture these geometry-dependent effects.
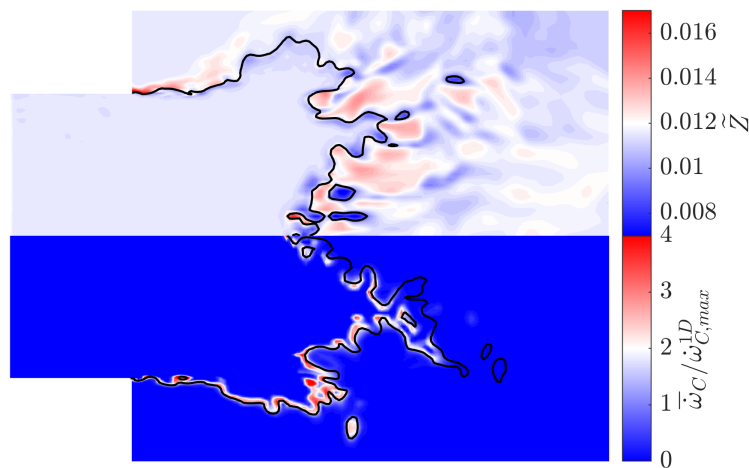
Figure 5.17: Close-up view of the mixture fraction (top) and normalized source term (bottom) for model 2. The black line is an isocontour at $C_{peak} = 0.0853$ to indicate the flame location.

5.4.3 A posteriori analysis of two-equation model

The conditional mean source terms of cases 2 and 3, $\left\langle \widetilde{\omega}_C | \widetilde{C} \right\rangle$, are shown in Fig. 5.18. The conditional source term of the DNS flame A, $\langle \dot{\omega}_C | C \rangle$, divided by $1 - \beta$ is also shown for comparison. As discussed in Section 5.3.3, this rescaled source term was used in the tabulation for case 2. The differences in the curves is a result of the LES filtering.

The results from the LES are similar in both shape and magnitude. As such, case 2 is able to reproduce many of the flow features that case 3 has, including an increased post-flame acceleration and better prediction of spreading rates. However, while case 2 may reproduce the mean source term of case 3, it does not capture any local variations in it. This may be the source of discrepancies between the two flow fields,

most importantly, that case 2 eliminates the recirculation region which is present in case 3.
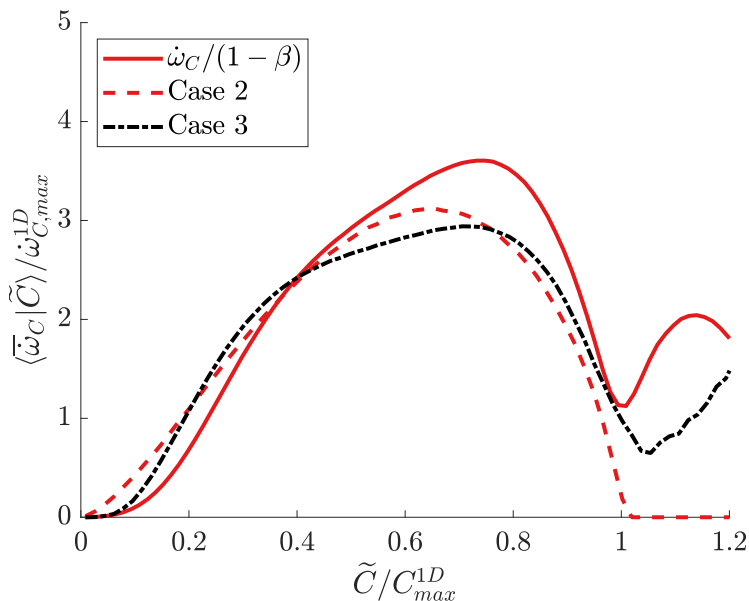
Figure 5.18: Conditional mean of the source term, $\left\langle \overline{\dot{\omega}}_C | \widetilde{C} \right\rangle$ compared to DNS results from Chapter 3.

5.5 Conclusions

Lean hydrogen premixed flames are subject to thermodiffusive instabilities that strongly influence local and global combustion properties. In this work, LES were conducted on a low-swirl burner using the tabulated chemistry framework. The simulations were conducted in two parts. First, a simulation of the LSI was performed using the immersed boundary method. This simulation was used to generate inflow boundary conditions for a second calculation of the combustion chamber.

The tabulated chemistry method was first validated on a methane/air flame at an equivalence ratio of $\phi = 0.59$, since it exhibits unity Lewis number behaviour. The flame opens up at about a 45 degree angle and is stabilized by the presence of a recirculation region. Then, LES were conducted on a premixed hydrogen/air flame at an equivalence ratio of $\phi = 0.4$. Due to differential diffusion effects, the hydrogen flame exhibits a unique flow field in the experiments. In particular, the recirculation region is pushed further downstream due to larger acceleration of the flow behind the flame.

Two filtered tabulation models were tested in the LES. The first is the classical one-equation tabulation, similar to the case of the methane flame. This method was

unable to reproduce correct mean statistics in terms of axial or radial velocity profiles. The second method was based on a two-equation tabulation, recently proposed by Schlup and Blanquart [33]. This model was able to capture the differential diffusion effects and reproduced successfully the unique flow field of the turbulent hydrogen flame. This work is the first successful application of the two-equation model in the LES framework.

Chapter 6

SUMMARY AND FUTURE DIRECTIONS

In this thesis, a comprehensive study of lean turbulent premixed hydrogen flames was conducted, ranging from DNS to LES. Besides fundamental studies, the results of the DNS were used to evaluate the validity of the effective Lewis number model and the two-equation tabulated chemistry model. Derived from the DNS results, the proposed LES framework has been validated against experimental results and could be used to investigate novel combustor designs.

6.1 Large- and small-scale turbulence effects

To perform a comprehensive study of the effects of turbulence on thermodiffusively unstable lean premixed hydrogen flames, a series of DNS was conducted across a wide range of Karlovitz numbers and integral length scale ratios. A generalized expression for the burning efficiency was proposed, which depends on the conditional mean source term, its gradient, and the percentage of superadiabatic burning. The burning efficiency increases before decreasing at the highest Karlovitz numbers. The assumptions of the previously proposed expression by Lapointe and Blanquart [43] do not hold in the case of thermodiffusively unstable flames. As such, their expression fails to reproduce the results of the newly proposed expression.

At a fixed Karlovitz number, the turbulent flame area, A_T, increases almost linearly with the integral length scale ratio, ℓ/l_F. The chemical source term shape does not show any significant differences. Thus, for a given Karlovitz number, the flame speed variation is directly controlled by the flame area, which is a global quantity. It is unclear whether the observed effects are a result of the integral length scale, or the domain size.

At a fixed integral length scale ratio, the flame speed and area both increase before decreasing at the highest Karlovitz number. This trend is attributed to the dampening of differential diffusion effects, due to the increased turbulent diffusivity. This is outlined by the observation that the shape of the chemical source term approaches that of the one-dimensional unity Lewis number flamelet. The propagation of the flames behaves as a material surface, and is thus attributed to the turbulence, and is not controlled by laminar instability structures.

A detailed discussion of the curvature effects on chemistry was also presented. The curvature of the flame scales with an intermediate quantity between the reaction zone thickness and the Kolmogorov length scale. To study the effects of chemistry, conditional sampling was conducted using the mixture fraction. In regions of positive curvature, the mixture fraction is higher than the nominal value, and in regions of negative curvature, the mixture fraction is lower. The conditional mean profile of Z_{mix} becomes almost constant with respect to C as the Karlovitz number is increased, further indicating that differential diffusion effects are being suppressed. The two-dimensional conditional mean source term, $\langle \dot{\omega}_C | \kappa, C \rangle$, shows significant differences in its shape and magnitude as the Karlovitz number increases. However, when conditioned in mixture fraction space, $\langle \dot{\omega}_C | Z_{mix}, C \rangle$, the profiles show a good collapse. This provides strong evidence for the validity of the two-equation tabulated chemistry model across the wide range of Karlovitz numbers present in this study.

Overall, the qualitative trends are not affected by Soret diffusion. However, the inclusion of Soret diffusion does have an impact on quantitative results. The mean flame speed is increased by 35% for case A and 15% for case C. This is reflected in an increase of the burning efficiency of approximately 10%.

6.2 Effective Lewis numbers

The effect of Soret diffusion and integral length scale ratio on the effective Lewis number model of Savard and Blanquart [19] was studied. It was shown that both the effective Lewis numbers and effective Soret diffusion needed to be used in conjunction. The effective Soret diffusion coefficients are shown to scale down by a factor of $1/(1 + \psi)$, where ψ is the ratio of turbulent to mixture thermal diffusivity.

When the Soret diffusion is properly accounted for, the results show excellent agreement with those of Savard and Blanquart [19]. A correction of their model is proposed. In their work, the asymptotic value at zero Karlovitz number was that of the one-dimensional laminar flame. However, we have shown that the correct asymptotic limit is that of the three-dimensional laminar flame. Although Soret diffusion changes the flame structures, it does not change the effective Lewis numbers.

It was hypothesized by Savard and Blanquart [19] that the small integral length scale ratio used in their study may have affected their scalings. We have shown that the integral length scale does not affect the flame structure, and as such, does not affect the identified effective Lewis numbers. The current results agree well with their proposed empirical model.

6.3 Large eddy simulations

In this work, LES were conducted on a low-swirl burning using the tabulated chemistry framework. Two main subfilter modelling strategies were explored. The filtered laminar flamelet method was shown to produce negative diffusion coefficients for the Z equation, thus leading to numerical instabilities. As such, we used the presumed β-pdf model, which was shown by Berger et al. [63] to perform well a priori.

The classical one-equation tabulation using the one-dimensional laminar flamelet source term failed to reproduce the unique flow field of hydrogen combustion. To obtain a more appropriate estimation of the mean flame speed, a conditional mean source term from the DNS results was also tested in the one-equation model. Although this model showed significant improvements over the laminar source term model, it exhibited excessive post-flame acceleration, and eliminated the main recirculation region. Finally, the two-equation model was shown to reproduce the mean velocity profiles and also the location of the recirculation region. The results also serve as an a posteriori evaluation of the presumed β-pdf subfilter scale model.

6.4 Future work

A few avenues of research which should be pursued further are identified here.

- The extraction of the effective Lewis numbers produces an estimate of the turbulent diffusivity, α_t. An evaluation of the turbulent diffusivity should be conducted via explicit filtering of the extensive DNS database for comparison and to further assess the validity of the model. The results could be used to inform flamelet based models for RANS.

- Further research should be conducted on identifying the effects of integral length scale on the flame dynamics. The present forcing method does not allow for the decoupling of the integral length scale and the domain size. This would clarify the cause of observed trends such as the almost linear increase of the flame area with the integral length scale ratio.

- The consideration of more complex physics should be added to the two-equation tabulated chemistry model. For example, wall heat loss effects may be important in the simulation of many industrial systems. The validity of incorporating enthalpy in the tabulation should be explored to make the model more widely applicable.

- Further investigation of the one-dimensional tabulation using turbulent quantities should be conducted. In this thesis, only the turbulent mean source term was tabulated. Other quantities, such as the diffusivity, may also need to be obtained either from the turbulent profiles or from the effective Lewis number model.

- The subfilter scale modelling of the two-equation tabulation should be further pursued to identify whether a different spatially filtered approach is applicable. Furthermore, besides local flame speed variations due to equivalence ratio fluctuations, there are local flame thickness variations, changing the characteristic length scale. Further research on LES modelling should investigate these effects.

- The two-equation tabulated chemistry model should be tested for other thermodiffusively unstable fuels, such as ammonia or blends of ammonia and hydrogen. The ability of the model to accurately predict emissions should also be investigated.

Appendix A

CONVERGENCE AND STABILITY OF THE MIDPOINT ITERATIVE TIME INTEGRATION OF THE LOW MACH NAVIER–STOKES EQUATIONS

The numerical stability of an explicit time integration scheme is often characterized by a CFL number, σ. Many practical applications, such as the injector and burner geometries used in Chapter 5, are naturally represented by cylindrical coordinates. In these cases, the limiting σ is in the azimuthal direction due to necessarily small arc lengths near the centerline. The CFL numbers in the radial and azimuthal directions are written as:

$$\sigma_r = \frac{u_r \Delta t}{\Delta r} \tag{A.1}$$

$$\sigma_\theta = \frac{u_\theta \Delta t}{r \Delta \theta} \tag{A.2}$$

For the first point away from the centerline, σ_r is evaluated at $r = \Delta r$, and σ_θ is evaluated at $r = \Delta r/2$ due to the staggering. Assuming that the magnitudes of u_r and u_θ are similar, then σ_θ is larger than σ_r by a factor of $2/\Delta\theta$. For reference, the simulations in Chapter 5 have $2/\Delta\theta = n_\theta/\pi = 256/\pi$.

In this Appendix, we study the numerical stability and convergence of the midpoint iterative time integration scheme which is used in NGA [64].

A.1 Sub-iterative fractional-step approach

For a constant density case, non-reacting flow, the equations presented in Chapter 2 may be written in a more compact way. First, the momentum equations are advanced. Then, continuity is enforced through the pressure Poisson equation. For a subiteration, k, and estimate for the velocity field, $\mathbf{u}^*$, the sub-iterative procedure is then split into three main steps:

1. Predictor

$$\frac{\mathbf{u}^* - \mathbf{u}^n}{\Delta t} = -\delta_{\mathbf{x}}(p_k) + f\left(\frac{1}{2}\left(\mathbf{u}^n + \mathbf{u}_k^{n+1}\right)\right) \tag{A.3}$$

2. Poisson equation for corrector

$$\delta_{\mathbf{x}}(\delta_{\mathbf{x}}(\delta p)) = \frac{1}{\Delta t}(\delta_{\mathbf{x}}(\mathbf{u}^*)) \tag{A.4}$$

3. Application of the correction

$$\mathbf{u}_{k+1} = \mathbf{u}^* - \Delta t \delta_{\mathbf{x}} \left(\delta p \right) \tag{A.5}$$

$$p_{k+1} = p_k + \delta p \tag{A.6}$$

where $\delta_{\mathbf{x}}$ is the finite difference gradient operator (see Eq. (2.49)), Δt is the timestep size, and δp is the necessary pressure change to enforce continuity. Steps 1–3 are repeated until convergence is satisfied, or until the maximum number of subiterations is reached. It is also important to note that the method is second-order in time for $k \geq 2$.

A.2 Semi-implicit iterative method

To increase numerical stability, Eq. (A.3) can be treated implicitly. Performing a Taylor series expansion, Eq. (2.61) is replaced by:

$$\left[1 - \frac{1}{2} \Delta t \frac{\partial f}{\partial u} \right] \left(u^*_{k+1} - u^{n+1}_k \right) = u^n - u^{n+1}_k + \Delta t f \left[\frac{1}{2} \left(u^n + u^{n+1}_k \right) \right] \tag{A.7}$$

where $\frac{\partial f}{\partial u}$ is the Jacobian matrix. The Jacobian matrix can be populated for an implicit treatment of individual terms of the governing equations (e.g., convective or diffusive terms). If the Jacobian matrix is set to zero, then the time integration scheme becomes an explicit iterative scheme. For more details, the reader is referred to [89, 88].

The Jacobian matrix is simplified through an approximate factorization [128]. If $\mathbf{A} = \frac{1}{2} \Delta t \frac{\partial f}{\partial u}$, then the approximate factorization is taken as:

$$\left(\mathbf{I} - \mathbf{A}_x - \mathbf{A}_y - \mathbf{A}_z \right) \approx \left(\mathbf{I} - \mathbf{A}_x \right) \left(1 - \mathbf{A}_y \right) \left(1 - \mathbf{A}_z \right) \tag{A.8}$$

The problem is thus reduced to the inversion of three poly-diagonal matrices for each momentum equation. The solution is obtained sequentially, treating each variable in each dimension separately. Despite the errors from the approximate factorization, it is important to note that the implicit correction aims to minimize the residual $u^{n+1}_{k+1} - u^{n+1}_k$, which is calculated for the full equation with no approximations.

A.3 Cartesian — Explicit formulation

In this section, the numerical stability of the explicit time integration scheme is discussed in the absence of viscosity. We consider first the case of the Cartesian coordinate system.

A.3.1 One-dimension — Longitudinal instabilities

The simplest test case is a strictly one-dimensional flow. In this case, the only instabilities which could appear would be in the direction of the mean flow. We refer to these instabilities as longitudinal instabilities. Consider a single velocity component, u_x, in the direction x. If we decompose the flow into mean and fluctuating components, $u_x(x) = \bar{u}_x(x) + u'_x(x)$, then the growth of $u'_x(x)$ can be predicted through a stability analysis of the predictor-corrector scheme.

Consider a case where there are instabilities present in the u^* field after the momentum predictor step, Eq. (A.3). The response of the pressure corrector step is explained as follows. The discretized one-dimensional Laplacian equation, Eq. (A.4), is:

$$\frac{u^*_{x,i_1+1} - u^*_{x,i_1}}{\Delta x} \frac{1}{\Delta t} = \frac{\delta p_{i_1+1} + \delta p_{i_1-1} - 2\delta p_{i_1}}{\Delta x^2} \tag{A.9}$$

Now, we consider the normal mode ansatz for both variables, namely $u^*_{x,i_1} = \widehat{u^*_x} e^{j(\kappa(i_1-\frac{1}{2})\Delta x)}$ and $\delta p_{i_1} = \widehat{\delta p} e^{j(\kappa i_1 \Delta x)}$, where $j^2 = -1$. The shift by $1/2$ accounts for the staggering of the variable and ultimately simplifies the expressions. Substituting these expressions into the discretized Laplacian equation, we obtain the following expression:

$$\frac{e^{j\kappa\Delta x/2} - e^{-j\kappa\Delta x/2}}{\Delta x} \widehat{u^*_x} \frac{1}{\Delta t} = \frac{e^{j\kappa\Delta x} + e^{-j\kappa\Delta x} - 2}{\Delta x^2} \widehat{\delta p} \tag{A.10}$$

or

$$\widehat{\delta p} = -\frac{j}{\Delta t \kappa''} \widehat{u^*_x} \tag{A.11}$$

where $\kappa'' = 2\sin(\kappa\Delta x/2)/\Delta x$ is the effective wavenumber. Similarly, the pressure correction step, Eq. (A.5), in one dimension takes the form:

$$u^{n+1}_{x,i_1} = u^*_{x,i_1} - \Delta t \frac{\delta p_{i_1} - \delta p_{i_1-1}}{\Delta x} \tag{A.12}$$

With the normal mode ansatz, it becomes:

$$\widehat{u^{n+1}_x} = \widehat{u^*_x} - \frac{\Delta t}{\Delta x}\left(e^{j\kappa\Delta x/2} - e^{-j\kappa\Delta x/2}\right)\widehat{\delta p} = \widehat{u^*_x} - \Delta t j \kappa'' \widehat{\delta p} \tag{A.13}$$

Substitution of Eq. A.11 into Eq. A.13 yields:

$$\widehat{u^{n+1}_x} = \widehat{u^*_x} - \widehat{u^*_x} = 0 \tag{A.14}$$

This result shows that the pressure predictor-corrector procedure acts to remove any longitudinal instabilities exactly within one timestep.

A.3.2 One-dimension — Transverse instabilities

The next step is to consider velocity fluctuations which are not in the direction of their respective velocity components. We refer to these as transverse instabilities. Because the pressure term in each momentum equation acts only in one direction, it only serves to remove the longitudinal instabilities. As such, pressure does not appear in the following von Neumann stability analysis.

We consider a uniform mean flow in the x direction, $\bar{u}_x > 0$, with fluctuation of a different velocity component along the x direction, $u'_y(x)$. In the limit of small perturbations, the linearized momentum equation is exactly the same as the traditional advection equation:

$$\frac{\partial \phi}{\partial t} + c\frac{\partial \phi}{\partial x} = 0 \tag{A.15}$$

where $\phi = u'_y$ is the transported quantity and $c = \bar{u}_x$ is the convective velocity. Similarly, the discretized momentum equation, Eq. (A.3), is equivalent to:

$$\frac{\partial \phi_{i_1}}{\partial t} + c\frac{\phi_{i_1+1} - \phi_{i_1-1}}{2\Delta x} = 0 \tag{A.16}$$

Introducing the normal mode ansatz, $\phi_{i_1} = \widehat{\phi}e^{j(i_1\kappa\Delta x)}$, the equation becomes:

$$\frac{\partial \widehat{\phi}}{\partial t} = -\frac{c}{2\Delta x}\left(e^{j\kappa\Delta x} - e^{-j\kappa\Delta x}\right)\widehat{\phi} = -jc\kappa'\widehat{\phi} \tag{A.17}$$

with the effective wavenumber $\kappa' = \sin(\kappa\Delta x)/\Delta x$. The wavenumber for the worst-case scenario corresponds to $\kappa\Delta x = \pi/2$ and $\kappa' = 1/\Delta x$. Hence, the equation can be simplified to:

$$\frac{\partial \widehat{\phi}}{\partial t} = -j\frac{c}{\Delta x}\widehat{\phi} \tag{A.18}$$

For one subiteration, the discrete equation becomes:

$$\frac{\widehat{\phi}^{n+1} - \widehat{\phi}^n}{\Delta t} = -j\frac{c}{\Delta x}\widehat{\phi}^n \tag{A.19}$$

Introducing the CFL number as $\sigma = c\Delta t/\Delta x$, we have:

$$\widehat{\phi}^{n+1} = \widehat{\phi}^n(1 - j\sigma) \tag{A.20}$$

and expressing the growth rate as $G = |\widehat{\phi}^{n+1}/\widehat{\phi}^n|$, the stability of one subiteration is characterized by:

$$|G_1|^2 = 1 + \sigma^2 \tag{A.21}$$

The process can be repeated iteratively to determine the dependence of the stability on the number of subiterations. For a total number of subiterations K, this can be expressed as:

$$\frac{\widehat{\phi}_K^{n+1} - \widehat{\phi}^n}{\Delta t} = -j \frac{c}{\Delta x} \frac{1}{2} (\widehat{\phi}^n + \widehat{\phi}_{K-1}^{n+1}) \tag{A.22}$$

The stability for two, three, and four subiterations is given as:

$$|G_2|^2 = 1 + \frac{\sigma^4}{4} \tag{A.23}$$

$$|G_3|^2 = 1 - \frac{\sigma^4}{4} + \frac{\sigma^6}{16} \tag{A.24}$$

$$|G_4|^2 = 1 - \frac{\sigma^6}{16} + \frac{\sigma^8}{64} \tag{A.25}$$

For one or two subiterations, the numerical method is unconditionally unstable. For three or four subiterations, the timesteps are stable if $\sigma \leq 2$ since the condition for stability is $|G| \leq 1$.

A.3.3   General multi-dimensional instabilities

The stability analysis presented in the previous section is now generalized for a three-dimensional flow with uniform mean velocities $\overline{u}_x$, $\overline{u}_y$, and $\overline{u}_z$. After linearization, the inviscid momentum equations become:

$$\frac{\partial u'_x}{\partial t} + \overline{u}_x \frac{\partial u'_x}{\partial x} + \overline{u}_y \frac{\partial u'_x}{\partial y} + \overline{u}_z \frac{\partial u'_x}{\partial z} = -\frac{\partial p'}{\partial x} \tag{A.26}$$

$$\frac{\partial u'_y}{\partial t} + \overline{u}_x \frac{\partial u'_y}{\partial x} + \overline{u}_y \frac{\partial u'_y}{\partial y} + \overline{u}_z \frac{\partial u'_y}{\partial z} = -\frac{\partial p'}{\partial y} \tag{A.27}$$

$$\frac{\partial u'_z}{\partial t} + \overline{u}_x \frac{\partial u'_z}{\partial x} + \overline{u}_y \frac{\partial u'_z}{\partial y} + \overline{u}_z \frac{\partial u'_z}{\partial z} = -\frac{\partial p'}{\partial z} \tag{A.28}$$

with $u'_x, u'_y, u'_z \ll \overline{u}_x, \overline{u}_y, \overline{u}_z$. For the fluctuating components, the normal mode ansatz is given as:

$$\phi'_{i_1 i_2 i_3} = \widehat{\phi} \exp \left[j \left(\kappa_x i_1 \Delta x + \kappa_y i_2 \Delta y + \kappa_z i_3 \Delta z \right) \right] \tag{A.29}$$

To account for the staggering, i_1, i_2, and i_3 may be offset by $1/2$, depending on the location of the variable of interest. After substitution, the spatially discretized momentum equations, Eqs. (A.26)-(A.28), are given as:

$$\frac{\partial \widehat{u}_x}{\partial t} + j \left(\overline{u}_x \kappa'_x + \overline{u}_y \kappa'_y + \overline{u}_z \kappa'_z \right) \widehat{u}_x = -j \kappa''_x \widehat{p} \tag{A.30}$$

$$\frac{\partial \widehat{u}_y}{\partial t} + j \left(\overline{u}_x \kappa'_x + \overline{u}_y \kappa'_y + \overline{u}_z \kappa'_z \right) \widehat{u}_y = -j \kappa''_y \widehat{p} \tag{A.31}$$

$$\frac{\partial \widehat{u}_z}{\partial t} + j \left(\overline{u}_x \kappa'_x + \overline{u}_y \kappa'_y + \overline{u}_z \kappa'_z \right) \widehat{u}_z = -j \kappa''_z \widehat{p} \tag{A.32}$$

with the effective wavenumbers $\kappa'_x = \sin(\kappa_x \Delta x)/\Delta x$ and $\kappa''_x = 2\sin(\kappa_x \Delta x/2)/\Delta x$. Similarly, the discretized continuity equation becomes:

$$\kappa''_x \widehat{u}_x + \kappa''_y \widehat{u}_y + \kappa''_z \widehat{u}_z = 0 \tag{A.33}$$

To study the time integration, we first consider the case of one subiteration. Since the pressure term is consistent between the predictor and corrector steps, it can be added fully in the corrector step. As such, the velocity components after the predictor step are:

$$\widehat{u}^*_x = (1 - j\Sigma)\,\widehat{u}^n_x \tag{A.34}$$

$$\widehat{u}^*_y = (1 - j\Sigma)\,\widehat{u}^n_y \tag{A.35}$$

$$\widehat{u}^*_z = (1 - j\Sigma)\,\widehat{u}^n_z \tag{A.36}$$

where $\Sigma = \Delta t\left(\overline{u}_x \kappa'_x + \overline{u}_y \kappa'_y + \overline{u}_z \kappa'_z\right)$. The corrector step follows as:

$$\widehat{u}^{n+1}_x = \widehat{u}^*_x - \Delta t\, j \kappa''_x \widehat{p} \tag{A.37}$$

$$\widehat{u}^{n+1}_y = \widehat{u}^*_y - \Delta t\, j \kappa''_y \widehat{p} \tag{A.38}$$

$$\widehat{u}^{n+1}_z = \widehat{u}^*_z - \Delta t\, j \kappa''_z \widehat{p} \tag{A.39}$$

An expression for $\widehat{p}$ can be obtained by substituting $\widehat{u}^{n+1}_x$, $\widehat{u}^{n+1}_y$, and $\widehat{u}^{n+1}_z$ into continuity, Eq. (A.33). After manipulation, the final equations can be expressed in matrix form:

$$\begin{bmatrix} \widehat{u}_x \\ \widehat{u}_y \\ \widehat{u}_z \end{bmatrix}^{n+1} = (1 - j\Sigma)\,\mathbf{A} \begin{bmatrix} \widehat{u}_x \\ \widehat{u}_y \\ \widehat{u}_z \end{bmatrix}^{n} \tag{A.40}$$

with

$$\mathbf{A} = \frac{1}{\kappa''^2_x + \kappa''^2_y + \kappa''^2_z} \begin{bmatrix} \kappa''^2_y + \kappa''^2_z & -\kappa''_x \kappa''_y & -\kappa''_x \kappa''_z \\ -\kappa''_y \kappa''_x & \kappa''^2_x + \kappa''^2_z & -\kappa''_y \kappa''_z \\ -\kappa''_z \kappa''_x & -\kappa''_z \kappa''_y & \kappa''^2_x + \kappa''^2_y \end{bmatrix} \tag{A.41}$$

The $\mathbf{A}$ matrix has two distinct eigenvalues, namely $\lambda_1 = 0$ and $\lambda_2 = 1$ (twice). The growth of either eigenvector associated with the larger eigenvalue, $\hat{\psi}_2$, is given by:

$$\hat{\psi}^{n+1}_2 = (1 - j\Sigma)\hat{\psi}^n_2 \tag{A.42}$$

This expression is similar to Eq. (A.20). The stability analysis for any number of subiterations can be derived in a manner similar to Section A.3.2.

In summary, the worst-case scenario for the 3D stability analysis (i.e., largest Σ) happens when the wavevector of the instability $(\kappa'_x, \kappa'_y, \kappa'_z)$ is aligned with the mean flow velocity vector $(\bar{u}_x, \bar{u}_y, \bar{u}_z)$. An upper limit is then $|\Sigma| \leq \sigma_x + \sigma_y + \sigma_z$, with $\sigma_x = |\bar{u}_x|\Delta t/\Delta x$, $\sigma_y = |\bar{u}_y|\Delta t/\Delta y$, and $\sigma_z = |\bar{u}_z|\Delta t/\Delta z$. The dependence on the CFL number and number of subiterations follows that of the 1D transverse instability case. Specifically, the stability of the system is controlled by the sum of the CFL numbers in the x, y, and z directions, namely $\sigma = \sigma_x + \sigma_y + \sigma_z < 2$ (for three or more subiterations). Note that this is a sufficient condition as $|\Sigma| \leq \sigma$).

A.3.4   Numerical verification

The stability is tested numerically in NGA in a series of two-dimensional and three-dimensional inviscid simulations on Cartesian grids. In each case, the flow is periodic in all three directions (x, y, and z); the domain size is $L_x = L_y = L_z = 1$; and the number of grid points is $n_x = n_y = n_z = 64$.

To test the one-dimensional transverse instabilities, the initial velocity profile corresponds to a mean flow in only one direction and perturbations in the other direction. Specifically:

$$u^0_x(x, y) = \bar{u}_x = 1 \tag{A.43}$$

$$u^0_y(x) = 1 \times 10^{-9} \sin\left(\frac{2\pi x}{4\Delta x}\right) \tag{A.44}$$

which corresponds to the most unstable mode identified in the previous sections. We also consider one-dimensional mean flows, $\bar{u}_x = 1$, two-dimensional mean flows, $\bar{u}_x = \bar{u}_y = 1$, and three-dimensional mean flows, $\bar{u}_x = \bar{u}_y = \bar{u}_z = 1$, with initial random perturbations of 1×10^{-9} amplitude.

For the one-dimensional transverse case, since there is no mean flow for u_y, the growth of the perturbations can be tracked directly by the maximum of its absolute value, $|u_y|_\infty$. The magnitude of the instability is expected to take the form:

$$|u^n_y|_\infty = G^n|u^0_y|_\infty \tag{A.45}$$

where n is the number of timesteps and G is the growth rate, which can be readily obtained from the results by calculating the slope of $|u^n_y|_\infty$ on a semi-logarithmic plot. An example of the growth of $|u^n_y|_\infty$ is shown in Fig. A.1 for four subiterations (see Eq. (A.25)). Results for three different CFL numbers are shown: $\sigma = 1.00$, which has a growth rate of $G = 0.9761$ compared to a predicted growth rate of $G_p = 0.9763$; $\sigma = 1.80$, which has a growth rate of $G = 0.7718$ compared to
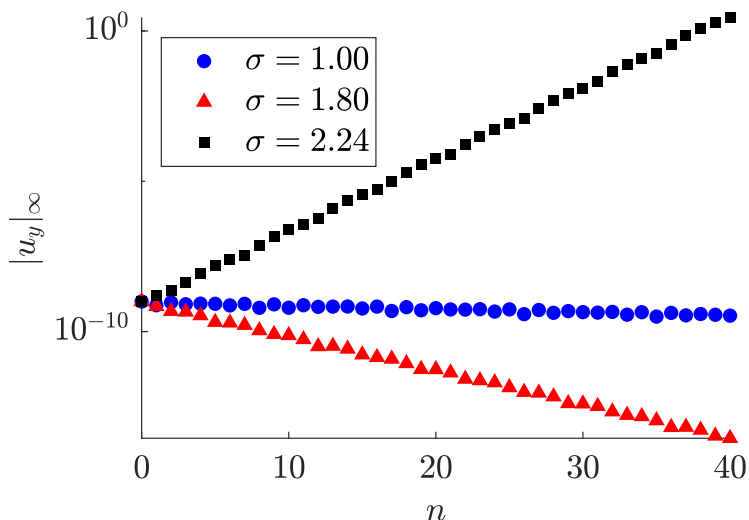
Figure A.1: Maximum of $|u_y|$ for a Cartesian flow consisting of a one-dimensional mean flow with transverse perturbations, integrated in time using 4 explicit subiterations.

$G_p = 0.7721$; and $\sigma = 2.24$, which has a growth rate of $G = 1.7335$ compared to $G_p = 1.7345$.

The measured and theoretical growth rates are compared further in Fig. A.2 as a function of σ. The data show excellent agreement. With three or four subiterations and $\sigma \leq 2$, the explicit midpoint iterative method is resistant to transverse instabilities in the absence of viscosity. The figure also shows results obtained with the two- and three-dimensional uniform velocity profiles. The results collapse perfectly when plotted versus the total CFL number, namely $\sigma = |\sigma_x| + |\sigma_y|$ in two dimensions and $\sigma = |\sigma_x| + |\sigma_y| + |\sigma_z|$ in three dimensions. It is noted that for the cases with random perturbations, the magnitude of the initial disturbances does not decrease as it does for the case with the most unstable mode when $\sigma < 2$. The initial perturbations are broad band with low wavenumbers that do not decay in time.

It should be noted there is a region between $\sigma \approx 1$ and $\sigma = 2$ where the growth rate dips significantly below 1. The perturbations at these σ are damped, which is beneficial for stability, but detrimental for preserving the total kinetic energy.

A.3.5 Convergence of explicit subiterations

In addition to studying the stability of the overall time integration, it is also important to consider the convergence of the subiterations within one timestep. Consistent with the results presented in the previous sections, we limit our analysis to one-dimensional transverse waves and the advection equation.
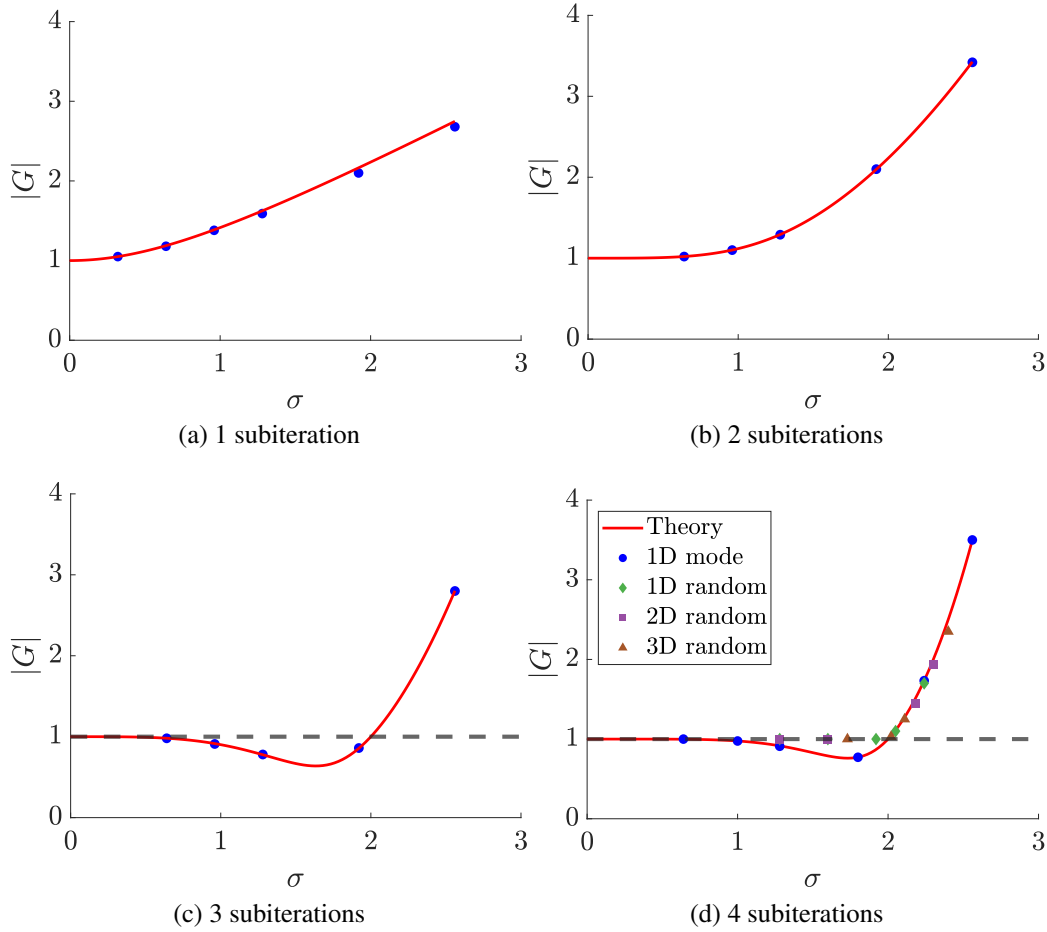
Figure A.2: Magnitude of the amplification factor of the explicit midpoint iterative method in Cartesian coordinates. The dashed line is at $r = 1$. For all the cases, the red line indicates the theory and the blue circles represent a one-dimensional simulation initialized with the most unstable mode. For four subiterations, the one-dimensional (green diamond), two-dimensional (purple square), and three-dimensional (brown triangle) cases shown are initialized using random perturbations.

Discretization of the advection equation via the midpoint iterative method yields:

$$\frac{\phi_{i_1,k+1}^{n+1} - \phi_{i_1}^n}{\Delta t} + c \frac{1}{2\Delta x} \left[\frac{1}{2} \left(\phi_{i_1+1}^n + \phi_{i_1+1,k}^{n+1} \right) - \frac{1}{2} \left(\phi_{i_1-1}^n + \phi_{i_1-1,k}^{n+1} \right) \right] = 0 \qquad \text{(A.46)}$$

To investigate the convergence of the subiterations, it is convenient to consider first the changes in the variable between two consecutive subiterations, namely $\delta\phi_{i_1,k+1} = \phi_{i_1,k+1}^{n+1} - \phi_{i_1,k}^{n+1}$. Substitution of the normal mode ansatz for $\delta\phi$ results in:

$$\widehat{\delta\phi}_{k+1} = -\frac{1}{2} c \Delta t j \kappa' \widehat{\delta\phi}_k \qquad \text{(A.47)}$$

For the worst-case scenario, $\kappa \Delta x = \pi/2$, and

$$\widehat{\delta\phi}_{k+1} = -j\frac{\sigma}{2}\widehat{\delta\phi}_k \tag{A.48}$$

The convergence of the geometric sequence is assured if the geometric ratio $r = \sigma/2 < 1$ or $\sigma < 2$. By realizing that $\phi_{i_1,k}^{n+1} = \phi_{i_1,0}^{n+1} + \sum_1^k \delta\phi_{i_1,m}$ is a geometric series with the same geometry ratio, the condition $\sigma < 2$ is also the necessary condition to ensure the convergence of the subiterations.

To test the stability of the subiterations, the same one-dimensional mean flow with transverse perturbations was simulated using 100 subiterations. For one timestep, the residual of u_y, $u_{y,k+1} - u_{y,k}$, is plotted against the subiteration in Fig. A.3 for three different σ. For $\sigma \leq 2$, the residual is decaying, indicating that the subiterations are converging. When σ is increased slightly above the stability limit to 2.048, the subiterations do not converge. Consequently, the overall timestep is also unstable and the solution diverges. The growth rates are also compared to the theoretical result of Eq. (A.48) and show good agreement.

(a) Residual of u_y
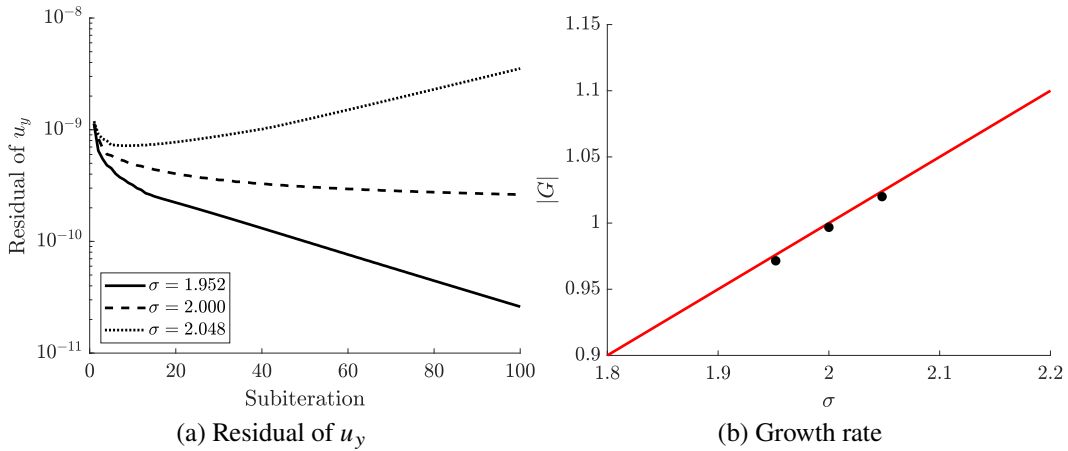
(b) Growth rate

Figure A.3: The residual of u_y versus the subiteration for the explicit iterative time integration in Cartesian coordinates (a) and associated growth rate compared to the theory (b).

A.4 Cylindrical — Explicit formulation

The cylindrical coordinate system introduces additional terms in the governing equations which may have implications on the stability of the time integration. In this section, we review the stability with regards to these specific aspects.

A.4.1 Expansion at centerline

Lele and Constantinescu [129] generalized series expansions for multivalued quantities on the centerline, namely u_θ and u_r. These expansions take the form:

$$M(r,\theta) = \frac{1}{r} \sum_{n=1}^{\infty} A_{0n} r^{2n} + \sum_{m=1}^{\infty} r^{m-1} \left(\sum_{n=0}^{\infty} A_{mn} r^{2n} \right) \cos(m\theta)$$

$$+ \sum_{m=1}^{\infty} r^{m-1} \left(\sum_{n=0}^{\infty} B_{mn} r^{2n} \right) \sin(m\theta) \tag{A.49}$$

For incompressible flows, the continuity equation in cylindrical coordinates with no axial flow is written:

$$\frac{1}{r} \frac{\partial r u_r}{\partial r} + \frac{1}{r} \frac{\partial u_\theta}{\partial \theta} = 0 \tag{A.50}$$

From here, the expressions for u_r and u_θ close to $r = 0$ can be written:

$$u_r = A \cos(\theta) + B \sin(\theta) \tag{A.51}$$

$$u_\theta = B \cos(\theta) - A \sin(\theta) + Cr \tag{A.52}$$

Although the governing equations have a singularity due to the $1/r$ term, the singularity is not physical as it does not appear in the solution for the velocity components. There are two key observations. The first is that the expression for u_r does not have an r dependence, whereas the expression for u_θ does. Secondly, the solution at the centerline accommodates two basic flows, namely, a uniform flow (corresponding the cos and sin terms) and a solid body rotation (corresponding to the r term). The stability of these two canonical flows is the subject of the following subsections.

A.4.2 General cylindrical stability

We repeat the stability analysis of section A.3.3 in cylindrical coordinates with a mean flow in the axial, $\bar{u}_x$, radial, $\bar{u}_r$, and azimuthal, $\bar{u}_\theta$, directions. No assumptions are made concerning the mean flow, besides verification of continuity. After linearization, the inviscid momentum equations become:

$$\frac{\partial u_x'}{\partial t} + \bar{u}_x \frac{\partial u_x'}{\partial x} + \bar{u}_r \frac{\partial u_x'}{\partial r} + \frac{\bar{u}_\theta}{r} \frac{\partial u_x'}{\partial \theta} = -\frac{\partial p'}{\partial x} \tag{A.53}$$

$$\frac{\partial u_r'}{\partial t} + \bar{u}_x \frac{\partial u_r'}{\partial x} + \bar{u}_r \frac{\partial u_r'}{\partial r} + \frac{\bar{u}_\theta}{r} \frac{\partial u_r'}{\partial \theta} - 2\frac{\bar{u}_\theta}{r} u_\theta' = -\frac{\partial p'}{\partial r} \tag{A.54}$$

$$\frac{\partial u_\theta'}{\partial t} + \bar{u}_x \frac{\partial u_\theta'}{\partial x} + \bar{u}_r \frac{\partial u_\theta'}{\partial r} + \frac{\bar{u}_\theta}{r} \frac{\partial u_\theta'}{\partial \theta} + \frac{\bar{u}_\theta}{r} u_r' = -\frac{1}{r} \frac{\partial p'}{\partial \theta} \tag{A.55}$$

with $u_x', u_r', u_\theta' \ll \bar{u}_x, \bar{u}_r, \bar{u}_\theta$. The normal mode ansatz for the fluctuating components is given as:

$$\phi_{i_1 i_2 i_3}' = \widehat{\phi} \exp\left[j \left(\kappa_x i_1 \Delta x + \kappa_r i_2 \Delta r + \kappa_\theta i_3 \Delta\theta \right) \right] \tag{A.56}$$

The discretized momentum equations become:

$$\frac{\partial \widehat{u}_x}{\partial t} + j \left(\overline{u}_x \kappa'_x + \overline{u}_r \kappa'_r + \overline{u}_\theta \kappa'_\theta \right) \widehat{u}_x = -j \kappa''_x \widehat{p} \tag{A.57}$$

$$\frac{\partial \widehat{u}_r}{\partial t} + j \left(\overline{u}_x \kappa'_x + \overline{u}_r \kappa'_r + \overline{u}_\theta \kappa'_\theta \right) \widehat{u}_r - 2\frac{\overline{u}_\theta}{r} \widehat{u}_\theta = -j \kappa''_r \widehat{p} \tag{A.58}$$

$$\frac{\partial \widehat{u}_\theta}{\partial t} + j \left(\overline{u}_x \kappa'_x + \overline{u}_r \kappa'_r + \overline{u}_\theta \kappa'_\theta \right) \widehat{u}_\theta + \frac{\overline{u}_\theta}{r} \widehat{u}_r = -j \kappa''_\theta \widehat{p} \tag{A.59}$$

with the effective wavenumbers $\kappa'_\theta = \sin(\kappa_\theta \Delta\theta)/r\Delta\theta$ and $\kappa''_\theta = 2\sin(\kappa_\theta \Delta\theta/2)/r\Delta\theta$. Finally, the continuity equation takes the form:

$$\kappa''_x \widehat{u}_x + \left(\frac{1}{r} + \kappa''_r \right) \widehat{u}_r + \kappa''_\theta \widehat{u}_\theta = 0 \tag{A.60}$$

Now, we consider the time integration with one subiteration. Assuming once again that the pressure term is added fully in the corrector step, the velocity components after the predictor step are:

$$\widehat{u}_x^* = (1 - j\sigma) \widehat{u}_x^n \tag{A.61}$$

$$\widehat{u}_r^* = (1 - j\sigma) \widehat{u}_r^n + 2\beta \widehat{u}_\theta^n \tag{A.62}$$

$$\widehat{u}_\theta^* = (1 - j\sigma) \widehat{u}_\theta^n - \beta \widehat{u}_r^n \tag{A.63}$$

with $\sigma = \Delta t \left(\overline{u}_x \kappa'_x + \overline{u}_r \kappa'_r + \overline{u}_\theta \kappa'_\theta \right)$ and $\beta = \Delta t \overline{u}_\theta / r$. The corrector step follows as:

$$\widehat{u}_x^{n+1} = \widehat{u}_x^* - \Delta t j \kappa''_x \widehat{p} \tag{A.64}$$

$$\widehat{u}_r^{n+1} = \widehat{u}_r^* - \Delta t j \kappa''_r \widehat{p} \tag{A.65}$$

$$\widehat{u}_\theta^{n+1} = \widehat{u}_\theta^* - \Delta t j \kappa''_\theta \widehat{p} \tag{A.66}$$

An expression for $\widehat{p}$ can be obtained by substituting $\widehat{u}_x^{n+1}$, $\widehat{u}_r^{n+1}$, and $\widehat{u}_\theta^{n+1}$ into continuity, Eq. (A.60). After manipulation, the final equations can be expressed in matrix form:

$$\begin{bmatrix} \widehat{u}_x \\ \widehat{u}_r \\ \widehat{u}_\theta \end{bmatrix}^{n+1} = \left[(1 - j\sigma) \, \mathbf{A} + \beta \, \mathbf{B} \right] \begin{bmatrix} \widehat{u}_x \\ \widehat{u}_r \\ \widehat{u}_\theta \end{bmatrix}^n \tag{A.67}$$

with

$$\mathbf{A} = \frac{1}{\kappa''^2_x + \kappa''^2_r + \frac{\kappa''_r}{r} + \kappa''^2_\theta} \begin{bmatrix} \kappa''^2_r + \frac{\kappa''_r}{r} + \kappa''^2_\theta & -\kappa''_x \left(\kappa''_r + \frac{1}{r} \right) & -\kappa''_x \kappa''_\theta \\ -\kappa''_r \kappa''_x & \kappa''^2_x + \kappa''^2_\theta & -\kappa''_r \kappa''_\theta \\ -\kappa''_\theta \kappa''_x & -\kappa''_\theta \left(\kappa''_r + \frac{1}{r} \right) & \kappa''^2_x + \kappa''^2_r + \frac{\kappa''_r}{r} \end{bmatrix} \tag{A.68}$$

and

$$\mathbf{B} = \frac{1}{\kappa_x''^2 + \kappa_r''^2 + \frac{\kappa_r''}{r} + \kappa_\theta''^2} \begin{bmatrix} 0 & \kappa_x'' \kappa_\theta'' & -2\kappa_x'' \left(\kappa_r'' + \frac{1}{r} \right) \\ 0 & \kappa_r'' \kappa_\theta'' & 2 \left(\kappa_x''^2 + \kappa_\theta''^2 \right) \\ 0 & -\left(\kappa_x''^2 + \kappa_r''^2 + \frac{\kappa_r''}{r} \right) & -2\kappa_\theta'' \left(\kappa_r'' + \frac{1}{r} \right) \end{bmatrix} \quad \text{(A.69)}$$

The **A** matrix has two distinct eigenvalues, namely $\lambda_1 = 0$ and $\lambda_2 = 1$ (twice). In the absence of the **B** matrix, the dynamics of Eq. (A.67) reflect that of Eq. (A.40). In other words, the stability of the cylindrical swirling flows would follow the same criteria as the previous Cartesian cases.

While the **B** matrix arises from $1/r$ terms in the radial and azimuthal momentum equations, its magnitude is the smallest at the centerline. At the first cell away from the centerline, the azimuthal wavenumber, κ_θ'', is larger than the radial wavenumber, κ_r'' by $n_\theta/\pi \gg 1$. In the limit of high azimuthal grid refinement, close to the centerline, the linear system (Eq. A.67) can be approximated by:

$$\begin{bmatrix} \widehat{u}_x \\ \widehat{u}_r \\ \widehat{u}_\theta \end{bmatrix}^{n+1} \approx \begin{bmatrix} 1 - j\sigma & 0 & 0 \\ 0 & 1 - j\sigma & 2\beta \\ 0 & 0 & 0 \end{bmatrix} \begin{bmatrix} \widehat{u}_x \\ \widehat{u}_r \\ \widehat{u}_\theta \end{bmatrix}^n \quad \text{(A.70)}$$

From this, we can conclude that the **B** does not impact the stability of the numerical system at small radii as the eigenvalues remain $1 - j\sigma$ (twice). The **B** matrix does impact the stability at large radii. Unfortunately, no general analytical solutions exist.

Consider a swirling flow with a mean axial velocity. Recognizing that σ is the largest when the effective wavevector is aligned with the mean flow vector, i.e., $(\kappa_x', \kappa_r', \kappa_\theta') \propto (\overline{u}_x, \overline{u}_r, \overline{u}_\theta)$, it is safe to neglect κ_r'' in the absence of mean radial velocity. Similarly, away from the centerline, we may neglect the $1/r$ terms. The remaining **B** matrix depends only on κ_x'' and κ_θ'', and its eigenvalues are $\pm j\sqrt{2}\kappa_x''/\sqrt{\kappa_x''^2 + \kappa_\theta''^2}$. In the worst-case scenario, the eigenvectors of **A** and **B** are aligned. When three or more subiterations are used, the stability criterion becomes:

$$|\sigma_x| + |\sigma_\theta| + |\beta| \sqrt{\frac{2\overline{u}_x^2}{\overline{u}_x^2 + \overline{u}_\theta^2}} < 2 \quad \text{(A.71)}$$

At worst, the factor multiplying β is $\sqrt{2}$.

A.4.3 Numerical verification

The stability is tested numerically in a series of two-dimensional and three-dimensional inviscid simulations on cylindrical grids. In each case, the flow is periodic in two

directions (x and θ); the domain size is $L_x = L_r = 1$ and $L_\theta = 2\pi$; and the number of grid points is $n_x = n_r = n_\theta = 64$.

Consistent with the expansion at $r = 0$ presented in section A.4.1, two different mean flows are considered. The first initial profile is taken to be that of a uniform flow in Cartesian coordinates. In cylindrical coordinates, the corresponding discrete velocity profile is given by:

$$\bar{u}_\theta(x, r, \theta) = \sin\theta \tag{A.72}$$

$$\bar{u}_r(x, r, \theta) = -\frac{\sin(\theta + \Delta\theta/2) - \sin(\theta - \Delta\theta/2)}{\Delta\theta} \approx -\cos\theta \tag{A.73}$$

Using the above expression for the radial velocity is important to ensure the mean flow verifies the continuity equation discretely. This mean flow is superimposed with random fluctuations in the axial velocity (of 1×10^{-9} amplitude). The mean flow is also used as Dirichlet boundary conditions at the outer edge in the r direction.

The second initial profile corresponds to that of a solid body rotation with mean axial velocity and random perturbations in the radial velocity (of 1×10^{-9} amplitude). Specifically:

$$\bar{u}_x(x, r, \theta) = const \tag{A.74}$$

$$\bar{u}_\theta^0(x, r, \theta) = r \tag{A.75}$$

In the absence of perturbations, the initial profile satisfies discretely continuity. Neumann boundary conditions are used at the outer edge in the r direction.

(a) Uniform flow   (b) Swirl
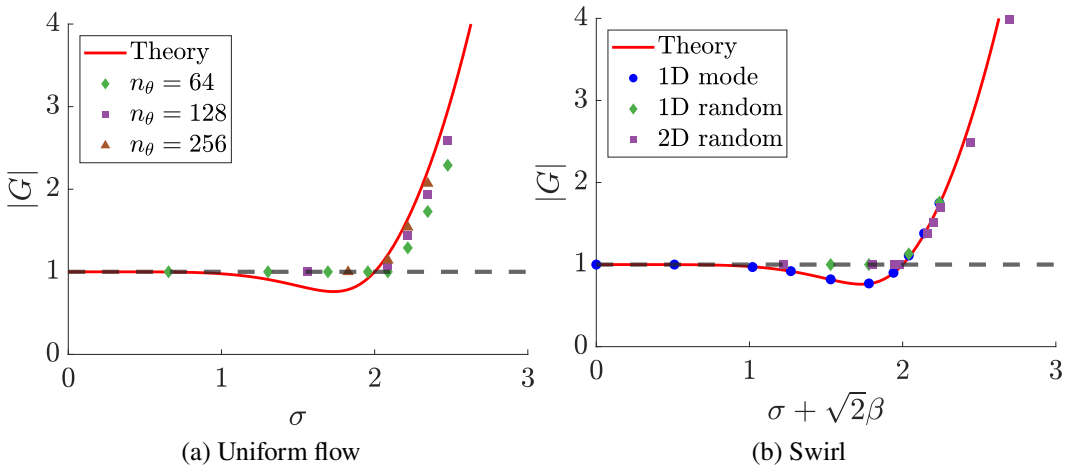
Figure A.4: Magnitude of the amplification factor of instabilities in cylindrical coordinates with four subiterations.

The numerical stability for these two test cases is shown in Fig. A.4 using 4 subiterations. Figure A.4a shows the growth rate of a case with uniform flow. For $n_\theta = 64$, there is a slight discrepancy between the theory and the measured values. Because u_θ is not constant, the instabilities 'feel' an effective u_θ corresponding to an average over a few wavelengths (which is lower than the maximum). As such, there is a grid dependence on the measured values. As the grid resolution is increased, this discrepancy is expected to decrease. This is reflected in the solutions for $n_\theta = 128$ and $n_\theta = 256$, which lie closer to the theoretically predicted values.

Figure A.4b shows the case of pure swirl. For both one-dimensional and two-dimensional simulations, the growth rates closely follow the theory when plotted against $\sigma + \sqrt{2}\beta$.

A.5 Implicit iterative method

To improve the numerical stability, the iterative method can be made semi-implicit (see Section A.2). This section provides a discussion of the formulation of the method and an evaluation of the numerical stability.

A.5.1 Implicit matrix formulation

Two implicit formulations of the momentum equation may be proposed.

Formally, as mentioned previously (Chapter 2), the governing equations are solved in the conservative form. The u_x-momentum equation in a three-dimensional inviscid Cartesian flow is given as:

$$\frac{\partial u_x}{\partial t} + \frac{\partial u_x u_x}{\partial x} + \frac{\partial u_x u_y}{\partial y} + \frac{\partial u_x u_z}{\partial z} + \frac{1}{\rho}\frac{\partial p}{\partial x} = 0 \tag{A.76}$$

Once again, we decompose the velocity into its mean and fluctuating components: $u_x = \bar{u}_x + u'_x$, with $u'_x \ll \bar{u}_x$. Recognizing that the mean flow is divergence free, the linearized equation in advection form is written:

$$\frac{\partial u'_x}{\partial t} + 2\bar{u}_x\frac{\partial u'_x}{\partial x} + \bar{u}_x\frac{\partial u'_y}{\partial y} + \bar{u}_y\frac{\partial u'_x}{\partial y} + \bar{u}_x\frac{\partial u'_z}{\partial z} + \bar{u}_z\frac{\partial u'_x}{\partial z} + \frac{1}{\rho}\frac{\partial p}{\partial x} = 0 \tag{A.77}$$

Along with the corresponding u'_y and u'_z equations, we obtain a set of three coupled equations for (u'_x, u'_y, u'_z) in three dimensions (x, y, z).

Alternatively, instead of developing an implicit formulation based on Eq. A.77, we take into account that the fluctuations are also divergence free, arriving at the equation:

$$\frac{\partial u'_x}{\partial t} + \bar{u}_x\frac{\partial u'_x}{\partial x} + \bar{u}_y\frac{\partial u'_x}{\partial y} + \bar{u}_z\frac{\partial u'_x}{\partial z} + \frac{1}{\rho}\frac{\partial p}{\partial x} = 0 \tag{A.78}$$

In this final formulation, the u'_x, u'_y, and u'_z equations are now decoupled. The approximate factorization requires that the equation be solved in each direction sequentially for each velocity component. The decoupling of the equations justifies the sequential nature of the semi-implicit scheme.

A.5.2 Implicit in single direction — Cartesian

We revisit the stability of the time integration in Cartesian coordinates done in Section A.3.3. This time, the semi-implicit algorithm described in Section A.2 is used in one direction, namely x. While similar to its explicit time integration counterpart, the semi-implicit time integration presents a couple of key subtleties.

Let's start with the case of one subiteration. After the predictor step, the velocity fluctuations are given by:

$$\widehat{u}^*_x = \frac{1 - j\Sigma' - \frac{1}{2}j\Sigma_x}{1 + \frac{1}{2}j\Sigma_x} \widehat{u}^n_x \tag{A.79}$$

$$\widehat{u}^*_y = \frac{1 - j\Sigma' - \frac{1}{2}j\Sigma_x}{1 + \frac{1}{2}j\Sigma_x} \widehat{u}^n_y \tag{A.80}$$

$$\widehat{u}^*_z = \frac{1 - j\Sigma' - \frac{1}{2}j\Sigma_x}{1 + \frac{1}{2}j\Sigma_x} \widehat{u}^n_z \tag{A.81}$$

where $\Sigma' = \Delta t \left(\bar{u}_y \kappa'_y + \bar{u}_z \kappa'_z\right)$ and $\Sigma_x = \Delta t \bar{u}_x \kappa'_x$. The corrector step remains the same, namely:

$$\widehat{u}^{n+1}_x = \widehat{u}^*_x - \Delta t j \kappa''_x \widehat{p} \tag{A.82}$$

$$\widehat{u}^{n+1}_y = \widehat{u}^*_y - \Delta t j \kappa''_y \widehat{p} \tag{A.83}$$

$$\widehat{u}^{n+1}_z = \widehat{u}^*_z - \Delta t j \kappa''_z \widehat{p} \tag{A.84}$$

Once again, an expression for $\widehat{p}$ can be obtained by substituting $\widehat{u}^{n+1}_x$, $\widehat{u}^{n+1}_y$, and $\widehat{u}^{n+1}_z$ into continuity. After manipulation, the final equations can be expressed in matrix form:

$$\begin{bmatrix} \widehat{u}_x \\ \widehat{u}_y \\ \widehat{u}_z \end{bmatrix}^{n+1} = \frac{1 - j\Sigma' - \frac{1}{2}j\Sigma_x}{1 + \frac{1}{2}j\Sigma_x} \mathbf{A} \begin{bmatrix} \widehat{u}_x \\ \widehat{u}_y \\ \widehat{u}_z \end{bmatrix}^n \tag{A.85}$$

The $\mathbf{A}$ matrix remains the same as before (its largest eigenvalue is $\lambda_2 = 1$). As a result, the stability of the semi-implicit system is controlled by the complex amplification factor:

$$G_1 = \frac{1 - j\Sigma' - \frac{1}{2}j\Sigma_x}{1 + \frac{1}{2}j\Sigma_x} \tag{A.86}$$

Unlike for the explicit time integration, the amplification factor is now a function of two parameters, namely Σ_x and Σ'. These two parameters take values between $0 \leq |\Sigma_x| \leq \sigma_x$ and $0 \leq |\Sigma'| \leq \sigma_y + \sigma_z \equiv \sigma'$. The magnitude of G_1 happens to be the largest when Σ' is the largest (namely $\Sigma' = \sigma'$) and $\Sigma_x = \sqrt{\Sigma'^2 + 4} - \Sigma'$. Hence, for $\Sigma_x > 2 > \sqrt{\Sigma'^2 + 4} - \Sigma'$, the amplification factor is independent of the CFL in the implicit direction (namely σ_x) and takes the form:

$$|G_1|^2 = 1 + \frac{2\sigma'}{\sqrt{\sigma'^2 + 4} - \sigma'} \tag{A.87}$$

The recursive relationship for any number of subiterations is:

$$G_{k+1} = \frac{1 - \frac{1}{2}j\Sigma'(1 + G_k) - \frac{1}{2}j\Sigma_x}{1 + \frac{1}{2}j\Sigma_x} \tag{A.88}$$

For two subiterations, the maximum amplification factor is given by:

$$|G_2|^2 = 1 + \frac{\sigma'^4}{4} \tag{A.89}$$

which occurs when $\Sigma_x = 0$ regardless of σ_x. For three subiterations, the maximum amplification factor occurs around $\Sigma_x \approx 3.3\text{--}3.45$ and is well approximated by:

$$|G_3|^2 \approx 1 + 0.028\sigma'^3 \tag{A.90}$$

for $\sigma_x > 3.45$. For four subiterations, the maximum amplification factor is approximated by:

$$|G_4|^2 \approx 1 + \frac{44}{625}\sigma'^4 + \frac{32}{625}\sigma'^5 - \frac{16}{625}\sigma'^6 + \frac{4}{625}\sigma'^8 \tag{A.91}$$

which occurs when $\Sigma_x \approx 1$.

Four key observations can be made. First, for large CFL numbers in the implicit direction (i.e., large σ_x), the amplification factor is only a function of the total CFL numbers in the explicit directions (i.e., $\sigma' = \sigma_y + \sigma_z$). Second, the amplification factor is always greater than 1. Third, the limit of the amplification factor at small explicit CFL (i.e., $\sigma' \to 0$) is exactly 1. Finally, these amplification factors should be understood as upper limits. The Σ_x values that correspond to these maxima (e.g., $\Sigma_x \approx 1$ for four subiterations) may not be realizable on a given computational grid.

A.5.3 Numerical verification

The numerical stability of the implicit iterative method is tested numerically in three dimensions using a two-dimensional mean flow, with constant $\bar{u}_x$ and $\bar{u}_y = 1$,

and initial random perturbations of 1×10^{-9} amplitude in u_z. Two different mean flows in x are used, namely $\overline{u}_x = 1$ and 10. Once again, the domain is of size $L_x = L_y = L_z = 1$ with $n_x = n_y = n_z = 64$ with triply periodic boundary conditions. The implicit treatment is in the x-direction.

(a) 1 subiteration

(b) 2 subiterations

(c) 3 subiterations
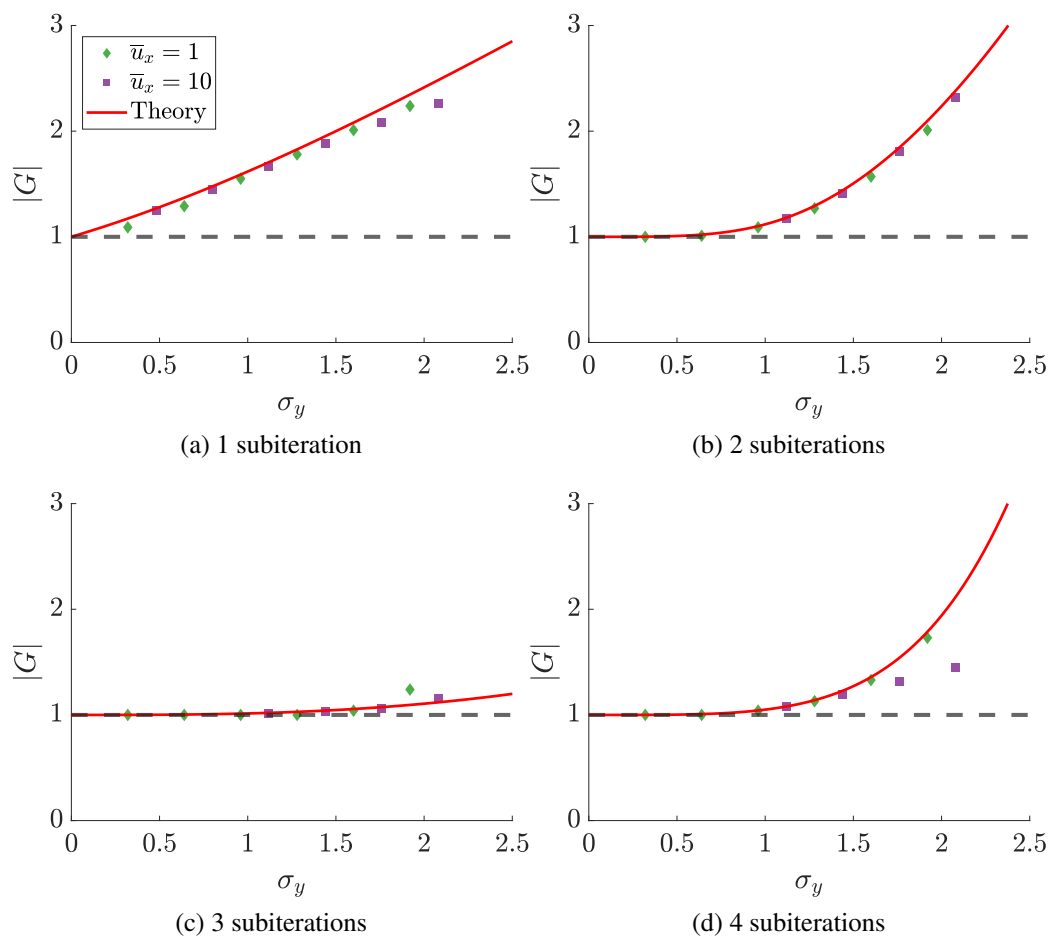
(d) 4 subiterations

Figure A.5: Magnitude of the amplification factor of the semi-implicit time integration with varying numbers of subiterations as a function of the CFL number in the explicit direction.

The results are shown in Fig. A.5. For most cases, the amplification factors for $\overline{u}_x = 1$ and $\overline{u}_x = 10$ are indistinguishable and agree well with the theoretical predictions. The results confirm that the controlling CFL number is in the direction which is not treated implicitly. For one and four subiterations, when $\overline{u}_x$ is increased by a factor of ten, the magnitude of the amplification factor is reduced below the theoretical predictions. Recall that these predictions are upper limits, and the most unstable analytical prediction may not be realized on the computational grid.

A.5.4 Implication for cylindrical flows

From a theoretical point of view, the semi-implicit treatment brings little to no benefits to the stability of the Cartesian cases. Specifically, the configurations which were stable in the explicit formulation (i.e., total CFL $\sigma_x + \sigma_y + \sigma_z < 2$) are unstable in the semi-implicit formulation. It does, however, provide "practical" stability to cylindrical cases.

As discussed previously, swirling flows do not lead to large azimuthal CFL numbers because the azimuthal velocity scales with r. The most stringent condition for simulations in cylindrical coordinates is encountered with a uniform flow (in Cartesian coordinates). In such flows, the azimuthal CFL number is about n_θ/π larger than the radial CFL around the centerline.

Strictly speaking, an amplification factor of magnitude 1.01 corresponds to an unstable solution, but the solution is practically stable (it would take about 230 timesteps for the oscillations to grow by one order of magnitude). With three (or four) subiterations, with only one direction treated implicitly, here θ, this amplification factor is reached with an explicit CFL number of $\sigma' = \sigma_x + \sigma_r \approx 0.71$ (0.68). With only 64 points in the azimuthal direction, this leads to $\sigma_\theta \approx 14$ (12). Clearly a fully explicit treatment of such case would be unstable.

In simulations of turbulent flows, it is common to use grids with close to identical spacing in x and r at the centerline, that is, $\Delta x = \Delta r$. However, not counting cross flows which are short-lived, the mean flow in x is usually an order of magnitude larger than in r. Hence, at the centerline, $\sigma' \approx \sigma_x$. Therefore, practical stability may be ensured if $\sigma_x < 0.7$ at the centerline with at least three subiterations.

Away from centerline, the azimuthal CFL number decreases rapidly ($\sigma_\theta \propto 1/r$) and the implicit stability limits approach the explicit stability theory. Thus, the CFL restriction becomes that discussed in Section A.4.2.

A.5.5 Inconsistency with pressure correction step

Recall that for the explicit iterative method, the predictor is written as:

$$\frac{u^* - u^n}{\Delta t} + f\left[\frac{1}{2}\left(u_k^{n+1} + u^n\right)\right] = -\delta_{\mathbf{x}} p_k^{n+1} \tag{A.92}$$

where f represents the convective (and diffusive) terms. The velocity and pressure updates take the form:

$$u_{k+1}^{n+1} = u^* - \Delta t \delta_{\mathbf{x}}\left(\delta p_{k+1}^{n+1}\right) \tag{A.93}$$

$$p_{k+1}^{n+1} = p_k^{n+1} + \delta p_{k+1}^{n+1} \tag{A.94}$$

Eqs. A.92 and A.93 can be combined to yield:

$$u_{k+1}^{n+1} = u^n - \Delta t f \left[\frac{1}{2} \left(u_k^{n+1} + u^n \right) \right] - \Delta t \delta_{\mathbf{x}} \left(p_k^{n+1} + \delta p_{k+1}^{n+1} \right) \tag{A.95}$$

The pressure correction in Eq. A.94 appears exactly in Eq. A.95, ensuring that the predicted velocity for the next subiteration is calculated with the correct and most updated pressure.

For the implicit scheme, the predictor is now written as:

$$\frac{u^* - u^n}{\Delta t} + f \left[\frac{1}{2} \left(u_k^{n+1} + u^n \right) \right] + \frac{1}{2} \frac{\partial f}{\partial u} \left(u^* - u_k^{n+1} \right) = -\delta_x p_k^{n+1} \tag{A.96}$$

Combining this equation with the velocity correction of Eq. A.93 yields:

$$\begin{aligned}
u_{k+1}^{n+1} = \left(1 - \frac{\Delta t}{2} \frac{\partial f}{\partial u} \right)^{-1} & \left\{ u^n - \Delta t f \left[\frac{1}{2} \left(u_k^{n+1} + u^n \right) \right] \right. \\
& \left. - \frac{\Delta t}{2} \frac{\partial f}{\partial u} u_k^{n+1} - \Delta t \delta_{\mathbf{x}} \left[p_k^{n+1} + \left(1 - \frac{\Delta t}{2} \frac{\partial f}{\partial u} \right) \delta p_{k+1}^{n+1} \right] \right\}
\end{aligned} \tag{A.97}$$

since $\frac{\partial f}{\partial u}$ is a linear operator and commutes with the gradient δ_x. However, the pressure term which appears in Eq. A.97 is now inconsistent with the pressure update step of Eq. A.94. To obtain the most accurate prediction for the next subiteration, the pressure update should instead be calculated as:

$$p_{k+1}^{n+1} = p_k^{n+1} + \left(1 - \frac{\Delta t}{2} \frac{\partial f}{\partial u} \right) \delta p_{k+1}^{n+1} \tag{A.98}$$

This formulation is expected to lead to quicker convergence of the pressure with subiterations. However, it presents several challenges. First, the discrete operator $(1 - \Delta t \partial f / \partial u)$ acts on the face-centered values, whereas δp is a cell-centered value. Second, the operator for the different velocity components may not be the same. For these reasons, it was not implemented.

A.6 Conclusions

In summary, the numerical stability of the midpoint iterative time integration scheme was studied in detail. The key conclusions are as follows:

- For three dimensions in Cartesian coordinates treated explicitly, the stability limit is determined by the sum of the three CFL numbers, $\sigma = \sigma_x + \sigma_y + \sigma_z < 2$. A minimum of three subiterations are required.

- For three dimensions in Cylindrical coordinates treated explicitly, the stability is also determined by the sum of the three CFL conditions with an additional term. The total sum must also be less than 2.

- The implicit treatment is always unstable, but may provide practical benefits for cylindrical flows. Keeping the sum of the radial and axial CFL numbers at around 0.7 is sufficient to ensure stability for practical purposes regardless of the azimuthal CFL, which can be on the order of 10–20.

BIBLIOGRAPHY

[1]   U. S. EIA. *Annual Energy Outlook 2023*. 2023. URL: https://www.eia.gov/outlooks/aeo/pdf/AEO2023_Narrative.pdf.

[2]   T. W. House. *FACT SHEET: President Biden Sets 2030 Greenhouse Gas Pollution Reduction Target Aimed at Creating Good-Paying Union Jobs and Securing U.S. Leadership on Clean Energy Technologies*. 2021. URL: https://www.whitehouse.gov/briefing-room/statements-releases/2021/04/22/fact-sheet-president-biden-sets-2030-greenhouse-gas-pollution-reduction-target-aimed-at-creating-good-paying-union-jobs-and-securing-u-s-leadership-on-clean-energy-technologies/.

[3]   U. S. EIA. *International Energy Outlook 2023*. 2023. URL: https://www.eia.gov/outlooks/ieo/pdf/IEO2023_Narrative.pdf.

[4]   J. Lelieveld et al. "Air pollution deaths attributable to fossil fuels: observational and modelling study". In: *BMJ* 383 (2023).

[5]   F. Perera and K. Nadeau. "Climate change, fossil-fuel pollution, and children's health". In: *New England Journal of Medicine* 386.24 (2022), pp. 2303–2314.

[6]   J. G. Aguilar, E. Æsøy, and J. R. Dawson. "The influence of hydrogen on the stability of a perfectly premixed combustor". In: *Combustion and Flame* 245 (2022), p. 112323.

[7]   J. B. Cristello et al. "Feasibility analysis of blending hydrogen into natural gas networks". In: *International Journal of Hydrogen Energy* 48.46 (2023), pp. 17605–17629.

[8]   S. Verhelst. "Recent progress in the use of hydrogen as a fuel for internal combustion engines". In: *International Journal of Hydrogen Energy* 39.2 (2014), pp. 1071–1085.

[9]   S. Verhelst and T. Wallner. "Hydrogen-fueled internal combustion engines". In: *Progress in Energy and Combustion Science* 35.6 (2009), pp. 490–527.

[10] J. Zhou, C. S. Cheung, and C. W. Leung. "Combustion, performance, regulated and unregulated emissions of a diesel engine with hydrogen addition". In: *Applied energy* 126 (2014), pp. 1–12.

[11] R. Cheng et al. "Laboratory investigations of a low-swirl injector with H2 and CH4 at gas turbine conditions". In: *Proceedings of the Combustion Institute* 32.2 (2009), pp. 3001–3009.

[12] D. Littlejohn and R. Cheng. "Fuel effects on a low-swirl injector for lean premixed gas turbines". In: *Proceedings of the Combustion Institute* 31.2 (2007), pp. 3155–3162.

[13] Z. Liu et al. "Effects of hydrogen addition on combustion characteristics of a methane fueled MILD model combustor". In: *International Journal of Hydrogen Energy* 47.36 (2022), pp. 16309–16320.

[14] D. L. Mauzerall et al. "NOx emissions from large point sources: variability in ozone production, resulting health damages and economic costs". In: *Atmospheric Environment* 39.16 (2005), pp. 2851–2866.

[15] A. Frassoldati, T. Faravelli, and E. Ranzi. "A wide range modeling study of NOx formation and nitrogen chemistry in hydrogen combustion". In: *International Journal of Hydrogen Energy* 31.15 (2006), pp. 2310–2328.

[16] S. R. Turns. *Introduction to Combustion*. Vol. 287. McGraw-Hill Companies New York, NY, USA, 1996.

[17] H. Pitsch. "FlameMaster: A C++ computer program for 0D combustion and 1D laminar flame calculations". In: *Technical Report, RWTH Aachen University* (1998).

[18] S. Yang et al. "Extreme role of preferential diffusion in turbulent flame propagation". In: *Combustion and Flame* 188 (2018), pp. 498–504.

[19] B. Savard and G. Blanquart. "An a priori model for the effective species Lewis numbers in premixed turbulent flames". In: *Combustion and Flame* 161.6 (2014), pp. 1547–1557.

[20] A. Aspden, M. Day, and J. Bell. "Towards the distributed burning regime in turbulent premixed flames". In: *Journal of Fluid Mechanics* 871 (2019), pp. 1–21.

[21] B. Bregeon, A. S. Gordon, and F. A. Williams. "Near-limit downward propagation of hydrogen and methane flames in oxygen–nitrogen mixtures". In: *Combustion and Flame* 33 (1978), pp. 33–45.

[22] T. Mitani and F. Williams. "Studies of cellular flames in hydrogen–oxygen–nitrogen mixtures". In: *Combustion and Flame* 39.2 (1980), pp. 169–190.

[23] M. Matalon, C. Cui, and J. Bechtold. "Hydrodynamic theory of premixed flames: effects of stoichiometry, variable transport coefficients and arbitrary reaction orders". In: *Journal of Fluid Mechanics* 487 (2003), pp. 179–210.

[24] C. Altantzis et al. "Hydrodynamic and thermodiffusive instability effects on the evolution of laminar planar lean premixed hydrogen flames". In: *Journal of Fluid Mechanics* 700 (2012), pp. 329–361.

[25] L. Berger, A. Attili, and H. Pitsch. "Intrinsic instabilities in premixed hydrogen flames: Parametric variation of pressure, equivalence ratio, and temperature. Part 1-dispersion relations in the linear regime". In: *Combustion and Flame* 240 (2022), p. 111935.

[26] J. F. Grcar, J. B. Bell, and M. S. Day. "The Soret effect in naturally propagating, premixed, lean, hydrogen–air flames". In: *Proceedings of the Combustion Institute* 32.1 (2009), pp. 1173–1180.

[27] H. Kido et al. "Influence of local flame displacement velocity on turbulent burning velocity". In: *Proceedings of the Combustion Institute* 29.2 (2002), pp. 1855–1861.

[28] L. Berger, A. Attili, and H. Pitsch. "Synergistic interactions of thermodiffusive instabilities and turbulence in lean hydrogen flames". In: *Combustion and Flame* 244 (2022), p. 112254.

[29] C. Dhandapani and G. Blanquart. "From isotropic turbulence in triply periodic cubic domains to sheared turbulence with inflow/outflow". In: *Physical Review Fluids* 5.12 (2020), p. 124605.

[30] B. Savard and G. Blanquart. "Broken reaction zone and differential diffusion effects in high Karlovitz n-C7H16 premixed turbulent flames". In: *Combustion and Flame* 162.5 (2015), pp. 2020–2033.

[31] S. Lapointe, B. Savard, and G. Blanquart. "Differential diffusion effects, distributed burning, and local extinctions in high Karlovitz premixed flames". In: *Combustion and Flame* 162.9 (2015), pp. 3341–3355.

[32] B. Bobbitt, S. Lapointe, and G. Blanquart. "Vorticity transformation in high Karlovitz number premixed flames". In: *Physics of Fluids* 28.1 (2016), p. 015101.

[33] J. Schlup and G. Blanquart. "Reproducing curvature effects due to differential diffusion in tabulated chemistry for premixed flames". In: *Proceedings of the Combustion Institute* 37.2 (2019), pp. 2511–2518.

[34] H. Lee et al. "Influence of molecular transport on burning rate and conditioned species concentrations in highly turbulent premixed flames". In: *Journal of Fluid Mechanics* 928 (2021), A5.

[35] H. Lee et al. "A DNS study of extreme and leading points in lean hydrogen-air turbulent flames–Part I: Local thermochemical structure and reaction rates". In: *Combustion and Flame* 235 (2022), p. 111716.

[36] W. Song et al. "Statistics of local and global flame speed and structure for highly turbulent H2/air premixed flames". In: *Combustion and Flame* 232 (2021), p. 111523.

[37] Yuvraj et al. "Local flame displacement speeds of hydrogen-air premixed flames in moderate to intense turbulence". In: *Combustion and Flame* 236 (2022), p. 111812.

[38] A. Aspden, M. Day, and J. Bell. "Turbulence–flame interactions in lean premixed hydrogen: transition to the distributed burning regime". In: *Journal of Fluid Mechanics* 680 (2011), pp. 287–320.

[39] T. Howarth, E. Hunt, and A. Aspden. "Thermodiffusively-unstable lean premixed hydrogen flames: Phenomenology, empirical modelling, and thermal leading points". In: *Combustion and Flame* 253 (2023), p. 112811.

[40] G. Damköhler. "Der einfluss der turbulenz auf die flammengeschwindigkeit in gasgemischen". In: *Zeitschrift für Elektrochemie und Angewandte Physikalische Chemie* 46.11 (1940), pp. 601–626.

[41] K. N. C. Bray. "Studies of the turbulent burning velocity". In: *Proceedings of the Royal Society of London. Series A: Mathematical and Physical Sciences* 431.1882 (1990), pp. 315–335.

[42] S. M. Candel and T. J. Poinsot. "Flame stretch and the balance equation for the flame area". In: *Combustion Science and Technology* 70.1-3 (1990), pp. 1–15.

[43] S. Lapointe and G. Blanquart. "Fuel and chemistry effects in high Karlovitz premixed turbulent flames". In: *Combustion and Flame* 167 (2016), pp. 294–307.

[44] F. Yang et al. "A mechanistic study of Soret diffusion in hydrogen–air flames". In: *Combustion and Flame* 157.1 (2010), pp. 192–200.

[45] W. Song, F. E. Hernández-Pérez, and H. G. Im. "Diffusive effects of hydrogen on pressurized lean turbulent hydrogen-air premixed flames". In: *Combustion and Flame* 246 (2022), p. 112423.

[46] O. Gicquel, N. Darabiha, and D. Thévenin. "Laminar premixed hydrogen/air counterflow flame simulations using flame prolongation of ILDM with differential diffusion". In: *Proceedings of the Combustion Institute* 28.2 (2000), pp. 1901–1908.

[47] J. Van Oijen, F. Lammers, and L. De Goey. "Modeling of complex premixed burner systems by using flamelet-generated manifolds". In: *Combustion and Flame* 127.3 (2001), pp. 2124–2134.

[48] J. Van Oijen, R. Bastiaans, and L. De Goey. "Low-dimensional manifolds in Direct Numerical Simulations of premixed turbulent flames". In: *Proceedings of the Combustion Institute* 31.1 (2007), pp. 1377–1384.

[49] A. Najafi-Yazdi, B. Cuenot, and L. Mongeau. "Systematic definition of progress variables and intrinsically low-dimensional, flamelet generated manifolds for chemistry tabulation". In: *Combustion and Flame* 159.3 (2012), pp. 1197–1204.

[50] J. Van Oijen et al. "Direct numerical simulations of premixed turbulent flames with reduced chemistry: Validation and flamelet analysis". In: *Flow, Turbulence and Combustion* 75.1 (2005), pp. 67–84.

[51] J. A. de Swart et al. "Inclusion of preferential diffusion in simulations of premixed combustion of hydrogen/methane mixtures with flamelet generated manifolds". In: *Flow, turbulence and combustion* 85.3 (2010), pp. 473–511.

[52] A. Donini et al. "Differential diffusion effects inclusion with flamelet generated manifold for the modeling of stratified premixed cooled flames". In: *Proceedings of the Combustion Institute* 35.1 (2015), pp. 831–837.

[53] R. Bilger, S. Stårner, and R. Kee. "On reduced mechanisms for methane-air combustion in nonpremixed flames". In: *Combustion and Flame* 80.2 (1990), pp. 135–149.

[54] N. Mukundakumar et al. "A new preferential diffusion model applied to FGM simulations of hydrogen flames". In: *Combustion Theory and Modelling* 25.7 (2021), pp. 1245–1267.

[55] H. Böttler et al. "Flamelet modeling of forced ignition and flame propagation in hydrogen-air mixtures". In: *Combustion and Flame* 243 (2022), p. 112125.

[56] H. Böttler et al. "Flamelet modeling of thermo-diffusively unstable hydrogen-air flames". In: *Proceedings of the Combustion Institute* 39.2 (2023), pp. 1567–1576.

[57] A. Scholtissek et al. "A self-contained composition space solution method for strained and curved premixed flamelets". In: *Combustion and Flame* 207 (2019), pp. 342–355.

[58] J. D. Regele et al. "A two-equation model for non-unity Lewis number differential diffusion in lean premixed laminar flames". In: *Combustion and Flame* 160.2 (2013), pp. 240–250.

[59] O. Colin et al. "A thickened flame model for Large Eddy Simulations of turbulent premixed combustion". In: *Physics of fluids* 12.7 (2000), pp. 1843–1863.

[60] J.-P. Legier, T. Poinsot, and D. Veynante. "Dynamically thickened flame LES model for premixed and non-premixed turbulent combustion". In: *Proceedings of the summer program*. Vol. 12. 2000.

[61] M. Anand and S. Pope. "Calculations of premixed turbulent flames by PDF methods". In: *Combustion and Flame* 67.2 (1987), pp. 127–142.

[62] R. Lindstedt and E. Vaos. "Transported PDF modeling of high-Reynolds-number premixed turbulent flames". In: *Combustion and Flame* 145.3 (2006), pp. 495–511.

[63] L. Berger et al. "Development of Large-Eddy Simulation Combustion Models for Thermodiffusive Instabilities in Turbulent Hydrogen Flames". In: *Proceeding of the Summer Program, Center for Turbulence Research, Stanford University* (2022), p. 247.

[64] O. Desjardins et al. "High order conservative finite difference scheme for variable density low Mach number turbulent flows". In: *Journal of Computational Physics* 227.15 (2008), pp. 7125–7159.

[65] A. Majda and J. Sethian. "The derivation and numerical solution of the equations for zero Mach number combustion". In: *Combustion science and technology* 42.3-4 (1985), pp. 185–205.

[66] S. Mathur, P. Tondon, and S. Saxena. "Thermal conductivity of binary, ternary and quaternary mixtures of rare gases". In: *Molecular Physics* 12.6 (1967), pp. 569–579.

[67] A. Eucken. "Über das Wärmeleitvermögen, die spezifische Wärme und die innere Reibung der Gase". In: *Physikalische Zeitschrift* 14.8 (1913), pp. 324–332.

[68] J. O. Hirschfelder, C. F. Curtiss, R. B. Bird, et al. *Molecular Theory of Gases and Liquids*. Wiley New York, 1954.

[69] C. R. Wilke. "A viscosity equation for gas mixtures". In: *The Journal of Chemical Physics* 18.4 (1950), pp. 517–519.

[70] T. Coffee and J. Heimerl. "Transport algorithms for premixed, laminar steady-state flames". In: *Combustion and Flame* 43 (1981), pp. 273–289.

[71] R. J. Kee, M. E. Coltrin, and P. Glarborg. *Chemically Reacting Flow: Theory and Practice*. John Wiley & Sons, 2005.

[72] J. Schlup and G. Blanquart. "A reduced thermal diffusion model for H and H2". In: *Combustion and Flame* 191 (2018), pp. 1–8.

[73] J. Schlup and G. Blanquart. "Validation of a mixture-averaged thermal diffusion model for premixed lean hydrogen flames". In: *Combustion Theory and Modelling* 22.2 (2018), pp. 264–290.

[74] Y. Xuan, G. Blanquart, and M. E. Mueller. "Modeling curvature effects in diffusion flames using a laminar flamelet model". In: *Combustion and Flame* 161.5 (2014), pp. 1294–1309.

[75] B. Savard and G. Blanquart. "Effects of dissipation rate and diffusion rate of the progress variable on local fuel burning rate in premixed turbulent flames". In: *Combustion and Flame* 180 (2017), pp. 77–87.

[76] C. Meneveau, T. S. Lund, and W. H. Cabot. "A Lagrangian dynamic subgrid-scale model of turbulence". In: *Journal of Fluid Mechanics* 319 (1996), pp. 353–385.

[77] C. Fureby. "Large eddy simulation modelling of combustion for propulsion applications". In: *Philosophical Transactions of the Royal Society A: Mathematical, Physical and Engineering Sciences* 367.1899 (2009), pp. 2957–2969.

[78] A. Y. Klimenko and R. W. Bilger. "Conditional moment closure for turbulent combustion". In: *Progress in Energy and Combustion Science* 25.6 (1999), pp. 595–687.

[79] I. Porumbel and S. Menon. "Large eddy simulation of bluff body stabilized premixed flame". In: *44th AIAA Aerospace Sciences Meeting and Exhibit*. 2006, p. 152.

[80] L. Y. Gicquel, G. Staffelbach, and T. Poinsot. "Large eddy simulations of gaseous flames in gas turbine combustion chambers". In: *Progress in Energy and Combustion Science* 38.6 (2012), pp. 782–817.

[81] H. Pitsch. "Large-eddy simulation of turbulent combustion". In: *Annual Review of Fluid Mechanics* 38 (2006), pp. 453–482.

[82] J. Van Oijen et al. "State-of-the-art in premixed combustion modeling using flamelet generated manifolds". In: *Progress in Energy and Combustion Science* 57 (2016), pp. 30–74.

[83] J. Réveillon and L. Vervisch. "Response of the dynamic LES model to heat release induced effects". In: *Physics of Fluids* 8.8 (1996), pp. 2248–2250.

[84] D. K. Lilly. "On the application of the eddy viscosity concept in the inertial sub-range of turbulence". In: *NCAR manuscript* 123 (1966).

[85] M. Germano et al. "A dynamic subgrid-scale eddy viscosity model". In: *Physics of Fluids A: Fluid Dynamics* 3.7 (1991), pp. 1760–1765.

[86] D. Lilly. "A proposed modification of the ¨Germano sugrid-scale closure method". In: *Phys Fluids A* 4 (1992), pp. 633–635.

[87] C. D. Pierce and P. Moin. "A dynamic model for subgrid-scale variance and dissipation rate of a conserved scalar". In: *Physics of Fluids* 10.12 (1998), pp. 3041–3044.

[88] B. Savard et al. "A computationally-efficient, semi-implicit, iterative method for the time-integration of reacting flows with stiff chemistry". In: *Journal of Computational Physics* 295 (2015), pp. 740–769.

[89] C. D. Pierce. "Progress-variable approach for large-eddy simulation of turbulent combustion". PhD thesis. Stanford University, 2001.

[90] R. Mittal and G. Iaccarino. "Immersed boundary methods". In: *Annual Review of Fluid Mechanics* 37 (2005), pp. 239–261.

[91] R. Verzicco. "Immersed boundary methods: Historical perspective and future outlook". In: *Annual Review of Fluid Mechanics* 55 (2023), pp. 129–155.

[92] S. Kang et al. "Prediction of wall-pressure fluctuation in turbulent flows with an immersed boundary method". In: *Journal of Computational Physics* 228.18 (2009), pp. 6753–6772.

[93] G.-S. Jiang and C.-W. Shu. "Efficient implementation of weighted ENO schemes". In: *Journal of Computational Physics* 126.1 (1996), pp. 202–228.

[94] P.-K. Yeung and S. B. Pope. "Lagrangian statistics from direct numerical simulations of isotropic turbulence". In: *Journal of Fluid Mechanics* 207 (1989), pp. 531–586.

[95] Z. Hong, D. F. Davidson, and R. K. Hanson. "An improved H2/O2 mechanism based on recent shock tube/laser absorption measurements". In: *Combustion and Flame* 158.4 (2011), pp. 633–644.

[96] Z. Hong et al. "On the rate constants of OH+ HO2 and HO2+ HO2: A comprehensive study of H2O2 thermal decomposition using multi-species laser absorption". In: *Proceedings of the Combustion Institute* 34.1 (2013), pp. 565–571.

[97] K.-Y. Lam, D. F. Davidson, and R. K. Hanson. "A shock tube study of H2+ OH→ H2O+ H using OH laser absorption". In: *International Journal of Chemical Kinetics* 45.6 (2013), pp. 363–373.

[98] N. Peters. *Turbulent Combustion*. Cambridge University Press, 2000.

[99] S. Trivedi and R. Cant. "Turbulence intensity and length scale effects on premixed turbulent flame propagation". In: *Flow Turbulence and Combustion* 109.1 (2022), pp. 101–123.

[100] R. Sankaran et al. "Response of flame thickness and propagation speed under intense turbulence in spatially developing lean premixed methane–air jet flames". In: *Combustion and Flame* 162.9 (2015), pp. 3294–3306.

[101] C. Dhandapani. "Using the force: Applications and implications of turbulence forcing terms in direct numerical simulations". PhD thesis. California Institute of Technology, 2019.

[102] T. S. Lundgren. "Linearly forced isotropic turbulence". In: *Center for Turbulence Research Annual Research Briefs 2003* (2003).

[103] C. Rosales and C. Meneveau. "Linear forcing in numerical simulations of isotropic turbulence: Physical space implementations and convergence properties". In: *Physics of Fluids* 17.9 (2005), p. 095106.

[104] P. L. Carroll and G. Blanquart. "A proposed modification to Lundgren's physical space velocity forcing method for isotropic turbulence". In: *Physics of Fluids* 25.10 (2013), p. 105114.

[105] A. L. Sánchez and F. A. Williams. "Recent advances in understanding of flammability characteristics of hydrogen". In: *Progress in Energy and Combustion Science* 41 (2014), pp. 1–55.

[106] Z. Liu et al. "Cellular instability in Le< 1 turbulent expanding flames". In: *Proceedings of the Combustion Institute* 37.2 (2019), pp. 2611–2618.

[107] S. Chaudhuri, V. Akkerman, and C. K. Law. "Spectral formulation of turbulent flame speed with consideration of hydrodynamic instability". In: *Physical Review E* 84.2 (2011), p. 026322.

[108] M. Day et al. "Turbulence effects on cellular burning structures in lean premixed hydrogen flames". In: *Combustion and Flame* 156.5 (2009), pp. 1035–1045.

[109] W. E. Lorensen and H. E. Cline. "Marching Cubes: A High Resolution 3D Surface Construction Algorithm". In: *SIGGRAPH Comput. Graph.* 21.4 (1987), pp. 163–169. ISSN: 0097-8930. DOI: 10.1145/37402.37422. URL: https://doi.org/10.1145/37402.37422.

[110] S. Lapointe. "Simulation of premixed hydrocarbon flames at high turbulence intensities". PhD thesis. California Institute of Technology, 2016.

[111] P. Yeung, S. Girimaji, and S. Pope. "Straining and scalar dissipation on material surfaces in turbulence: implications for flamelets". In: *Combustion and Flame* 79.3-4 (1990), pp. 340–365.

[112] A. Aspden, M. Day, and J. Bell. "Characterization of low Lewis number flames". In: *Proceedings of the Combustion Institute* 33.1 (2011), pp. 1463–1471.

[113] B. Savard, B. Bobbitt, and G. Blanquart. "Structure of a high Karlovitz n-C7H16 premixed turbulent flame". In: *Proceedings of the Combustion Institute* 35.2 (2015), pp. 1377–1384.

[114] N. Burali et al. "Assessment of the constant non-unity Lewis number assumption in chemically-reacting flows". In: *Combustion Theory and Modelling* 20.4 (2016), pp. 632–657.

[115] N. Peters. *Fifteen Lectures on Laminar and Turbulent Combustion.* https://www.itv.rwth-aachen.de/fileadmin/Downloads/Summerschools/SummerSchool.pdf. Accessed: 2023-10-10. 1992.

[116] M. X. Yao and G. Blanquart. *Isolating effects of large and small scale turbulence on thermodiffusively unstable premixed hydrogen flames.* 2023. arXiv: 2311.18131 [physics.flu-dyn].

[117] G. P. Smith. *GRI-Mech 3.0.* 1999. URL: http://www.me.berkley.edu/gri_mech/.

[118] S. B. Pope. "PDF methods for turbulent reactive flows". In: *Progress in Energy and Combustion Science* 11.2 (1985), pp. 119–192.

[119] A. Giusti and E. Mastorakos. "Turbulent combustion modelling and experiments: Recent trends and developments". In: *Flow, Turbulence and Combustion* 103.4 (2019), pp. 847–869.

[120] B. Fiorina et al. "Premixed turbulent combustion modeling using tabulated detailed chemistry and PDF". In: *Proceedings of the Combustion Institute* 30.1 (2005), pp. 867–874.

[121] F. Hernández-Pérez et al. "LES of a laboratory-scale turbulent premixed Bunsen flame using FSD, PCM-FPI and thickened flame models". In: *Proceedings of the Combustion Institute* 33.1 (2011), pp. 1365–1371.

[122] S. Mukhopadhyay, J. Van Oijen, and L. De Goey. "A comparative study of presumed PDFs for premixed turbulent combustion modeling based on progress variable and its variance". In: *Fuel* 159 (2015), pp. 728–740.

[123] S. Lapointe and G. Blanquart. "A priori filtered chemical source term modeling for LES of high Karlovitz number premixed flames". In: *Combustion and Flame* 176 (2017), pp. 500–510.

[124] J. Smolke et al. "Experimental and numerical studies of fuel and hydrodynamic effects on piloted turbulent premixed jet flames". In: *Proceedings of the Combustion Institute* 36.2 (2017), pp. 1877–1884.

[125] S. Pope. *Turbulent Flows*. Cambridge University Press, 2000. ISBN: 9781139643351.

[126] J. Schlup. "Numerical Investigations of Transport and Chemistry Modeling for Lean Premixed Hydrogen Combustion". PhD thesis. California Institute of Technology, 2018.

[127] B. Fiorina et al. "A filtered tabulated chemistry model for LES of premixed combustion". In: *Combustion and Flame* 157.3 (2010), pp. 465–475.

[128] J. Kim and P. Moin. "Application of a fractional-step method to incompressible Navier–Stokes equations". In: *Journal of Computational Physics* 59.2 (1985), pp. 308–323.

[129] G. S. Constantinescu and S. Lele. "A highly accurate technique for the treatment of flow equations at the polar axis in cylindrical coordinates using series expansions". In: *Journal of Computational Physics* 183.1 (2002), pp. 165–186.